Scanning Tunnelling Microscopy and Electron Spectroscopy Studies of Gold Nanoparticles Dispersed Over Rutile TiO_2 (110)

Andrew Gerrard Mellor

Supervised by Prof. Geoff Thornton

Thesis submitted for the Degree of Doctor of Engineering to the University College London

Department of Chemistry

University College London

2017

I, Andrew Gerrard Mellor, confirm that the work presented in this thesis is my own. Where information has been derived from other sources, I confirm that this has been indicated in the thesis.

Abstract

This thesis examines the geometric, electronic and chemical properties of Au nanoparticles supported by reduced rutile TiO_2 (110), a potential heterogeneous catalyst system for many important reaction processes.

Scanning tunnelling microscopy (STM) has been used to examine the nucleation properties of Au nanoparticles dispersed over a reduced rutile TiO_2 (110) surface. From comparisons of the surface before and after Au deposition, and using atomic manipulation, the nucleation site of single Au atoms was directly observed to be at oxygen vacancies on the substrate ($O_{b\text{-}vacs}$). Statistical analysis of the atomic manipulation method applied provides some insight into the nature of the bonding between Au and $O_{b\text{-}vac}$ sites.

Synchrotron based X-ray photoelectron emission microscopy (XPEEM) was used, in conjunction with STM and low energy electron microscopy (LEEM), to probe the electronic character of Au nanoparticles as a function of particle size and coverage. Core-level binding energy measurements revealed a two-stage shift in Au 4f binding energy as particle size increased. This suggests electron transfer from $O_{b\text{-}vacs}$ to Au occurs for small nanoparticles on the TiO_2 (110) surface. To reduce experimental error, a method was developed for precisely patterning the substrate with discrete regions of varying Au coverage on the nanometre scale. The effects of beam induced photo-reduction of the substrate were also investigated.

High resolution electron energy loss spectroscopy was used to measure the vibrational spectrum of an Au/TiO_2 sample before and after ethanol exposure. After exposure, loss features appear that correspond to acetate, however, this is not observed for Au coverages less than 0.1-0.3 MLE. From this, it is suggested that Au has a size dependent effect on the reactivity of TiO_2 towards ethanol oxidation.

Acknowledgements

I would like to thank my supervisor, Professor Geoff Thornton, and my external contact, Professor Hicham Idriss, for their advice during my studies and for providing me with the opportunity to pursue my doctorate in such a fascinating field of research.

I am indebted to Dr Chi-Lun Pang for his invaluable guidance both in experiments and with academic writing. Also, I am especially grateful to Dr Axel Wilson for his continued support and friendship, and for keeping me sane during those long nights at the synchrotron.

Recognition must go to Drs Chi Ming Yim, Dave Grinter, Yu Zhang and Chris Muryn for teaching me so much about UHV analysis and for their help during

experiments. I would also like to acknowledge the current and former members of the nanoscience group, Daniel, George, Bobbie-Jean, Imad, Michael, Oscar and Hyun-Jin, who I have had the pleasure of working with over the last four years.

Room temperature STM measurements of Au atoms (Chapter 4, Fig. 4.3) were adapted, with permission, from unpublished work by Mr David Humphrey (thesis pending publication), for which I am thankful. I would also like to thank Drs Francesco Maccherozzi, Helder Marchetto and Sarnjeet Dhesi for their contributions to the work performed at the IO6 beamline, Diamond Light Source UK. In addition, thanks must go to Dr Khabiboulakh Katsiev and the others at the SABIC corporate research and development center for their hospitality.

I gratefully acknowledge SABIC and the EPSRC for their finding and support of my work.

I also express my gratitude to the many friends I have met during my time both in and out of UCL, particularly Jon, Emilia, Shereif and Matt for the, much-appreciated, excursions from the basement. Also, I would like to thank Dr Zhimei Du who has always been a friendly face around the department.

Vielen Dank an Anna für all die aufschlussreichen Gespräche und ihre Ermutigungen in den letzten Monaten und für ihre Geduld während der vielen langen Nächte und Wochenenden des Schreibens.

Finally, I would like to give thanks to my family: my parents, my brother and my grandparents, for nurturing my curiosity right from the beginning and giving me the drive to pursue my ambitions wherever they may take me. Without their unwavering support and enthusiasm over the years I would not be where I am today.

"An expert is someone who has made all the mistakes that can be made, in a narrow field"

– Niels Bohr

"Oft, wenn es erst durch Jahre durchgedrungen, Erscheint es in vollendeter Gestalt. Was glänzt, ist für den Augenblick geboren, Das Echte bleibt der Nachwelt unverloren."†

– Johann Wolfgang von Goethe

† Often, after years of perseverance, it emerges in a completed form. What glitters, is born for the moment. The Genuine lives on thereafter.

Glossary of Terms

µ-LEED	Micro-Low Energy Electron Diffraction
µ-XPS	Micro-X-ray Photoelectron Spectroscopy
AcAc	Acetic Acid
AES	Auger Electron Spectroscopy
BE	Binding Energy
BGS	Band Gap State
CC	Constant Current
CCD	Charge Coupled Device (Camera)
CEM	Channel Electron Multiplier
CH	Constant Height
CHA	Concentric Hemispherical Analyser
CNT	Carbon Nanotube
CVD	Chemical Vapour Deposition
DFT	Density Functional Theory
DOS	Density of States
EDX	Energy-Dispersive X-ray Spectroscopy
EELS	Electron Energy Loss Spectroscopy
eV	Electron Volt
FFT	Fast Fourier Transform

FT-IR	Fourier Transformed Infra-Red Spectroscopy
FWHM	Full Width at Half Maximum
HREELS	High Resolution Electron Energy Loss Spectroscopy
KE	Kinetic Energy
KPFM	Kelvin Probe Force Microscopy
LA	Longitudinal Acoustic Phonon Mode
LC-Au/TiO_2	Low Coverage Au/TiO_2
LDOS	Local Density of States
LEED	Low Energy Electron Diffraction
LEEM	Low Energy Electron Microscopy
LO	Longitudinal Optical Phonon Mode
LT-STM	Low Temperature Scanning Tunnelling Microscopy
MLE	Monolayer Equivalent
MS	Mass Spectrometry
PEEM	Photoelectron Emission Microscopy
PES	Photoelectron Spectroscopy
PVD	Physical Vapour Deposition
RAIRS	Reflection Adsorption Infra-Red Spectroscopy
RFA	Retarding Field Analyser
RGA	Residual Gas Analyser
SEM	Scanning Electron Microscopy
SO	Surface Optical Phonon Mode
SPLEEM	Spectroscopic Photoemission and Low Energy Electron Microscope
STM	Scanning Tunnelling Microscopy
SXRD	Surface X-ray Diffraction
TA	Transverse Acoustic Phonon Mode
TEM	Transmission Electron Microscopy
TO	Transverse Optical Phonon Mode
TPD	Temperature Programed Desorption
TSP	Titanium Sublimation Pump
UHV	Ultra High Vacuum
UPS	Ultraviolet Photoelectron Spectroscopy
UV	Ultraviolet
UV-PEEM	Ultraviolet Photoelectron Emission Microscopy
VT-STM	Variable Temperature Scanning Tunnelling Microscopy
WGS	Water Gas Shift Reaction
WKB	Wentzel-Kramers-Brillouin
XAS	X-ray Adsorption Spectroscopy
XPEEM	X-ray Photoelectron Emission Microscopy
XPS	X-ray Photoelectron Spectroscopy

Table of Contents

List of Figures

Chapter 1

Introduction

1.1 | Surface Science

The first few atomic layers of a material often exhibit properties very different to that of its bulk due to under coordination of the surface's atoms. This gives rise to variations of a surface's electronic configuration, and often results in enhanced chemical reactivity. All chemical reactions occur at interfaces, *i.e.* at surfaces. Therefore, developing a detailed understanding of surface domains is vital to furthering our knowledge of the world around us. This field of research is known as surface science. Surface science has long been tied to the development of heterogeneous catalysis, and almost all studies of crystalline catalyst systems involve the use of surface sensitive techniques. Surface science first began to emerge in the 1960's due to the development of robust, reliable vacuum technology. High vacuum conditions are usually a necessary requirement for surface analysis. The reason for this is twofold. Firstly, at low pressure the rate at which ambient gas molecules collide with the sample is minimised, preserving its surface long enough to study it without contamination. Secondly, for many spectroscopic techniques, the relatively weak signal intensity of a surface is quickly attenuated by interactions with gas molecules between the sample and analyser[1].

One of the most significant milestones in the progression of surface science was the invention of the scanning tunnelling microscope (STM) by Binnig and Rohrer in 1981[1,2]. STM has the ability to record the geometric and electronic structure of a material at the nanometre scale, allowing for an unprecedented level of surface characterisation. One further advantage of STM is that data collected is locally specific. In contrast, techniques such as low energy electron diffraction (LEED), X-ray photoelectron spectroscopy (XPS) and Auger electron spectroscopy (AES) collect spatially averaged data, and any information relating to non-periodic features, such as defects or nanoclusters, is lost.

Nanotechnology is a newly emerging field of research involving the design and fabrication of materials at nanometre scales. As with surfaces, the properties of nanomaterials are often vastly different from those of their bulk counterparts, and this trend becomes even more pronounced as particle size decreases[3]. The rise of nanotechnology has had a huge impact on a number of fields, and in some cases created new areas of research. Currently, carbon based nanostructures such as graphene or carbon nanotubes (CNT's) are being heavily researched, as are nanomaterial applications for electronic devices, gas sensing, medicine and more[4-8]. Binnig and Rohrer's STM has brought the fields of surface science and nanotechnology together by allowing scientists to examine surface reconstructions, adsorbate bonding characteristics, local surface geometry, nanoparticle distributions, thin film growth modes and surface electron distributions in detail.

1.2 | Metal Oxides

The physical properties and potential applications of metal oxides is one of the most active areas of research in surface science. Photochemistry, heterogeneous catalysis, paint pigments, electronics, resistive coatings, solar cells and gas sensing devices are just a few of the applications that rely on the effective use of these materials.

1.2.1 | Titanium Dioxide

Owing to its low toxicity, high catalytic activity and relative abundance, TiO_2 is widely studied for a range of applications including photocatalysis, gas sensing and solar cells[9-13]. TiO_2 is a reducible metal oxide that naturally occurs in

one of three polymorphic forms; rutile, anatase and bookite. Of these, rutile and anatase are by far the most chemically active, which is reflected by the number of studies concerning these systems. Rutile is the most stable and abundant of the three polymorphs and is considered to be a model metal oxide system. Because of this, rutile TiO_2 studies are often used as a basis for other metal oxides such as CeO_2 or ZnO. Detailed reviews of the numerous studies of TiO_2 have been given by Diebold, Pang *et al.*[14,15]. Rutile has a tetragonal unit cell with lattice parameters a = b = 4.58 Å and c = 2.95 Å. The (110) surface of rutile consists of alternating rows of five-fold coordinated Ti atoms (Ti_{5c}) and two-fold coordinated O atoms (O_{2c}/O_b) bridging between six-fold coordinated Ti atoms (Ti_{6c}). The Ti_{5c} and Ti_{6c} rows are connected by three-fold coordinated O atoms (O_{3c}) with all three bonds in the (110) plane. The rutile TiO_2 (110)-(1x1) surface unit cell measures 6.5 Å in the $[1\bar{1}0]$ direction and 2.95 Å in the $[001]$ direction[14]. The unit cell and (110) surface structure are shown in Fig. 1.1.

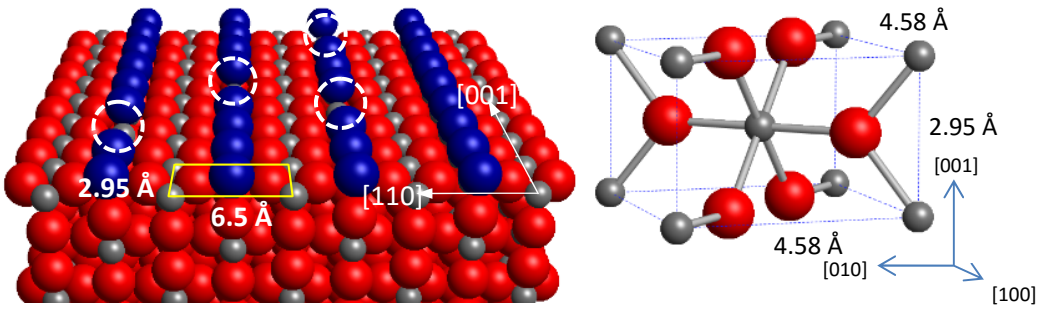

Fig. 1.1, (Left) ball model of the rutile TiO_2 (110) surface. Grey spheres correspond to Ti, red spheres to bulk O and blue spheres to bridging O atoms. Dashed circles mark $O_{b\text{-}vacs}$. The yellow rectangle indicates the surface unit cell. (Right) Crystal structure model of rutile TiO_2.

Stoichiometric TiO_2 is a wide band gap insulator (~3 eV). Vacuum annealing induces dissociation of O_b atoms from the surface causing the sample to become reduced. On reduction, a state appears within TiO_2's electronic band gap at 0.8 eV below the Fermi level. In its reduced form, the presence of an electronic state within the band-gap of the material, the so called band gap state (BGS), causes TiO_2 to become semi-conducting[16]. The transition of TiO_2 from

insulating to semiconducting can be traced by a colour change, from transparent to dark blue to black, as the sample becomes increasingly reduced. Reduced rutile TiO_2 is characterised by vacancies in the two-fold coordinated O_b rows that run across the (110) surface in the [001] direction and by interstitial Ti atoms in the bulk[14]. A ball model of the (110) surface of a reduced rutile TiO_2 crystal is shown in Fig. 1.1 (left). The presence of $O_{b\text{-}vacs}$ on TiO_2 has a dramatic effect on its chemical properties. For example, H_2O is known to dissociate at $O_{b\text{-}vacs}$ to form two bridging hydroxyl groups (OH_b) per vacancy (OH filling the $O_{b\text{-}vac}$ and H bonding to a neighbouring O_b)[17]. As TiO_2 is further reduced TiO_x clusters appear on the surface, eventually propagating along the [001] direction as 1×2 reconstructions. It has been suggested, these 1×2 reconstructions are the result of reactions between O_2 and interstitial Ti atoms on the surface, forming Ti_2O_3[14]. After annealing reduced TiO_2 in an oxygen rich atmosphere O adatoms adsorb along the Ti_{5c} rows, while $O_{b\text{-}vacs}$ appear to be 'healed' (replaced by O_b). During this process, BGS intensity diminishes, evidencing the dissociation of O_2 to form oxidised TiO_2[19].

1.3 | Gold Nanoparticles on TiO_2

In 1989, Haruta *et al.* showed that Au nanoparticles, supported by reducible metal oxides, exhibit high catalytic activity towards CO oxidation reactions[20,21]. Since then, the rate of publication for articles related to Au nanoparticle catalysis has risen year after year[14,22-26]. This finding is surprising as neither pure Au or TiO_2 alone exhibit significant catalytic activity towards CO oxidation. It has been shown that nanoparticle size has a dramatic effect on the catalytic behaviour of the Au/TiO_2 system. This suggests metal/support

interactions and/or particle size effects play a key role in catalytic reaction mechanisms.

In recent years, research into Au/TiO_2 catalysis has mainly focused on the production of hydrogen from renewable resources. Hydrogen is an important feedstock for many industrial processes, *e.g.* the Haber process, hydrogenation *etc*., and is a critical component in hydrogen fuel cell technology. Currently, the most widely used method of hydrogen production in industry is via steam reforming of fossil fuels. In this process, water vapour is reacted with hydrocarbons to produce hydrogen gas. Though this method is highly effective, there are two main drawbacks; reliance on the consumption of fossil fuels and the inherent impurity of the hydrogen produced (1-10% CO)[27]. The presence of CO is of particular concern for hydrogen fuel cell technology as it acts as a 'catalyst poison', covering all surface active sites and preventing further reactions. The Water Gas Shift reaction (WGS) is a 'clean' method for hydrogen production and a potential alternative to steam reforming of fossil fuels. In this reaction, H_2O reacts with CO over a heterogeneous catalyst as per the following reaction:

$$H_2O_{(g)} + CO_{(g)} \rightarrow H_{2(g)} + CO_{2(g)} \qquad (1.1.1)$$

Au/TiO_2 has shown great promise for WGS catalysis, and further investigation of the dynamic properties of this system could prove useful in the development of better WGS catalysts. Au/TiO_2 has also shown promise as a catalyst in organic reactions[3,10].

The fabrication of Au nanoparticles employ one of several methods. In this work, vapour deposition was used to disperse Au nanoparticles over reduced rutile TiO_2 (110) substrates. The downside of using vapour deposition is the need for a high vacuum environment, thereby removing the sample from 'real world' conditions. In the analysis of this work, this drawback must be carefully considered as surface reactivity may differ between vacuum and ambient

pressures. Despite this, surface analysis under high vacuum is essential to gain a fundamental understanding of Au/TiO_2 catalysis.

1.4 | Thesis Question and Structure

Can the Au/TiO_2 system be used as an effective heterogeneous catalyst for the production of organic species from renewable resources? To answer this question, this thesis seeks to investigate to the geometric, electronic and chemical properties of Au nanoparticles dispersed over rutile TiO_2 (110).

The thesis is further structured into 6 sections (Chapters 2-7).

Chapter 2 gives a brief overview of the theoretical considerations required to understand the basic principles of the techniques used in this work. Three main methods of sample analysis have been used: STM, XPEEM and HREELS, which are covered in detail in Chapter 2. In addition, several auxiliary experimental techniques have been employed to aid with sample preparation and analysis.

Chapter 3 details the experimental methodology and instrumentation used in this work. Sample analyses were carried out in one of three custom designed UHV systems, each housing an array of analytical equipment. In addition, the facilities at beamline IO6 of the UK synchrotron Diamond Light Source were used to collect the data presented in Chapter 5.

Chapters 4, 5 and 6 detail the experimental results collected from three separate investigations of Au/TiO_2. First, a brief outline of each experimental chapter is given. Second, an introduction reviews the relevant scientific background for each experiment and the relevance and any potential applications of the work carried out. Third, technical details of the techniques and methods employed in each chapter are described. Fourth, the data collected during each investigation is discussed in detail and interpreted in the context of the literature.

Finally, a summary of each investigation is presented, including any conclusions drawn from the experimental results.

Chapter 4 investigates the geometric structure of small Au nanoparticles in order to determine the nucleation site of single Au species on rutile TiO_2 (110). In addition, a method of Au atom manipulation is presented and subsequently used to infer the nature of the bonding between Au atoms and the TiO_2 surface.

Chapter 5 investigates the size dependent modification of the Au nanoparticle electronic configuration when dispersed on rutile TiO_2 (110), as well as the properties of electron transfer between Au and TiO_2 using synchrotron radiation.

Chapter 6 investigates the dynamics of ethanol adsorption over rutile TiO_2 (110), and the reactive properties of Au nanoparticles (with respect to acetate/acetaldehyde formation). The effects of UV light on the system are also explored.

Chapter 7 provides a brief summary of the work presented in this thesis and the key conclusions of each experimental chapter. These conclusions are then discussed in relation to the thesis question and their impact on science in the context of the literature. In addition, suggestions are made for future investigations of the Au/TiO_2 system.

1.5 | References

1. Gates, B. C. & Knözinger, H. *Impact of Surface Science on Catalysis.* (Academic Press, 2000).

2. Binnig, G. Rohrer, H. Gerber, C. & Weibel, E. Surface Studies by Scanning Tunneling Microscopy. *Phys. Rev. Lett.* **49,** 57-61 (1982).

3. Haruta, M. Yamada, N. Kobayashi, T. & Iijima, S. Gold catalysts prepared

by coprecipitation for low-temperature oxidation of hydrogen and of carbon monoxide. *J. Catal.* **115,** 301-309 (1989).

4. Geim, A. K. & Novoselov, K. S. The rise of graphene. *Nat. Mater.* **6,** 183-191 (2007).

5. Terrones, M. Science and Technology of the Twenty-First Century: Synthesis, Properties and Applications of Carbon Nanotubes. *Annu. Rev. Mater. Res.* **33,** 419-501 (2003).

6. Park, S. Vosguerichian, M. & Bao, Z. A review of fabrication and applications of carbon nanotube films-based flexible electronics. *Nanoscale* **5,** 1727-1752 (2013).

7. Sun, Y.-F. *et al.* Metal Oxide Nanostructures and Their Gas Sensing Properties: A Review. *Sensors* **12,** 2610-2631 (2012).

8. Huff, T. B. *et al.*Hyperthermic effects of gold nanorods on tumor cells. *Nanomedicine (lond).* **2,** 125-132 (2007).

9. Diebold, U. Structure and properties of TiO_2 surfaces: A brief review. *Appl. Phys. A Mater. Sci. Process.* **76,** 681–687 (2003).

10. Nadeem, M. A. *et al.* Photoreaction of ethanol on Au/TiO_2 anatase: Comparing the micro to nanoparticle size activities of the support for hydrogen production. *J. Photochem. Photobiol. A Chem.* **216,** 250–255 (2010).

11. O'Regan, B. & Grätzel, M. A low-cost, high-efficiency solar cell based on dye-sensitized colloidal TiO_2 films. *Nature* **353,** 737–740 (1991).

12. Blossey, R. Self-cleaning surfaces — virtual realities. *Nat. Mater.* **2,** 301–306 (2003).

13. Karunagaran, B., Uthirakumar, P., Chung, S. J., Velumani, S. & Suh, E.-K. TiO_2 thin film gas sensor for monitoring ammonia. *Mater. Charact.* **58,** 680–684 (2007).

14. Diebold, U. The Surface Science of Titanium Dioxide. *Appl. Surf. Sci.* **48,**

53-229 (2003).

15. Pang, C. -L., Lindsay, R. & Thornton, G. Structure of clean and adsorbate-covered single-crystal rutile TiO_2 surfaces. *Chem. Rev.* **113,** 3887-3948 (2013).

16. Yim, C. M., Pang, C. -L. & Thornton, G. Oxygen vacancy origin of the surface band-gap state of TiO_2(110). *Phys. Rev. Lett.* **104,** 36806 (2010).

17. Papageorgiou, A. C. *et al.* Electron traps and their effect on the surface chemistry of TiO_2(110). *Proc. Natl. Acad. Sci. U.S.A.* **107,** 2391-2396 (2010).

18. Du, Y. *et al.* Imaging Consecutive Steps of O_2 Reaction with Hydroxylated TiO_2(110): Identification of HO_2 and Terminal OH Intermediates. *J. Phys. Chem. C* **315,** 1692 (2007).

19. Matthey, D. *et al.* Enhanced Bonding of Gold Nanoparticles on Oxidised TiO_2(110). *Science* **315,** 1692 (2007).

20. Haruta, M., Kobayashi, T., Sano, H. & Yamada, N. Novel Gold Catalysts for the Oxidation of Carbon Monoxide at a Temperature far Below 0 °C. *Chem. Lett.* **16,** 405–408 (1987).

21. Iizuka, Y. *et al.* Adsorption of CO on gold supported on TiO_2. *Catal. Today* **36,** 115–123 (1997).

22. Park, J. B. *et al.* High catalytic activity of Au/CeOx/TiO_2(110) controlled by the nature of the mixed-metal oxide at the nanometer level. *Proc. Natl. Acad. Sci.* **106,** 4975–4980 (2009).

23. Valden, M., Lai, X. & Goodman, D. W. Onset of Catalytic Activity of Gold Clusters on Titania with the Appearance of Nonmetallic Properties. *Science* **281,** 1647–1650 (1998).

24. Cosandey, F. & Madey, T. E. Growth morphology interfacial effect and catalytic properties of Au on TiO_2. *Surf.Rev Lett.* **8,** 73 (2001).

25. Chen, M. S. & Goodman, D. W. The structure of catalytically active gold on

titania. *Science* **306,** 252–5 (2004).

26. Lai, X., Clair, T. P. S., Valden, M. & Goodman, D. W. Scanning tunneling microscopy studies of metal clusters supported on TiO_2(110): Morphology and electronic structure. *Prog. Surf. Sci.* **59,** 25–52 (1998).

27. Rodrigues, J. A. Gold-Based catalysts for the Water-gas-shift reaction: Active sites and reaction mechanism. *Catal. Today* **160,** 3-10 (2011).

2

Chapter 2

Theoretical Considerations

2.1 | Scanning Tunnelling Microscopy

In the 1980s Binnig and Rohrer worked on the development of a new form of high resolution surface microscopy, the scanning tunnelling microscope (STM)[1,2]. Since its invention, STM has revolutionised the fields of surface science, nanotechnology and heterogeneous catalysis. Using STM, it has become a routine procedure in many surface science labs to collect atomically resolved images of sample surfaces and, in some cases, directly manipulate individual surface adsorbates[3–6].

The operating principle of STM relies on quantum tunnelling of electrons, from one electrode to another, through a potential barrier. In a vacuum, the separation distance between two electrodes acts as such a potential barrier. From quantum theory, the wavefunction of an electron at the surface of an electrode does not immediately fall to zero at the potential barrier, but rather decays exponentially within it, see Fig. 2.1. Therefore, if the separation distance is small enough the wavefunction of an electron may overlap with the electronic states of the opposing electrode, allowing it to 'tunnel' through the barrier.

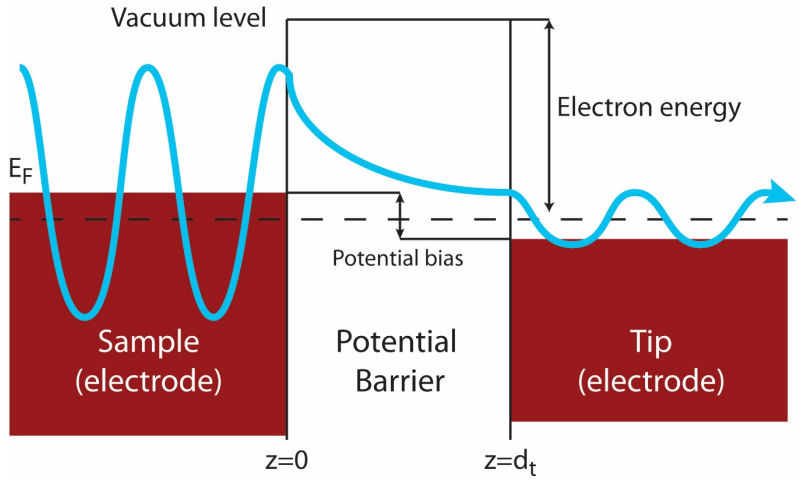

Fig. 2.1, Illustration of the 1D wavefunction of an electron tunnelling between two metal electrodes through a potential barrier of width d_t. An applied potential bias separates the Fermi levels of the two electrodes. Z - position. E_F – Fermi energy.

Quantum tunnelling is often described by the problem of an electron encountering a rectangular potential barrier in a 1D system[7]. Solving the Schrödinger equation for this system, the wavefunction of the electron, ψ, inside the barrier can be given in the form:

$$\psi \propto e^{-\kappa x}\,, \tag{2.1.1}$$

where x is the position of the electron and κ is the decay constant, given by:

$$\kappa = \frac{\sqrt{2m(V_B - E)}}{\hbar}, \tag{2.1.2}$$

where V_B is the height of the potential barrier and E and m are the energy and effective mass of the electron. In reality, the height of the potential barrier is not constant, but this approximation remains a valid in the limit of low bias voltage, *i.e.* when:

$$eV \ll \phi_s\,, \tag{2.1.3}$$

where ϕ_s is the workfunction of the sample. In the simplest case V_B is equal to the vacuum level of the system, V_o, therefore for electrons at the Fermi level[7]:

$$V_o - E = \phi\,, \tag{2.1.4}$$

In the experimental setup of STM, the sample acts as an electrode, while an atomically sharp metallic tip acts as a counter electrode. In STM, the tip, sample and distance between them are collectively known as the tunnel junction. Fig.2.2 shows a basic schematic of an STM system.

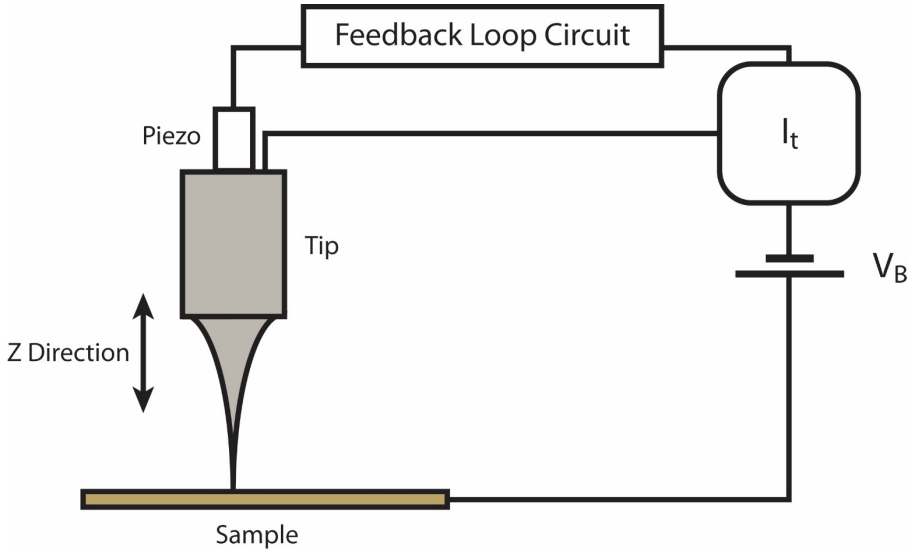

Fig.2.2, schematic diagram showing the basic STM setup and how the tunnelling current feedback loop circuit, together with the tip piezo, are used to control the position of the tip relative to the sample surface.

During STM measurements, the tip is approached to within a few Å of the sample surface. Applying a potential bias across the tunnel junction induces a flow of electrons from tip to sample (or *vice versa* depending on the polarity), which is then measured as a tunnelling current, I_t. At low potential bias and sample temperature (<300 K) I_t is related by:

$$I_t \propto e^{-2\kappa d_t}, \tag{2.1.5}$$

where d_t is the tip to sample separation distance[8,9]. From Eq. (2.1.5) it is apparent that I_t is exponentially dependent on d_t. Typically, the value of V_B is a few eV, therefore from Eq. (2.1.2) $2\kappa \approx 2\text{Å}^{-1}$. It follows, an increase in d_t by 2 Å will cause I_t to increase by an order of magnitude. From this relationship STM derives its impressive spatial resolution.

2.1.1 | Tersoff and Hamann

For the purpose of imaging surfaces, STM collects topography data by recording relative changes in I_t, rather than its absolute value. Considering this, using first-order perturbation theory, one can describe I_t by Bardeen's formalism:

$$I_t = \frac{2\pi e}{\hbar}\sum_{\mu\nu} f(E_\mu)[1 - f(E_\nu) + eV]\left|M_{\mu\nu}\right|^2 \delta(E_\mu - E_\nu)\,, \qquad (2.1.6)$$

where *f*(E) is the Fermi function, V applied bias voltage, $M_{\mu\nu}$ the tunnelling matrix between electronic states of the tip (ψ_μ) and surface (ψ_ν) and E_μ and E_ν are the energies of the tip and surface states, respectively[10,11]. Applying the limits of small bias voltage and low temperature Eq. (2.1.6) becomes:

$$I_t = \frac{2\pi}{\hbar} e^2 V \sum_{\mu\nu}\left|M_{\mu\nu}\right|^2 \delta(E_\nu - E_F)\delta\left(E_\mu - E_F\right), \qquad (2.1.7)$$

where E_F is the Fermi level.

Bardeen demonstrated that the matrix element $M_{\mu\nu}$ can be expressed as[10]:

$$M_{\mu\nu} = \frac{\hbar}{2m}\int dS \cdot (\psi_\mu^* \nabla\psi_\nu - \psi_\nu \nabla\psi_\mu^*)\,. \qquad (2.1.8)$$

Following this, Tersoff and Hamann add a further limit to their description of I_t whereby the tip is considered to be a single point probe[9]. Such a system represents an idealised situation where the tip is non-intrusive to the sample, and maximum resolution can be achieved.

This simplifies Eq. (2.1.7) such that the matrix element is proportional to the amplitude of ψ_ν at the probes position $(\vec{r}_0)$:

$$I_t \propto \sum_{\nu} |\psi_\nu(\vec{r}_0)|^2 \, \delta(E_\nu - E_F) \, . \tag{2.1.9}$$

Tersoff and Hamann's approximation shows that I_t is proportional to the surface's local density of states (LDOS) at the Fermi energy. Therefore, an STM image can be considered to be a LDOS map of a sample's surface.

2.1.2 | Chen

Tersoff and Hamann predicted that STM has a maximum spatial resolution of ~6 Å[11]. However, in 1989 experimental observations demonstrated the possibility of achieving a resolution as low as 2 Å[12]. In 1990, Chen proposed a new model to explain this discrepancy between theory and experiment[13]. He suggested that the s wave approximation used by Tersoff and Hamann is likely invalid for most experiments as STM tips are usually fashioned from d-band metals such as tungsten, platinum-iridium or gold. Chen observed that the DOS at the Fermi level of a d-band metal tip are mainly constructed of d electron states. In addition, it is often considered that surface d states of tungsten tips tend to form highly localised dangling d_{z^2} orbitals, which extend into the vacuum. These states are expected to play a major role in the tunnelling of such tips. Chen also introduced a reciprocity principle into his model[13]. This demonstrates that on an s wave surface scanned by a d_{z^2} tip is equivalent to a d_{z^2} surface scanned by an s wave tip, as illustrated in Fig.2.3.

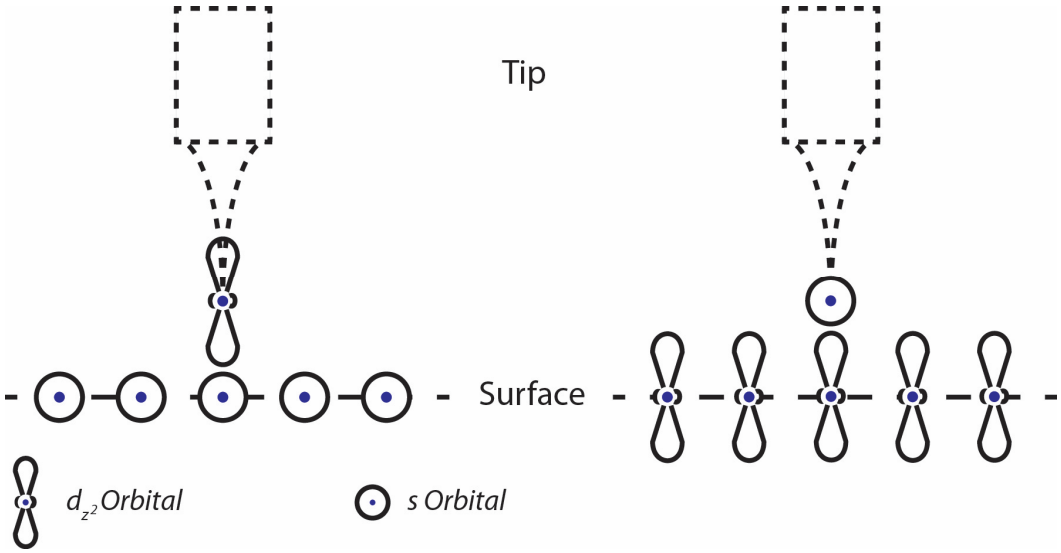

Fig.2.3, diagram illustrating the STM reciprocity principle introduced by Chen. This demonstrates that scanning an s orbital terminated surface with a d_{z^2} terminated tip is equivalent to scanning a d_{z^2} orbital terminated surface with an s terminated tip[13].

Applying his refined model, Chen estimated the tip-to-sample distance during STM ~4-6 Å[13]. Within this separation, covalent bonds may form between tip and sample due to the oscillation of electrons between them. Using voltage pulses, Lyo and Avouris have shown that this is indeed the case by inducing atom transfer from the surface of an Si sample to an STM tip[14].

2.1.3 | Lang

Interactions between a sample's surface and adsorbates on that surface are expected to disturb the LDOS distribution of the substrate material. Because STM effectively maps a surface's LDOS, it is reasonable to expect adsorbates to appear as distortions in STM images. This principle has been explored by Lang who, via theoretical calculations, investigated how a sample's LDOS is affected by various adsorbates[15–17]. Using Bardeen's formalism, Lang calculated the DOS for a system consisting of a sodium atom (tip) and a single species (adsorbate), where each is present on a flat electrode substrate.

Lang's work shows Na 3s and S 2p resonances cause increases in the LDOS at the Fermi level, creating what appear to be protrusions in STM images. In contrast, He atoms resulted in a decrease in the LDOS at the Fermi level, and therefore appear as depressions in STM images. This effect is illustrated in Fig.2.4. Lang's observations highlight the fact that interpretation of STM images is non-trivial, as image features do not arise solely from the topography of the sample. Therefore, STM analysis is often supported by theoretical calculations, *e.g.* simulated images[18–21].

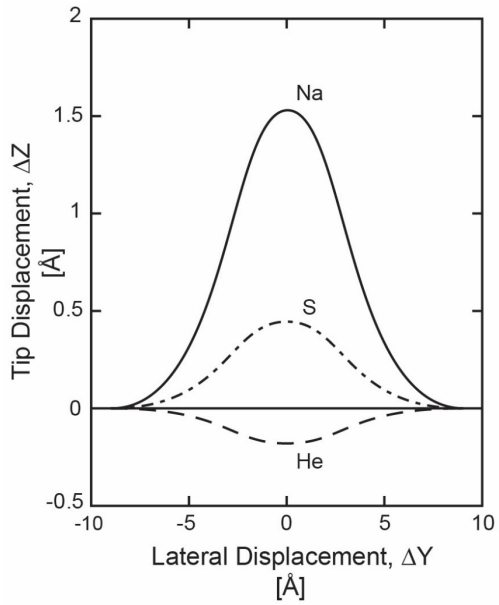

Fig.2.4, plot showing STM tip displacement as a function of lateral movement over a flat electrode surface with an adsorbed Na, S or He atom, as calculated by Lang et al. Adapted from Lang[16].

2.1.4 | WKB Approximation

Typically, in STM experiments of metal oxides a sample/tip bias voltage in the range of 1-3 eV (or even higher) is applied. Recalling Tersoff and Hamman theory, it is apparent that for many cases the approximation of low bias voltage is not valid when studying oxides[11]. Where the low bias approximation is no longer suitable, it is necessary to consider the range of electron states below E_F that contribute to I_t. In such situations, the semi-classical Wentzel-Kramers-Brillouin

(WKB) approximation provides a reasonable model of the system[9]. The WKB approximation calculates the probability of an electron tunnelling between two planar electrodes at 0 K. The resulting value of I_t is an integral over the energy range available for tunnelling, which includes both filled and empty electron states, given by:

$$I_t = \int_0^{eV} \rho_s(r,E)\rho_t(r,\pm eV,\mp E)T(E,eV,r)\,dE\,, \qquad (2.1.10)$$

where ρ_s (r, E) and ρ_t (r, E) are the density of states of the sample and tip respectively at location r and energy E (measured with respect to their Fermi levels). Upper and lower signs in Eq. (2.1.10) correspond to positive and negative sample bias respectively. T is the transition probability for an electron with energy E and bias voltage V at tip sample separation d_t, given by:

$$T\,(d_t,E,V) = exp\left(-\frac{2d_t\sqrt{2m}}{\hbar}\sqrt{\frac{\phi_s+\phi_t}{2}+\frac{eV}{2}-E}\right). \qquad (2.1.11)$$

Eq. (2.1.10) sums over all filled and empty state pairs that contribute to I_t in the given energy range. It is worth noting, however, that T is at a maximum when E= 0, *i.e.* at the Fermi level of the emitter. Therefore, electron states closest to the Fermi energy of the tip/sample give the largest contribution to I_t[22].

2.2 | High Resolution Electron Loss Spectroscopy

High resolution electron energy loss spectroscopy (HREELS) is a type of electron spectroscopy used to probe electronic features at the surface of a sample, *e.g.* phonons, plasmons, electron transitions etc[23]. In addition, HREELS can be used to investigate the molecular vibrational spectrum of a surface. During HREELS, a well-defined monochromatic beam of electrons is directed towards a sample at a specific angle of incidence. As incoming electrons reach the sample they are scattered from its surface towards an electron energy analyser, where their kinetic energy is measured. The energy difference between incident and scattered electrons is recorded on a computer. By plotting energy difference (loss) as a function of signal intensity, an energy loss spectrum is generated.

Analyser design is a key factor in HREELS. Until the early 1990's HREELS spectrometers were typically capable of an energy resolution of ~10 meV. In 1993 Ibach *at al.* pioneered a new type of electron analyser capable of resolutions as low as 1 meV, which has been refined to 0.5 meV or better in the years since[24–26]. The data collected by HREELS is often comparable to that of reflection adsorption infra-red spectroscopy (RAIRS). RAIRS is a method of sensitive IR spectroscopy used to collect vibrational spectra from single crystal surfaces. Despite significant improvements in HREELS design, RAIRS is typically capable of greater resolutions (0.1 meV) while being less technically complicated to implement[27,28]. For this reason, RAIRS is a more widely implemented technique than HREELS, however HREELS does have some advantages over RAIRS. Firstly, RAIRS is confined to collecting data within the spectral range of infra-red light, while HREELS is capable of scanning a much broader energy range, limited only by the maximum beam energy of the system. Secondly, while RAIRS is only sensitive to dipole excitations, HREELS can detect signals induced by both dipole and non-dipole excitations. This is particularly useful as dipole induced excitations

are restricted by a set of selection rules that do not apply to non-dipole excitations.

2.2.1 | Electron Scattering

In HREELS, most incident electrons are elastically scattered by the sample and reflected back at an angle equal to their angle of incidence. This is known as the specular angle (direction). In addition to those scattered elastically, a minority of electrons are scattered inelastically after interacting with the sample surface. The energy transferred between incoming electrons and the surface has a well-defined value, E_s, which is dependent on the exact scattering mechanism that occurs. E_s is given by:

$$E_s = E_i - \hbar\omega \,, \qquad (2.2.1)$$

where E_i is the incident electron energy and $\hbar\omega$ is the energy of the excited surface state[29]. There are several mechanisms by which electrons can be inelastically scattered from a surface. These are grouped into three main categories; dipole scattering, impact scattering and resonance scattering. Dipole scattering is typically the strongest of these interactions and produces the most intense loss features in HREEL spectra.

2.2.1.1 | Dipole Scattering

The dielectric medium of a crystal can be perturbed by both external electric fields and intrinsic oscillations of the crystal's own atomic/electronic structure (*e.g.* phonons/plasmons). The oscillating potential generated by these processes is known as a dipole oscillation[30]. During HREELS, electrons incident on a sample are deflected away from the specular direction by dipole oscillations in a process known as dipole scattering.

During the approach of an incident electron, the electric field of the sample does work on it causing an inexorable energy loss. Assuming a specific angle of approach and that the charge distribution at the surface is constant, the potential seen by the incoming electron is given by:

$$\Phi(x) = \Phi_0 \, e^{-k_{\parallel}|z|} e^{ik_{\parallel} \cdot x_{\parallel}}, \qquad (2.2.2)$$

where Φ_0 is the initial potential at the surface (without any incoming electrons), z is the perpendicular distance between the electron and the sample (*i.e.* z = 0 at the surface of the sample) and $x_{\parallel}$ is the wave vector component of the incoming electron parallel to the surface[31]. $k_{\parallel}$ is the wave vector of the excited mode parallel to the surface, given by:

$$k_{\parallel} = k_{i\parallel} - k_{s\parallel}, \qquad (2.2.3)$$

where $k_{i\parallel}$ and $k_{s\parallel}$ are the wave vectors of the incident and scattered electron, respectively. From Eq. (2.2.2) it is apparent that the potential felt by an incoming electron decays exponentially as z increases, and only excitations with small $k_{\parallel}$ values will have meaningful potentials at large distances from the surface. As $k_{\parallel}$ is typically much smaller than $k_{i\parallel}$ and $k_{s\parallel}$, dipole scattered electrons do not deviate far from the specular direction.

In the case of an external electric field, *i.e.* polar surface adsorbates, the presence of a dipole on a surface induces an opposing 'image' charge in the substrate, as shown in Fig.2.5. If a dipole is orientated perpendicular to a surface the induced dipole oscillation extends a relatively long distance from the sample (~10 nm). However, for a dipole lying parallel to a surface the image charge of the sample will almost completely cancel out the field of the induced dipole oscillation at large distances. Perpendicular dipole oscillations begin to interact with the electric field of an incoming electron long before it reaches the surface

of a sample, thereby creating measurable loss peaks in HREEL spectra. In contrast, the much shorter interaction between a parallel dipole oscillation and incoming electron does not usually give rise to detectable losses in HREELS.

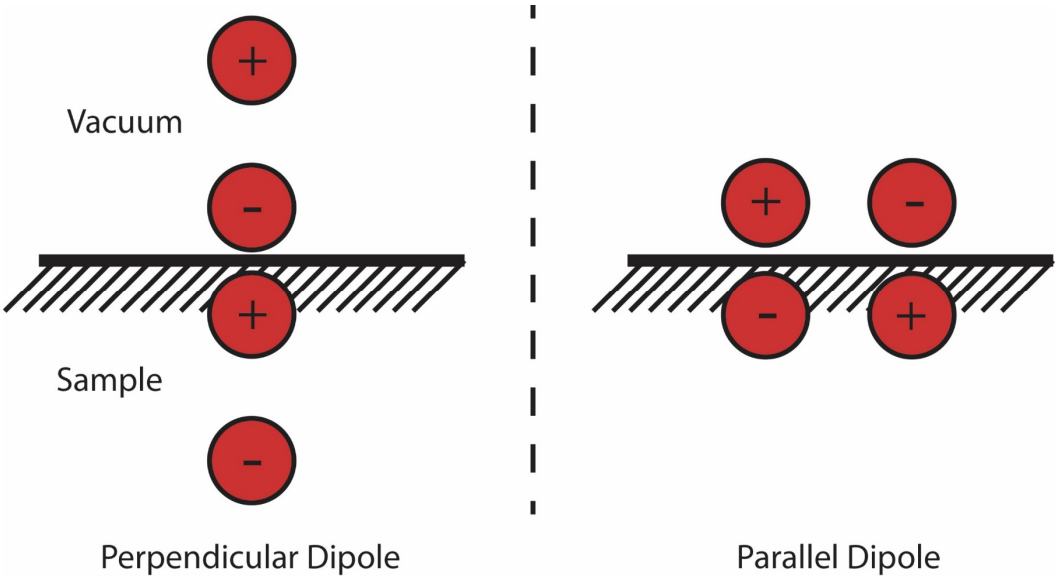

Fig.2.5, diagram illustrating the image charge induced in a sample by a surface dipole orientated either perpendicularly or parallelly to the surface plane.

This is the basis of the dipole selection rule of surface vibrational spectroscopy[29]. Due to the restriction of charge carriers, semiconductors and insulating materials produce less effective image charges than those of metal systems. This results in a relaxation of the dipole selection rule for semiconductors and insulators. Subsequently, parallel dipole oscillations may produce detectable losses in HREELS measurements of such systems. Due to the possible relaxation of the dipole selection rule, HREELS alone cannot be used to determine molecular orientation on semiconductor or insulator surfaces[29].

In addition to dipole scattering, HREELS can also detect non-dipole scattered electrons. In spectra, non-dipole scattering modes are typically much less intense, and often overlap with, dipole modes. During measurements, the strong angular dependence of dipole scattering can be exploited to improve the visibility of non-dipole modes. By measuring at an off-specular angle, dipole mode

intensity will reduce relative to that of non-dipole modes, making them more easily distinguishable in resulting spectra.

2.2.1.2 | Impact Scattering

Impact scattering involves short range interactions between incoming electrons and atomic nuclei at the surface of a crystal[32]. Because only short range interactions are involved, impact scattered electrons have a wider angular distribution from the sample, and so the specular direction does not have a special significance. The orientation of surface excitations has no influence over the scattering cross section of impact scattered electrons. As such, analysis of impact scattered electrons allows HREELS to probe dipole forbidden excitations as dipole selection rules no longer apply. The scattering cross section of impact scattered electrons increases as their incident energy increases, therefore higher beam energies are required to obtain reasonable signal intensity. HREELS resolution is inversely linked to the incident energy of the electron beam used. This means, a compromise must be made between signal intensity and spectral resolution during impact scattering measurements.

To explain the underlying mechanism of impact scattering in more detail a complex quantum mechanical analysis is required. For the purposes of this work, such an in-depth analysis is unnecessary. The reader is directed to chapter 3 of “Electron Energy Loss Spectroscopy and Surface Vibrations” (Ibach and Mills) for more information[29].

2.2.1.3 | Resonance Scattering

Negative ion resonance scattering is a particular case of impact scattering whereby surface adsorbed molecules capture incoming electrons, temporarily forming negative ions in the process[29]. This occurs when an incoming electron’s energy matches the ionisation energy of an adsorbate on the surface. Typically,

negative ion states generated in this way have a lifetime between 10^{-10} and 10^{-15} s, after which the captured electron is reemitted. This causes increased loss intensity at the energy of the emitted electron in HREEL spectra. A detailed review of negative ion resonance scattering is given by Palmer *et al*[33].

2.2.2 | Intrinsic Energy Losses

In addition to losses arising from extrinsic factors, *i.e.* surface adsorbates, crystal systems also generate a number of intrinsic energy loss signals in HREELS. The most significant of these are phonon, plasmon and inter/intra band excitations[29].

2.2.2.1 | Phonon Losses

A phonon is the term given to the elastic wave that propagates through a crystal lattice as its atoms vibrate. The wave vector, k, of a phonon in a 3D lattice, with a basis, has 3N normal modes where N is the number of atoms in the basis[29]. The in-phase oscillation of atoms in the primitive cell of a crystal is called an acoustic phonon. In the long wavelength limit, acoustic phonons decay linearly with k. Acoustic phonon modes account for three of the 3N normal modes of a 3D lattice. The remaining 3N-1 modes, where the atoms of the primitive cell oscillate out of phase, are called optical phonons. Because ions are moving in phase (in the same direction), acoustic phonons do not generate significant electric fields. In contrast, the out of phase movement of ions in an optical phonon produces localised dipole oscillations, which interact strongly with external electric fields. Optical phonons are conceptually similar to molecular vibrations. In spectra, optical phonon peaks are broadened by intercellular interactions and appear as frequency bands. Unlike acoustic phonons, optical phonon frequencies depend more on non-k dependent factors, such as angle strain or force constants, and therefore do not diminish with k (in the long wavelength limit). The dependence

of a phonon's frequency on k is shown in Fig.2.6 for an N = 2 system, this is called a phonon dispersion curve[34]. The large fluctuation in frequency, and decay to 0 as k approaches 0, seen in Fig.2.6 clearly illustrates the dependence that acoustic modes have on k. In contrast, optical phonon modes remain relatively flat. In addition to optical and acoustic modes, phonons can be further split into longitudinal and transverse waves. For a given system there are:

- 1 × Longitudinal acoustic phonon (LA)
- 2 × Transverse acoustic phonons (TA)
- N-1 × Longitudinal optical phonons (LO)
- 2(N-1) × Transverse optical phonons (TO)

For systems where N >2 (*e.g.* TiO_2) the corresponding phonon dispersion curve is much more complicated but the same basic principles apply.

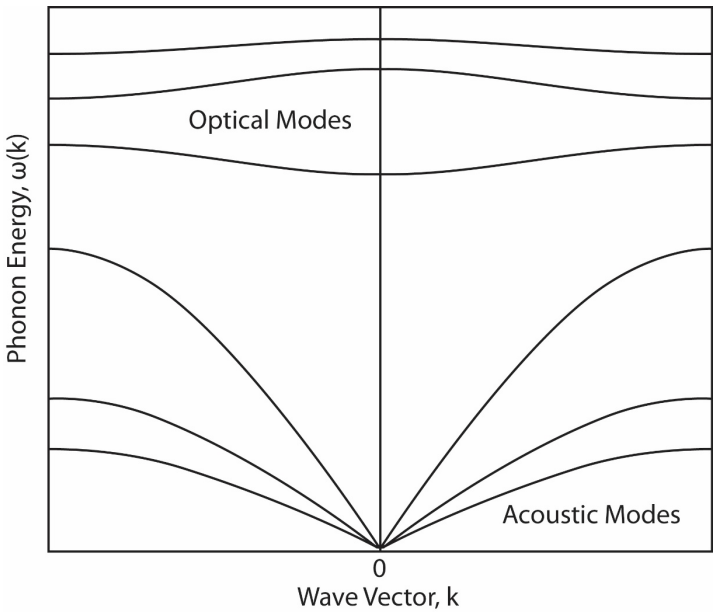

Fig.2.6, diagram showing the phonon dispersion curve of an N = 2 system. Optical and acoustic phonon modes have been labelled accordingly. Adapted from Chang[34].

Optical phonons are usually defined by their dielectric function, ε(ω). Within the long wavelength limit, this is given by:

$$\varepsilon(\omega) = \varepsilon_{\infty} + \sum_{j=0}^{n} \frac{\Delta\varepsilon_j \omega_j^2}{\omega_j^2 - \omega^2 + i\omega\gamma_j}, \qquad (2.2.4)$$

where ε_∞ is the high frequency limit of ε(ω), $\Delta\varepsilon_j$ is the difference between ε_∞ and the low frequency limit of ε(ω), ω_j is the frequency of the j^{th} transverse optical mode and γ_j is the j^{th} damping factor (associated with anharmonic affects). ε(ω) is the dielectric function of the system at frequency ω, which has both real and imaginary parts:

$$\varepsilon(\omega) = \varepsilon' + i\varepsilon''. \qquad (2.2.5)$$

Eq. (2.2.4) describes the variation of a system's dielectric properties with applied electric field. Considering the tensor properties of an anisotropic system, the dielectric function of a crystal system may have up to 9 different components. This can be written in the form:

$$\varepsilon(\omega) = \begin{bmatrix} \varepsilon_{xx} & \varepsilon_{xy} & \varepsilon_{xz} \\ \varepsilon_{yx} & \varepsilon_{yy} & \varepsilon_{yz} \\ \varepsilon_{zx} & \varepsilon_{zy} & \varepsilon_{zz} \end{bmatrix}. \qquad (2.2.6)$$

To describe a uniaxial crystal system, such as TiO_2, only three distinct values of its dielectric function are required (ε_{xx}, ε_{yy} and ε_{zz}). ε_{xx} and ε_{yy} are equivalent, therefore this can be further simplified to two components; one perpendicular, $\varepsilon_\perp$ ($\varepsilon_{xx}/\varepsilon_{yy}$), and one parallel, $\varepsilon_\parallel$ (ε_{zz}), to the C-axis[35]. To describe the system $\varepsilon_\perp$ and $\varepsilon_\parallel$ must be treated separately. For the optical phonons of an ionic system, the movement of differently charged ions relative to each other induces strong

dipole oscillations within the bulk of the material. Phonon derived dipole oscillations interact strongly with external electric fields, like that of an approaching electron, and often produce intense signals in HREEL spectra.

The interaction between incoming electrons and the electric field above the surface of a crystal is related to the probability, P(ω, k), of an electron exciting a surface mode with energy $\hbar\omega$ and wave vector k. This probability is given by[35]:

$$\mathrm{P}\,(\omega,\,\mathrm{k}) = \frac{4e^2\mathrm{k}}{\pi^2 h v_\perp^2[\mathrm{k}^2 + (\frac{\omega}{v_\perp})^2]^2}\,\mathrm{Im}\frac{-1}{\varepsilon(\omega)+1}, \qquad (2.2.7)$$

where $v_\perp{}^2$ is the velocity component of the incoming electron perpendicular to the surface. Fig.2.7 shows the two dielectric function components of TiO_2, plotted as a function of frequency[34]. From these dielectric function plots, information can be derived about the energies of TiO_2's optical phonons. From Eq. (2.2.7), the probability of a loss occurring is at a maximum when:

$$\mathrm{Re}[\varepsilon(\omega)] = 0\,. \qquad (2.2.8)$$

In Fig.2.7, LO and TO modes are indicated by points at which the curve crosses the x-axis with positive and negative gradient, respectively. In HREELS, surface optical (SO) phonon modes are detected, rather than LO or TO modes. SO modes were first described by Fuchs and Kliewer in 1965, hence their alternate name F-K modes[36]. SO phonons arise from changes in electrostatic potential of a system as its periodicity is terminated in one direction, *i.e.* at its surface.

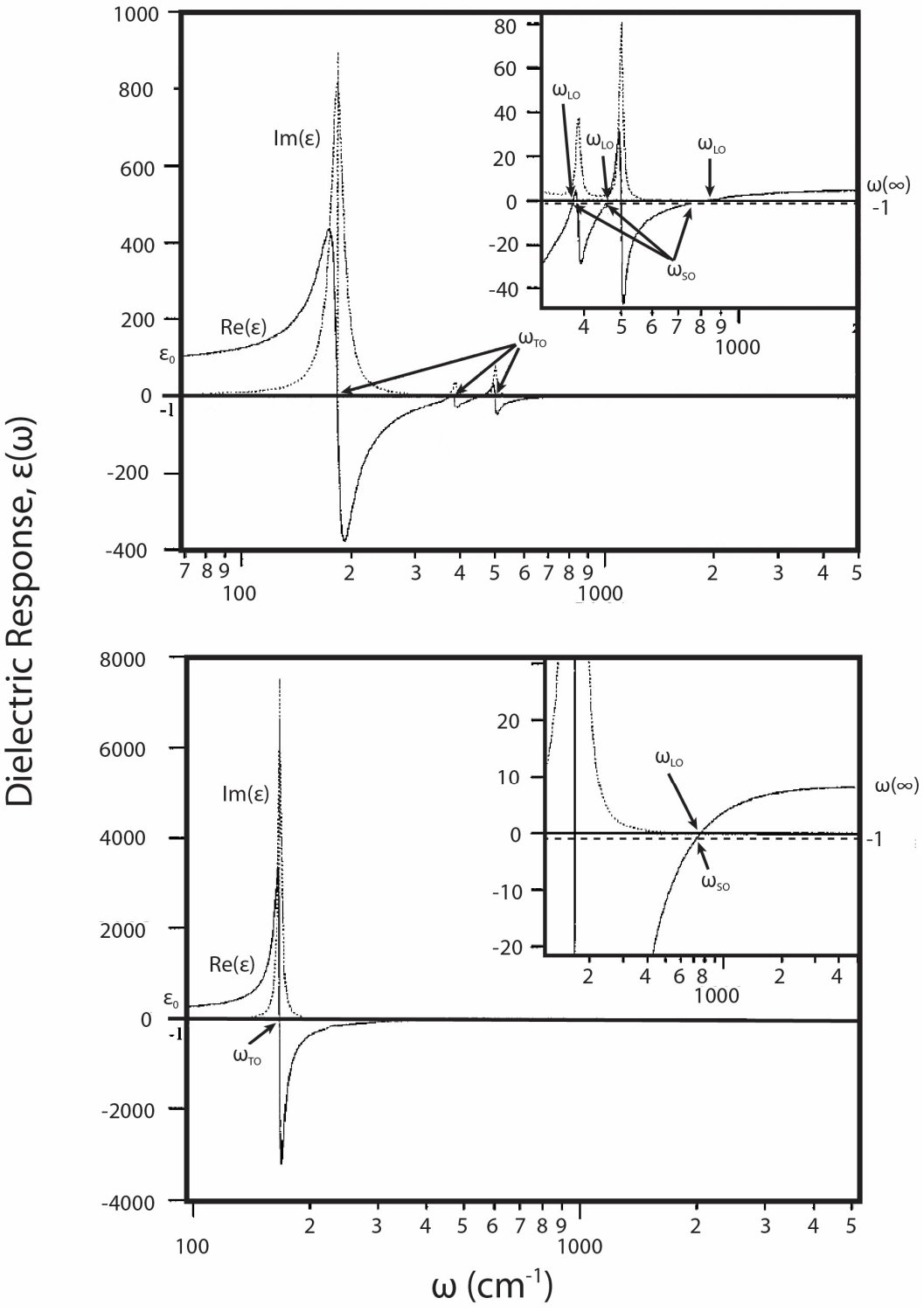

Fig.2.7, plot showing calculated parallel and perpendicular dielectric function components of TiO_2 as a function of frequency. From this data, TO, LO and SO phonon modes of TiO_2 can be determined and have been labelled in the figure. Taken from Chang[34].

For SO modes there is a maximum loss probability for each region between an LO and TO mode of the bulk (*i.e.* $\omega_{TO} < \omega_{SO} < \omega_{LO}$), where:

$$\mathrm{Re}[\varepsilon(\omega)] = -1 \, . \qquad (2.2.9)$$

In Fig.2.7 there are 4 points that satisfy this condition, however, at the first point Im[ε(ω)] is at a maximum. Eq (2.2.7) shows that loss probability is inversely dependent on Im[ε(ω)], therefore the probability of a loss signal appearing when Im[ε(ω)] is at a maximum is negligible. SO phonon loss peaks appear in HREEL spectra at energies as low as 10 meV[37]. For this reason, a resolution of 10 meV or better is essential for studying SO phonon modes, otherwise signals may be lost beneath the elastic peak.

Fuchs *et al.* first predicted the appearance of an SO phonon mode for ZnO, and the position of this mode was later confirmed by Ibach and Mills at 68.8 meV[29,36]. Fuchs further predicted that the frequency of an SO phonon mode, ω_{SO}, can be related to that of a corresponding bulk TO mode, ω_{TO}, by the following equation:

$$\omega_{SO} = \left[\frac{(\varepsilon_0 + 1)}{(\varepsilon_\infty + 1)}\right]^{\frac{1}{2}} \omega_{TO} \, , \qquad (2.2.10)$$

where ε_0 and ε_∞ are the low and high frequency limits of the dielectric function, respectively[36]. In addition to this, Ibach *et al.* confirmed that SO loss intensity is inversely proportional to the energy of the incident electrons[29]. At low energies, incoming electrons may have a kinetic energy close to the excitation energy of the SO phonon modes. In such a case, alternate scattering mechanisms are more influential, and the dependence of SO loss intensity on beam energy no longer holds.

In addition to the loss peaks, anti-stokes gain peaks are also observed in HREELS. The ratio of gain and loss peak intensity, I_{gain}/I_{loss}, is given by:

$$\frac{\mathrm{I}_{gain}}{\mathrm{I}_{loss}} = e^{\frac{\hbar\omega_s}{K_b T}}, \tag{2.2.11}$$

where ω_s is the fundamental frequency of the excited surface mode.

2.2.2.2 | Plasmon Losses

In conducting solids, the term plasma refers to the cloud of free electrons permeating the lattice of the system, and the collective oscillation of these electrons is called a plasmon. The oscillating charge density of a plasmon will interact with the electric field of an incoming electron. Plasmons propagate through both the bulk of a material and along its surface. The electric field of an incoming electron can interact with, and subsequently excite, the surface plasmons of a sample, producing loss features in HREEL spectra[31]. Surface plasmons are typically observed for metallic substrates. However, semi-conductor materials, and even nanoparticles, with a sufficient density of nearly-free charge carriers can also generate plasmons.

The dielectric function of a plasmon can be approximated using the Drude dielectric function of a free electron gas[38,39]:

$$\varepsilon(\omega) = \varepsilon_\infty \frac{-ne^2}{\mu\varepsilon_o\omega^2}. \tag{2.2.12}$$

where n is the number of oscillators, μ is the effective mass, e is the dynamic charge of the oscillators and ε_o is the permittivity of free space[29]. Applying the same rules used to determine the loss probability of phonons in the bulk

(Re[ε(ω)] = 1) and at the surface (Re[ε(ω)] = -1) of a sample, Flavel *et al.* deduced the following expression relating surface, ω_S, and bulk, ω_B, plasmon frequencies[40]:

$$\frac{\omega_S}{\omega_B} = \left(\frac{\varepsilon_\infty}{\varepsilon_\infty + 1}\right)^{\frac{1}{2}}. \qquad (2.2.13)$$

From the above equation one can conclude that surface plasmons typically have lower frequencies than their bulk counterparts.

2.2.2.3 | Inter-/Intra-band Transition Losses

During HREELS measurements, incoming electrons can induce inter and intra-band electron transitions, *e.g.* excitation from the valence to the conduction band of a semi-conductor. These excitations appear in HREEL spectra as broad loss peaks with an intensity independent of scattering angle[31].

2.2.3 | Fourier Deconvolution

The interaction between SO phonon modes and incident electrons in HREELS is very strong for ionic substrates. Therefore, HREEL spectra of metal oxides are typically dominated by very intense SO phonon mode peaks. The large dipole moments of metal oxides give rise to a high probability of exciting a single SO mode multiple times. This process appears in spectra as a series of overtones of the primary (single electron excitation) phonon loss peaks. Such overtones are termed multiple loss peaks[41]. In HREELS of TiO_2 and other metal oxides, multiple loss peaks often appear in the molecular vibrational frequency range of the spectrum[42–44]. As SO phonon loss peaks are typically much more intense than molecular vibrational peaks, accurately identifying vibrational features is almost impossible in raw HREEL spectra. Background subtraction is one method

employed to solve this issue. A measurement of the substrate, taken prior to molecular exposure, is subtracted from the spectrum collected after exposure. Background subtraction has been used by D'Amico *et al*. for investigations of ZnO exposed to CO, however with limited success [45]. In 1985, Cox *et al.* developed an alternate method for removing multiple loss peaks from HREEL spectra using Fourier deconvolution[46]. They determined that multiple loss peaks follow a Poisson distribution. Therefore, for an HREEL spectrum described by s(ω):

$$\mathrm{s}(\omega) = \mathrm{i}(\omega) * \left[\delta(0) + \mathrm{p}(\omega) + \frac{1}{2!}\mathrm{p}(\omega) * \mathrm{p}(\omega) + \frac{1}{3!}\mathrm{p}(\omega) * \mathrm{p}(\omega) * \mathrm{p}(\omega) + \cdots\right], \tag{2.2.14}$$

where $\delta(0)$ describes the elastic peak, p(ω) is the probability of a single loss occurring and i(ω) represents the instrumental broadening factor. The instrumental broadening factor is taken as a Gaussian with an FWHM equal to that of the elastic peak (*i.e.* the instrumental resolution). Denoting Fourier transformation of A(τ) to a(ω) as:

$$A(\tau) \leftrightarrow a(\omega), \tag{2.2.15}$$

and using the relationship:

$$A(\tau)\, B(\tau) \leftrightarrow a(\omega) * b(\omega), \tag{2.2.16}$$

one can express the Fourier transformed HREEL spectrum as:

$$S(\tau) = I(\tau)\left(\sum_{n=0}^{\infty} \frac{P(\tau)^2}{n!}\right). \tag{2.2.17}$$

The term inside the brackets is a Taylor expansion of e^x, therefore Eq. (2.2.17) can be re-written as:

$$S(\tau) = I(\tau)e^{P(\tau)} \,. \tag{2.2.18}$$

Rearranging Eq. (2.2.18) yields:

$$P(\tau) = \ln \frac{S(\tau)}{I(\tau)}, \tag{2.2.19}$$

where P(τ) represents the electron energy loss function free of multiple losses. Due to noise and steps in the raw HREEL data, applying an inverse Fourier transformation to Eq. (2.2.19) can cause Fourier ripples to appear in the resulting spectrum. To avoid this, a smoothing function, I'(τ), is applied prior to inverse Fourier transformation, giving the deconvolution formula:

$$P(\tau) = I'(\tau) \ln \left(\frac{S(\tau)}{I(\tau)} \right), \tag{2.2.20}$$

which can then be inverse Fourier transformed to give:

$$I'(\tau) \ln \left(\frac{S(\tau)}{I(\tau)} \right) \leftrightarrow p(\omega) * i'(\omega) \,. \tag{2.2.21}$$

In the work presented here (see chapter 6), a combination of background subtraction and Fourier deconvolution has been employed to allow vibrational spectroscopy analysis of a rutile TiO_2 sample using HREELS. During deconvolution, a Gaussian, with FWHM equal to that of the elastic peak +2 meV, was generated and used as a smoothing function.

2.3 | Low Energy Electron Diffraction

In 1937, Davidson and Thompson received the Nobel prize in physics for the development of low energy electron diffraction (LEED)[47]. Since then, LEED has become a widely employed technique for determining the surface structure and ordering of single crystal samples[27,48,49]. Over the years, technological developments have made LEED an easy addition to most UHV based instruments. As a result, in conjunction with other techniques such as STM, XPS, SXRD, UPS and AES, LEED is often used as an auxiliary method of surface characterisation.

In LEED, a monochromatic beam of low energy electrons, typically 20-300 eV, is directed towards a sample[50]. Electrons incident on the sample are elastically scattered at discrete angles in a radial distribution. To avoid a build-up of excess charge, it is important that the sample is grounded. After scattering from the surface, electrons are passed through a series of grids that act to filter out any lower energy (inelastically scattered) electrons. Finally, scattered electrons strike a fluorescent screen causing light to be emitted at the point of impact. The higher the electron intensity at a single point the brighter that point will fluoresce, thereby creating a pattern of discrete spots on the screen. From the wave particle duality of electrons, the de Broglie wavelength, λ_e, of an electron beam can be calculated via the de Broglie equation:

$$\lambda_e \frac{h}{\sqrt{2m_e E}}, \tag{2.3.1}$$

where m_e is the effective mass of an electron and:

$$\mathrm{E} = \mathrm{e} \cdot \mathrm{V}, \tag{2.3.2}$$

where V is the accelerating voltage applied to the electron beam and e is the elementary charge. Using eq. (2.3.1), the de Broglie wavelength of an electron beam with energy in the range of 20-200 eV is between 2.74 and 0.87 Å. Such a wavelength is of the same order of magnitude as the interatomic spacing in a crystal lattice making LEED an ideal technique for probing the atomic structure of a material.

The angular distribution of electrons scattered by a sample is governed by the conditions for Bragg diffraction from a periodic array[50]. This is illustrated in Fig.2.8 for two parallel electron beams incident on a 1D lattice of atoms.

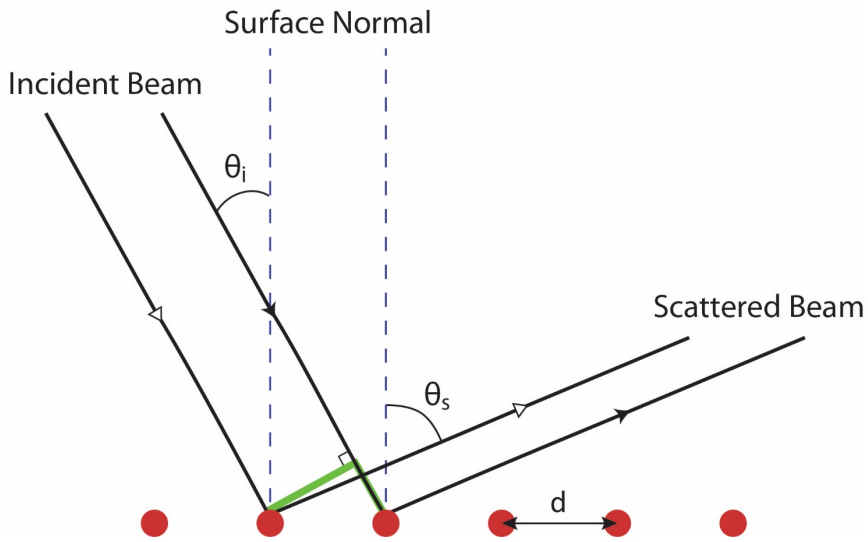

Fig.2.8, diagram illustrating the scattering of two parallel electron beams incident on a 1D periodic array. The interatomic lattice spacing of the array is given by d. θ_i and θ_s represent the angle of the incident and scattered beams respectively (normal to the surface).

The path difference of the two incident beams, ΔS, is given by:

$$\Delta S = \mathrm{d}(\sin\theta_s - \sin\theta_i)\,, \tag{2.3.3}$$

where d is the interatomic spacing of the 1D lattice, and θ_i and θ_s are the angles of the incident and scattered electrons (normal to the surface), respectively. In

the case of an incoming electron beam normal to the surface, Eq. (2.3.3) simplifies to:

$$\Delta S = \mathrm{d}(\sin\theta_s)\,. \tag{2.3.4}$$

Scattered electrons interfere constructively or destructively with each other. From Bragg's law, complete constructive interference occurs when d is equal to an integer multiple, n, of the de Broglie wavelength, λ, of the incident electrons, *i.e.* when:

$$\Delta S = n\lambda\,. \tag{2.3.5}$$

For a system with a large number of scatterers, as is the case for a real sample, diffracted electron intensity is only significant when Eq. (2.3.5) is satisfied. This results in discrete maxima in the scattered electron intensity at certain angles. In LEED, this is known as a diffraction pattern. From Eq. (2.3.4) it is apparent that d and sinθ have an inversely proportional relationship. Therefore, the diffraction pattern projected onto the LEED screen is inversely proportional to the interatomic spacing of the sample.

For experimental techniques, the proportion of information derived from a sample's surface, compared to the bulk, is described as its surface sensitivity. Surface sensitivity is a critical factor when collecting data for surface science investigations. Electrons moving through a crystal lattice can be scattered elastically or inelastically, and as the path of an electron through the sample increases so does its inelastic scattering probability. Due to the inexorable energy loss of each inelastic scattering event, an energy dependent attenuation of the incident electrons occurs as a function of their penetration depth through the sample. The electron penetration depth, as a function of kinetic energy, has been experimentally determined for various materials (see Fig. 2.9)[51]. From Fig. 2.9, the average mean free path of an electron through a sample, within the energy range

10-1000 eV, is <10 Å, demonstrating that LEED (20-300 eV) is a highly surface sensitive technique.

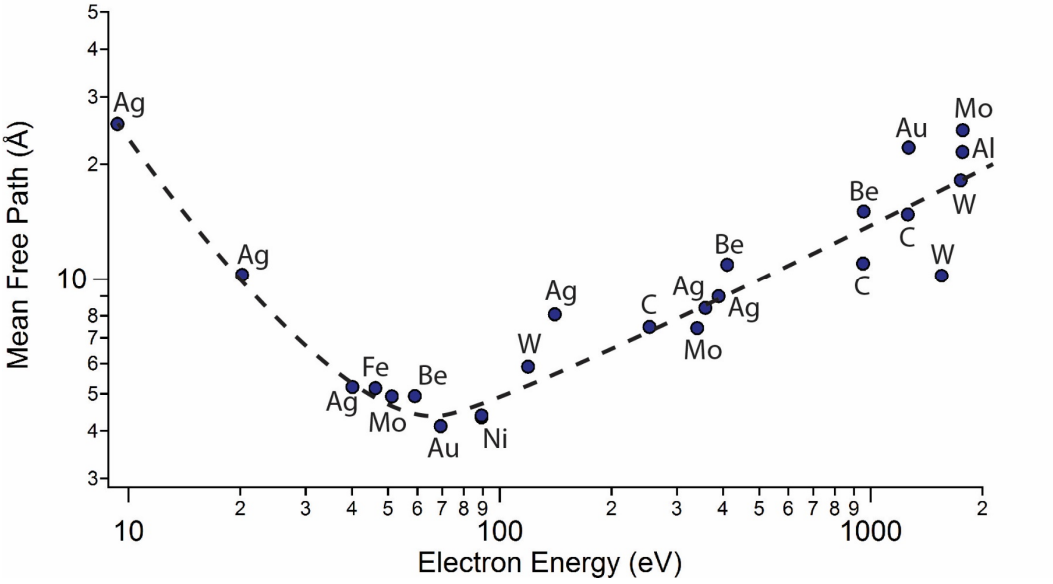

Fig. 2.9, plot showing the average inelastic mean free path of electrons through a sample as a function of electron energy. Points represent the individual peaks obtained from photoelectron spectra of the various elements labelled. Fig. adapted from J. B. Hudson's, Surface Science an Introduction[51].

2.4 | Auger Electron Spectroscopy

Auger electron spectroscopy (AES) is a widely-used technique for determining the elemental composition of a sample's surface. AES was first discovered in 1923 by Lise Meitner, and also independently by Pierre Auger in 1925[52]. Technologically, as with LEED, AES is relatively simple to implement and can be incorporated into the design of most LEED optics. The underlying mechanism of the Auger process is illustrated in Fig.2.10.

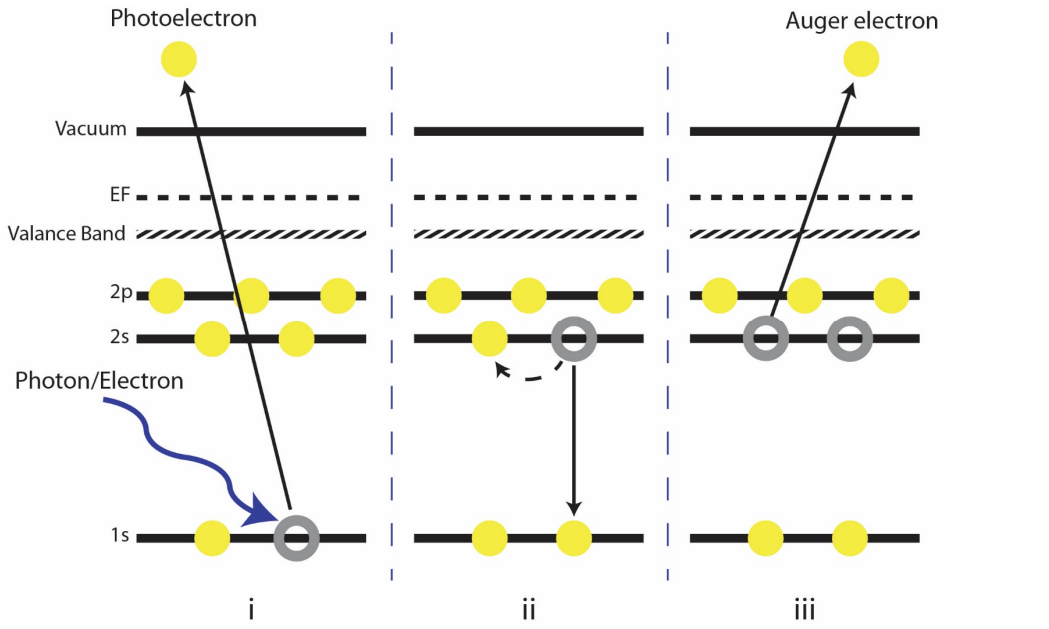

Fig.2.10, Diagram illustrating the Auger process. i shows the initial emission of an electron into the vacuum following excitation of a sample by an incident photon/electron beam. In ii the relaxation of a second electron into the hole left by the first is followed by the transference of energy to a third electron. The emission of the third electron into the vacuum, as an Auger electron, is shown in iii.

In the first step of the process, an electron/photon incident on a surface induces excitation, and subsequent photoemission, of a core level electron (this is the same process that occurs in photoelectron spectroscopy). Next, a higher energy electron (with lower binding energy to the atom) relaxes into the hole left by the emitted electron. As the second electron transitions from higher to lower energy level, the excess energy, ΔE, may be emitted as a photon. The emitted photon has

an energy equal to the energy difference between the initial energy levels of the first and second electrons. In the case that a photon is not emitted, the excess energy is instead passed to a third electron, called the Auger electron, that is then emitted into the vacuum[53]. The energy of the Auger electron, E_o, is given by:

$$\mathrm{E}_o = E_K - E_{L1} - E_{L2,3} - \phi \,, \tag{2.4.1}$$

where ϕ is the workfunction of the detector. E_K, E_{L1} and $E_{L2,3}$ represent the binding energies of the three electrons in their initial states (subscripts denote the energy level from which each electron originated). The energy of the Auger electron is dependent on the exact electronic structure of its parent atom and is therefore an elementally specific quantity. All elements with >2 electrons produce characteristic AES signatures, which can be used as a fingerprint in composition analysis.

Similar to LEED, AES uses a monochromatic beam of electrons, with tuneable energy, to induce the Auger process. Electron beam energies used are typically in the range of 500-2000 eV. although less surface sensitive than LEED, AES spectra are derived from the first few atomic layers of a sample (~10 Å)[51].

AES performed in this work employed a detection method known as retarding field analysis (RFA). The RF analyser is, for the most part, physically identical to the setup used for LEED. Auger emitted electrons pass through a series of four grids before striking a screen/detector. Unlike with LEED, the total electron intensity incident on the screen is recorded as a current. The first and last grids of the detector are grounded to create a field free region between the sample and the screen. The two central grids, called the retarding grids, act to filter out low energy electrons before they encounter the screen. A potential is applied to the retarding grids that decelerates all electrons that pass through them. Subsequently, electrons with a kinetic energy less than the retarding potential are filtered out. In principle, it is possible to create an Auger system using only two grids between the screen and the sample. In this case, the grid

closest to the sample is grounded and the grid closest to the screen acts as a retarding grid[51]. The advantage of the four-grid system is that the addition of the extra grounded and retarding grids improves the signal-to-noise ratio and spectral resolution of the analyser, respectively.

During AES, the current measured from the screen is proportional to the electron flux passing through the retarding grid at potential V_o. This current corresponds to the signal intensity of the electrons with energy E_o where:

$$E_o = e \cdot V_o \,. \tag{2.4.2}$$

Spectra are plotted by recording signal intensity as a function of E_o.

2.5 | X-ray Photoelectron Spectroscopy

X-ray Photoelectron Spectroscopy (XPS) is a surface sensitive technique used to obtain information about both the chemical identity and electronic configuration of a sample's surface[54]. The theoretical principle of XPS is based on the photoelectric effect, first discovered by Hertz in 1887 that involves the emission of core level electrons from a sample following photoexcitation[55]. This process is illustrated in Fig.2.11. In XPS, a monochromatic beam of X-rays, with energy hν, is used to illuminate the sample. Most commonly, X-rays are generated using a Mg or Al filament (producing photons at 1253.6 (Mg Kα) or 1486.6 eV (Al Kα) respectively)[56]. If hν is greater than the binding energy, BE, of a core level electron to its nucleus (relative to the Fermi level), that electron will be excited to the vacuum level, and subsequently emitted from the sample. The resultant photoelectron has a kinetic energy, KE, equal to the difference between hν and BE (minus the workfunction difference of the detector and the sample) *i.e.*:

$$\mathrm{KE} = \mathrm{h}\nu - \mathrm{BE} - (\phi_s - \phi_a)\,, \tag{2.5.1}$$

where ϕ_s and ϕ_a are the workfunctions of the sample and analyser, respectively. For conducting materials, the Fermi levels of the sample and analyser align and the term ϕ_s in Eq. (2.5.1) is negligible. For insulating materials, surface charging can occur due to the photoexcitation of the sample. In this case, (ϕ_s - ϕ_a) is often estimated by locating the spectral line of a known species present on the sample (typically Au or Ag) or using the Fermi edge. Core level binding energies are elementally specific values that can be used as a fingerprint in chemical analysis of a sample. By recording their kinetic energy, the calculated binding energy of a photoelectron can be used to determine the chemical composition of a sample. Binding energy shifts of a material can be explained by changes in the electronic configuration of the material, and such chemical shifts can be used to determine

the chemical state of the sample. In XPS spectra s orbital electrons give rise to singlet electron intensity peaks whereas, due to spin orbital splitting, p, d and f electrons produce doublets. For p, d and f doublets the peak separation and intensity ratios are well known for most elements and can be used to aid elemental identification.

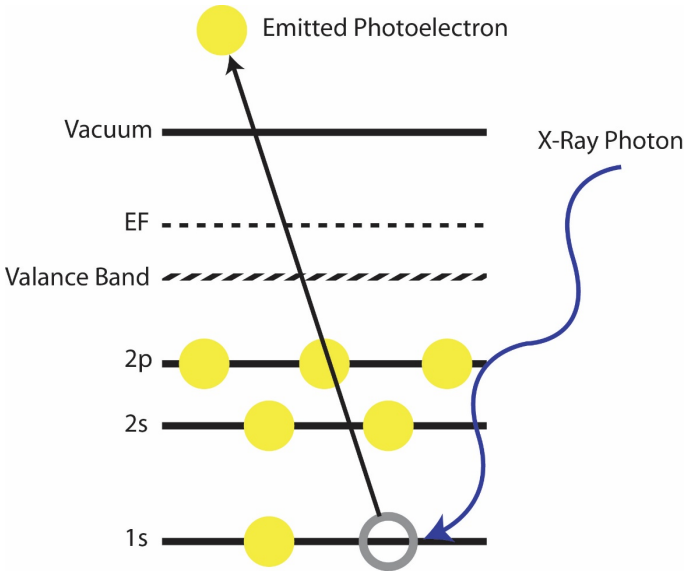

Fig.2.11, diagram showing the photoelectric effect whereby an electron (photoelectron) is emitted into the vacuum following excitation by an incident photon. In XPS, core level photoexcitation is achieved by illuminating a sample with X-ray photons of sufficient energy.

The mean free path of photons through a sample far exceeds that of electrons, and photoionization of a sample will occur a few µm beneath the surface. Despite this, due to inelastic scattering, photoemitted electrons only originate from the first few atomic layers (on the order of ~10 Å). From this, XPS exhibits relatively high surface sensitivity. This is further improved by orienting the analyser at a grazing angle of incidence to the sample. This reduces the intensity of photoelectrons reaching the analyser, but increases their path through the sample, thereby reducing the depth from which they originate.

Typically, XPS uses an electrostatic concentric hemispherical analyser (CHA), which consists of two concentric hemispherical metal plates with an electric field applied between them[57]. Electrons entering one side of the analyser are directed towards an electron detector at the other side. If the KE of the

electrons is too large (too small) the incoming electrons collide with the outer (inner) hemisphere of the analyser due to the applied electric field. In this way, only electrons within a specific KE range reach the detector. In addition to this, an exit slit is inserted to 'cut' the dispersed beam and further filter the energy of the electrons reaching the detector. By varying the applied field, the photoelectron intensity is measured as a function of KE and can be plotted to yield a photoelectron spectrum of the sample. Briggs and Grant give a thorough guide to XPS including detailed explanations of the instrumentation used[57].

2.6 | Photoelectron Emission Microscopy

In the 1930's, Brüche demonstrated the use of a two aperture electrostatic lens system for obtaining high resolution images of the surface of a heated, planar, electron-emitting cathode[58]. Following this, it was found that the addition of a simple magnetic lens to this setup facilitated surface imaging without the need to heat the sample[59]. This method of imaging surface via photoemitted electrons is known as photoelectron emission microscopy (PEEM). Due to the technological constraints of the time, PEEM was not widely implemented until the 1980s following advancements in synchrotron radiation and UHV design. The realisation of PEEM as a method for chemically mapping surfaces at high resolution represents a key milestone in the fields of surface science and nanotechnology[60–63]. Unlike similar techniques, such as EDX, PEEM has the advantage of being highly surface specific, a vital characteristic when studying thin films, nanostructured materials and molecular reactions at surfaces.

In PEEM analysis, variable contrast is used to illustrate the photoelectron yield obtained from each pixel in an image (brighter areas indicate higher yield). Photoelectron yield is dependent on three factors[64,65]:

- the excitation probability of the sample;
- the mean free path of electrons through the sample lattice; and
- the local workfunction at the sample surface.

From these factors PEEM derives its chemical and structural sensitivity and as such is a powerful tool for identifying surface domains on samples. In addition, workfunction altering effects are sometimes exploited in PEEM to track chemical reactions on surfaces, *e.g.* changes in adsorbate electron distributions during surface catalysed reactions.

The photon energy used in PEEM is typically between 20-300 eV. Due to the inelastic mean free path of electrons in this energy range, this makes PEEM a highly surface sensitive technique (see the section on LEED in this chapter for more information). This is further improved by applying a retarding field prior to the electron analyser, which effectively filters out lower energy electrons originating from deeper in the sample.

2.6.1 | Modes of PEEM

PEEM has several modes of operation commonly distinguished by the photon energy used and the method by which photoelectrons are collected for analysis.

In UV-PEEM, UV light is used to induce photoemission. This PEEM mode is often used as a non-spectroscopic technique solely for imaging purposes. The advantage of UV-PEEM over other modes of operation is that it is much more technologically simple to implement, however, there is no chemical specificity in the information obtained[66].

In contrast to UV-PEEM, XPEEM utilises, higher energy soft X-rays to illuminate the sample. Photons in this energy range can induce elementally specific core level photoemission, thereby allowing for elemental composition analysis. Subsequently, binding energy spectra (like those collected during XPS) can be generated from XPEEM for each area imaged. XPEEM can be further divided into three main methods of data collection; X-ray absorption spectroscopy (XAS), energy filtered imaging microscopy and μ-XPS[67].

2.6.1.2 | X-ray Absorption Spectroscopy

XAS utilises energy tuneable X-rays produced by a synchrotron. During XAS measurements, the incident photon energy is swept through a range of values. If

the incident energy is lower than the binding energy of a core level electron on the surface then no photoemission can occur, appearing as a dark region in XAS images. If the incident energy is equal to, or greater than, a core level electron's binding energy a resonance is observed in the emission of electrons excited by secondary processes, appearing as a bright region in XAS images. This resonance originates from the excitation of core level electrons to previously unoccupied valence states, caused by the filling of core holes following the initial photoemission. As the photon energy increases so will the emission of secondary electrons from the sample, so corresponding images appear increasingly brighter. By measuring the total electron yield of a material, calculated via the elementally specific absorption coefficient, one can determine the chemical identity of different regions in XAS images. Using XAS, it is possible to determine several features of a species such as its valence/chemical state and adsorption site[67,60].

2.6.1.3 | Energy Filtered Imaging Microscopy

Rather than using variable energy photons, as with XAS, energy filtered imaging microscopy uses a fixed energy photon beam to induce photoemission. In addition to the usual setup, an energy filter is applied to the electron analyser so that only electrons of a chosen energy are detected. Also, a contrast aperture is inserted from which a surface image is resolved from the beam of photoemitted electrons. A series of images are recorded while the energy filter is swept through a range of values. Each pixel in the resulting images will appear bright where the photoemission energy of the surface atoms matches the band pass energy of the filter. By sweeping the band pass energy of the analyser, different areas will appear to light up depending on their chemical identity. Using this methodology complex nanostructured surface features can be identified and characterised[67,60].

2.6.1.4 | μ-XPS

Operating XPEEM in μ-XPS mode is conceptually similar to conventional XPS, however, spectra are collected from a much smaller area of the surface. Similar to energy filtered imaging microscopy, μ-XPS uses a photon beam of fixed energy while a variable band pass filter is applied[67]. No exit slit is applied to the energy filter, and the last two lenses of the microscope are set to project the dispersive plane of the filter directly onto the detector. Dispersive plane images appear as a straight line with varying contrast. The horizontal position and brightness of each point on the line corresponds to the binding energy and signal intensity of the dispersed photoemitted electrons, respectively. By taking a line profile of a dispersive plane image, one can produce a photoemission spectrum for the given energy window, like those collected during conventional XPS. The spatial resolution of the technique is set by inserting a field limiting aperture into the path of the photoemitted electrons, and in this way μ-XPS can collect spectra from an area as small as 2 μm.

It is worth pointing out, that while recording μ-XPS it is not possible to also collect images of the surface simultaneously. For this reason, μ-XPS is usually used in conjunction with other imaging techniques or PEEM modes. The advantage of μ-XPS over other modes of operation is its superior energy resolution, an important factor when measuring small core level binding energy shifts[68].

2.6.2 | LEEM and LEED

By incorporating a standard electron gun into the design of the conventional PEEM setup, the instrument can be adapted to collect LEED and LEEM (low energy electron microscopy) data[67,68]. In LEEM mode, an energy selected monochromatic beam of electrons is directed towards the sample. The energy of the incident electron beam can be tuned by controlling the potential difference between the sample and the cathode of the electron gun. Electrons

elastically scattered by the sample are directed towards the analyser with incident and reflected electrons passing through an objective lens. The objective lens focuses incident electrons into a plane wave while also decelerating them to low energy. After elastic scattering from the sample, reflected electrons pass back through the objective lens and are re-focused and accelerated in the process. The periodic lattice of a crystal confines elastically scattered electrons to specific angles of emission from the surface (see the section in this chapter on LEED)[51]. Electrons emitted at the same angle have constructive interference with a maximum in signal intensity when the following condition is satisfied:

$$\mathrm{d}\sin\theta = n\lambda\,, \tag{2.6.1}$$

where d is the interatomic spacing of the crystal lattice, θ is the angle of the scattered electron normal to the surface, λ is the de Broglie wavelength of the electron beam and n is an integer. A beam splitter is used to redirect the scattered electrons through an imaging column, which also incorporates a contrast aperture. The resulting image is magnified and projected onto the detector to produce a highly resolved (typically a few nm) LEEM image of the surface. By removing the contrast aperture from the imaging column a conventional LEED pattern of the surface is projected onto the detector instead. The main benefit of LEEM imaging over PEEM arises from the low energy of the incident electrons used, *i.e.* LEEM can achieve high surface sensitivity while causing minimal sample damage.

2.7 | References

1. Binnig, G., Rohrer, H., Gerber, C. & Weibel, E. Surface Studies by Scanning Tunneling Microscopy. *Phys. Rev. Lett.* **49,** 57–61 (1982).

2. Binnig, G. *et al.* Tunneling through a controllable vacuum gap Tunneling through a controllable vacuum gap. *Appl. Phys. Lett.* **40,** 178 (1982).

3. Eigler, D. M. & Schweizer, E. K. Positioning single atoms with a scanning tunnelling microscope. *Nature* **344,** 524–526 (1990).

4. Meyer, G., Phel, S. Z. & Rieder, K. H. Manipulation of atoms and molecules with a low temperature scanning tunneling microscope. *Appl. Phys. A* **63,** 557–564 (1996).

5. Adam, O. A. O. *et al.* Single-atom manipulation of Co embedded in Cu(001) surfaces. *Japanese J. Appl. Physics, Part 1 Regul. Pap. Short Notes Rev. Pap.* **45,** 2014–2017 (2006).

6. Hla, S. STM Single Atom / Molecule Manipulation and Its Application to Nanoscience and Technology. *J. Vac. Sci. Technol. A Vacuum, Surfaces, Film.* **23,** 1–12 (2005).

7. Chen, C. J. *Introduction to Scanning Tunneling Microscopy*. *Oxford University Press* (Oxford University Press, 1993).

8. Wiesendanger, R. *Scanning Probe Microscopy and Spectroscopy: Methods and applications*. (Cambridge University Press, 1994).

9. Bonnell, D. W. *Scanning Probe Microscopy and Spectroscopy. Theory, Techniques, and Applications. Journal of the American Chemical Society* (Wiley-VCH, 2001).

10. Bardeen, J. Tunnelling from a Many-Particle Point of View. *Phys. Rev. Lett.* **6,** 57–59 (1961).

11. Tersoff, J. & Hamann, D. R. Theory of the scanning tunneling microscope. *Phys. Rev. B* **31,** 805–813 (1985).

12. Wintterlin, J. *et al.* Atomic-Resolution Imaging of Close-Packed Metal Surfaces by Scanning Tunneling Microscopy. *Phys. Rev. Lett.* **62,** 59–62 (1989).

13. Chen, C. J. Origin of atomic resolution on metal surfaces in scanning

tunneling microscopy. *Phys. Rev. Lett.* **65,** 448–451 (1990).

14. Lyo, I.-W. & Avouris, P. Field-Induced Nanometer- to Atomic-Scale Manipulation of Silicon Surfaces with the STM. *Science (80).* **253,** 173–176 (1991).

15. Lang, N. D. Spectroscopy of single atoms in the scanning tunneling microscope. *Phys. Rev. B* **34,** 5947–5950 (1986).

16. Lang, N. D. Theory of Single-Atom Imaging in the Scanning Tunneling Microscope. *Phys. Rev. Lett.* **56,** 1164–1167 (1986).

17. Lang, N. D. Vacuum tunneling current from an adsorbed atom. *Phys. Rev. Lett.* **55,** 230–233 (1985).

18. Okazaki-Maeda, K., Maeda, Y., Morikawa, Y., Tanaka, S. & Kohyama, M. Study of Interaction between Au and TiO_2(110) at Low Coverage. *Mater. Trans.* **47,** 2663–2668 (2006).

19. Rønnau, A. A Closer Look at the TiO_2 (110) Surface with STM. *Adsorpt. J. Int. Adsorpt. Soc.* **2,** 103 (2003).

20. Nilius, N. *et al.* Formation of One-dimensional electronic states along the step edges of CeO_2(111). *ACS Nano* **6,** 1126–1133 (2012).

21. Fu, Q. & Wagner, T. Interaction of nanostructured metal overlayers with oxide surfaces. *Surf. Sci. Rep.* **62,** 431–498 (2007).

22. Nilius, N. Properties of oxide thin films and their adsorption behavior studied by scanning tunneling microscopy and conductance spectroscopy. *Surf. Sci. Rep.* **64,** 595–659 (2009).

23. Erskine, J. L. High-resolution electron energy loss spectroscopy. *Crit. Rev. Solid State Mater. Sci.* **13,** 311–379 (1987).

24. Ibach, H. Electron energy loss spectroscopy with resolution below 1 meV. *J. Electron Spectros. Relat. Phenomena* **64,** 819–823 (1993).

25. Ibach, H., Balden, M. & Lehwald, S. Recent advances in electron energy

loss spectroscopy of surface vibrations. *J. Chem. Soc. Faraday Trans.* **92,** 4771–4774 (1996).

26. Ibach, H., Rajeswari, J. & Schneider, C. M. An electron energy loss spectrometer designed for studies of electronic energy losses and spin waves in the large momentum regime, **123904,** (2011).

27. Raval, R. *et al.* FT-rairs, EELS and LEED studies of the adsorption of carbon monoxide on Cu(111). *Surf. Sci.* **203,** 353–377 (1988).

28. Greenler, R. G. *A Comparison of the Reflection -Absorption Infrared Method with the Electron Energy Loss Method for Studying Vibrations at Surfaces*. (Springer US, 1982).

29. Ibach, H. & Mills, D. L. *Electron energy loss spectroscopy and surface vibrations*. (Academic Press, 1982).

30. Ibach, H. *Electron Spectroscopy for Surface Analysis*. (Springer-Verlag, 1977).

31. Thiry, P. A., Liehr, M., Pireaux, J. J. & Caudano, R. Electron Interaction Mechanisms in High Resolution Electron Energy Loss Spectroscopy. *Phys. Scr.* **35,** 368 (1987).

32. Soriaga, M. P., Chen, X., Li, D. & Stickney, J. L. High Resolution Electron Energy-Loss Spectroscopy. *Encycl. Inorg. Chem.* (2008).

33. Palmer, R. E. & Rous, P. J. Resonances in electron scattering by molecules on surfaces. *Rev. Mod. Phys.* **64,** 383–440 (1992).

34. Chang, Z. Adsorbate studies at Ti02 surfaces and metal/TiO_2 interfaces using vibrational spectroscopies. (1999).

35. Henrich, V. E. & Cox, P. A. in *The Surface Science of Metal Oxides* (Cambridge University Press, 2000).

36. Fuchs, R. & Kliewer, K. L. Optical Modes of Vibration in an Ionic Crystal Slab. *Phys. Rev.* **140,** A2076-A2088 (1965).

37. Balden, M., Lehwald, S. & Ibach, H. Substrate and hydrogen phonons of the ordered p(2×1) and (2×2) phase and of the anomalous (1×1) phase of hydrogen on W(110). *Phys. Rev. B* **53,** 7479–7491 (1996).

38. Drude, P. Zur Elektronentheorie der Metalle. *Ann. Phys.* **306,** 566–613 (1900).

39. Drude, P. Zur Elektronentheorie der Metalle; II. Teil. Galvanomagnetische und thermomagnetische Effecte. *Ann. Phys.* **308,** 369–402 (1900).

40. Cox, P. A., Egdell, R. G., Eriksen, S. & Flavell, W. R. The high-resolution electron-energy-loss spectrum of TiO_2(110). *J. Electron Spectros. Relat. Phenomena* **39,** 117–126 (1986).

41. Henderson, M. a. An HREELS and TPD study of water on TiO_2(110): the extent of molecular versus dissociative adsorption. *Surf. Sci.* **355,** 151–166 (1996).

42. Henderson, M. A., Otero-Tapia, S. & Castro, M. E. The chemistry of methanol on the TiO_2(110) surface: the influence of vacancies and coadsorbed species. *Faraday Discuss.* **114,** 313–329 (1999).

43. Henderson, M. a. Acetone Chemistry on Oxidized and Reduced TiO_2(110). *J. Phys. Chem. B* **108,** 18932–18941 (2004).

44. Qiu, H., Idriss, H., Wang, Y. & Wöll, C. Carbon−Carbon Bond Formation on Model Titanium Oxide Surfaces: Identification of Surface Reaction Intermediates by High-Resolution Electron Energy Loss Spectroscopy. *J. Phys. Chem. C* **112,** 9828–9834 (2008).

45. D'Amico, K. L., McFeely, F. R. & Solomon, E. I. High resolution electron energy loss vibrational studies of carbon monoxide coordination to the (10.hivin.10) surface of zinc oxide. *J. Am. Chem. Soc.* **105,** 6380–6383 (1983).

46. Cox, P. A., Flavell, W. R., Williams, A. A. & Egdell, R. G. Application of Fourier transform techniques to deconvolution of HREEL spectra. *Surf. Sci.*

152, 784–790 (1985).

47. Pleijel, H. *Nobel Lectures, Physics 1922-1941*. (Elsevier Publishing Company, 1965).

48. Farmer, J. Ag Adsorption on Reduced CeO_2(111) Thin Films. *J. Phys. Chem. C* **2,** 17166–17172 (2010).

49. Stroscio, J. A., Bare, S. R. & Ho, W. The chemisorption and decomposition of ethylene and acetylene on Ni(110). *Surf. Sci.* **148,** 499–525 (1984).

50. Woodruff, D. P. & Delchar, T. A. *Modern Techniques of Surface Science*. (Cambridge University Press, 1994).

51. Hudson, J. B. *Surface Science an Introduction*. (Butterworth-Heinemann, 1992).

52. Hardouin Duparc, O. Pierre Auger – Lise Meitner: Comparative contributions to the Auger effect. *Int. J. Mater. Res.* **100,** 1162–1166 (2009).

53. Chattarji, D. *The Theory of Auger Transitions*. (Academic Press Inc, 1976).

54. van der Heide, P. in *X-Ray Photoelectron Spectroscopy* 1–12 (John Wiley & Sons, Inc., 2011).

55. Hertz, H. Ueber einen Einfluss des ultravioletten Lichtes auf die electrische Entladung, *Ann. Phys.* **276,** 983 (1887).

56. Briggs, D. & Seah, M. P. *Practical surface analysis*. *Journal of Chemical Technology & Biotechnology* (John Wiley & Sons, Ltd., 1992).

57. Briggs, D. & Grant, J. T. *Surface analysis by Auger and x-ray photoelectron spectroscopy*. *Surface and Interface Analysis* (IM Publications, 2004).

58. Brüche, E. Elektronenmikroskopische Abbildung mit lichtelektrischen Elektronen. *Zeitschrift für Phys.* **86,** 448–450 (1933).

59. Bauer, E. A brief history of PEEM. *J. Electron. Spectrosc. Relat. Phenom.* **185,** 314–322 (2012).

60. Locatelli, A. & Bauer, E. Recent advances in chemical and magnetic imaging of surfaces and interfaces by XPEEM. *J. Phys. Condens. Matter* **20,** 93002 (2008).

61. Grinter, D. C. *et al.* Oxidation state imaging of ceria island growth on Re(0001). *J. Phys. Chem. C* **117,** 16509–16514 (2013).

62. Grinter, D. C. *et al.* Spectromicroscopy of a model water-gas shift catalyst: Gold nanoparticles supported on ceria. *J. Phys. Chem. C* **118,** 19194–19204 (2014).

63. McArthur, S. L. Thin films of Vanadium Oxide Grown on Vanadium metal. *Surf. Interface Anal.* **38,** 1380–1385 (2006).

64. Pianetta, P. *et al.* Core level photoelectron microscopy with synchrotron radiation. *Rev. Sci. Instrum.* **60,** 1686–1689 (1989).

65. Dover, C. Synchrotron Studies of Technologically Important Metal Oxide Surfaces. (PhD thesis, University College London, 2014).

66. Hawkes, P. W. & Spence, J. C. H., Science of Microscopy (Springer New York, 2007).

67. Bauer, E., Photoelecron microscopy. *J. Phys. Condens. Matter,* **13,** 11391-11404 (2001).

68. Schmidt, T. *et al.* SPELEEM: Combining LEEM and Spectroscopic Imaging. *Surf. Rev. Lett.* **5,** 1287–1296 (1998).

3

Chapter 3

Instrumentation

3.1 | Ultra High Vacuum

Sample cleanliness is a critical factor when studying the reactive surfaces of materials. By interaction with the surrounding environment, a sample's surface may become completely contaminated before any surface analysis can be performed. To maximise the timeframe of a sample's viability, it has become standard practice in surface science to conduct experiments under high vacuum conditions. Most commonly, a sample is introduced into an ultra-high vacuum (UHV) chamber, with an environmental pressure in the range of 10^{-9} to 10^{-10} mbar, housing an array of analytical instrumentation.

Surface impingement rate, Z_A, is a measure of the number of gas molecules striking a surface in a given timeframe, and is defined by the Hertz-Knudsen equation[1]:

$$Z_A = \frac{P}{\sqrt{(2\pi m k_B T)}} \tag{3.1.1}$$

where P is the pressure of the system, m is the mass of the impinging atom/gas, k_B is the Boltzmann constant and T is the temperature of the system. By calculating Z_A, one can estimate the amount of time a surface will remain relatively free of contamination. For example, a sample at 300 K in an environment containing CO gas will have an impingement rate of 2.87×10^{10} cm^{-2} s^{-1} at a pressure of 10^{-10} mbar. A single monolayer of adsorbed gas molecules is typically defined as ~10^{15} molecules per cm^2. Considering a 1 cm^2 sample in a UHV chamber at 10^{-10} mbar, assuming a unit sticking probability, one would expect the entire sample surface to be covered by a monolayer of gas molecules within <10 hours. Many surface science techniques have been developed to operate at pressures in this range, and in such a timeframe it is possible to perform detailed surface analysis of a sample. Whilst maintaining UHV

conditions minimises sample contamination, it is worth pointing out that this also removes the sample from a real-world environment. Because of this, UHV based studies are often used to gain insight into the fundamental properties of a system.

Typically, adsorbates do not arrange on surfaces in continuous single monolayer structures, instead localised clusters or 'islands' often form. For this reason, in UHV surface science investigations, adsorbate coverages are typically expressed in terms of monolayer equivalents (MLE). 1 MLE is defined as the number of atoms/molecules required to completely cover a sample's surface with a single monolayer of adsorbates. This provides a useful quantification for the number density of adsorbates on a surface regardless of structure. 1 MLE is ~10^{15} adsorbates per cm^2 but varies depending on the exact surface/adsorbates in question.

3.1.1 | Sample Preparation

When probing surfaces under UHV conditions, sample cleanliness and crystallographic ordering can be critical factors for collecting reliable data. The most widely used method of sample preparation in a UHV system is by successive cycles of inert ion bombardment followed by sample annealing[2].

Inert ion bombardment, or sputtering, is performed to remove any surface contaminants from a sample. To do this, inert gas (typically argon) is fed into an ion gun where it is ionised (Ar^+) by a hot filament. The resulting plasma is focused into a beam and accelerated towards the sample using electrostatic lenses, typically with a kinetic energy in the range of 500-1500 eV. The kinetic energy of the Ar^+ ions incident on the sample is transferred to the atoms of its surface causing them to be ejected into the vacuum.

After the first few atomic layers have been removed, the newly exposed surface is left very rough by the sputtering process. To re-order the surface into a smooth crystal lattice the sample is heated in a process called annealing. At high

temperatures, the atoms on a sample surface diffuse laterally. As the sample begins to cool diffusing atoms become trapped in a low energy configuration and the surface order is restored. Some complications can arise during the annealing process. If the annealing temperature is not well controlled, polymorphism can convert a thermodynamically less stable configuration into a more stable one, *e.g.* the conversion of anatase TiO_2 to rutile TiO_2. Also, repeated annealing cycles have been known to facilitate the diffusion of impurities from the bulk to the surface of a crystal. Sample heating in UHV is usually achieved by applying a high voltage to the sample and a current to a filament close to but electrically isolated from the sample. Electrons emitted by the hot filament are accelerated towards the back of the sample (to avoid damage to its surface). On impact, some of the kinetic energy of the electrons is transferred to the sample causing it to heat up. This set-up is typically referred to as an electron beam, or e-beam, heater.

3.2 | STM

During STM the motions of the tip in the z-direction (perpendicular to the sample surface) are controlled by a piezoelectric crystal to which it is attached. STM can be operated in one of two modes; constant current (CC) and constant height (CH) mode[3]. During imaging, the tip of the STM is rastered across the sample at a given separation distance d_t. As the tip encounters changes in the geometry or LDOS of the sample's surface d_t will vary accordingly. In CC mode, a feedback loop is applied that maintains a constant value of I_t by controlling the voltage applied to the tip's piezo, see Fig. 3.1. By controlling this voltage, the vertical position of the tip is varied in response to changes in I_t. Vertical movements of the tip are recorded line by line for each x and y point in a given area. From this information, a map of the scanned surface is plotted (*i.e.* a topographic STM image).

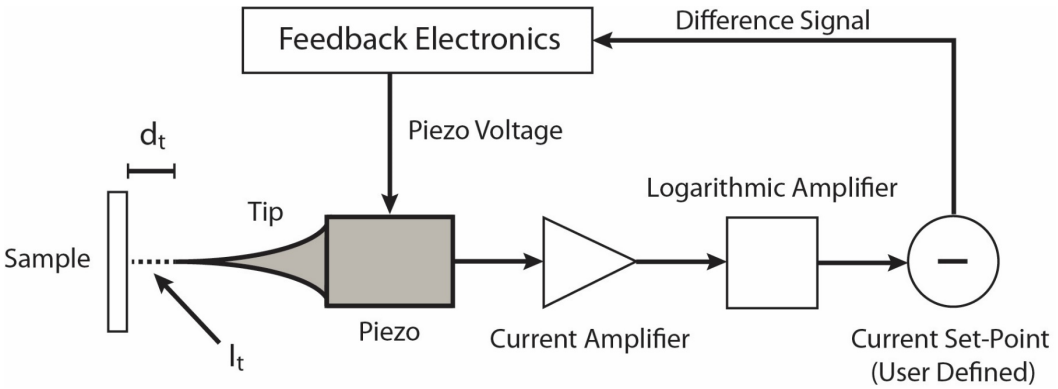

Fig. 3.1, block diagram illustrating the feedback loop mechanism used to control an STM tip while scanning in constant current mode.

In CH mode, the vertical position of the tip is held constant as it is rastered across an area. Rather than measuring tip displacement, CH STM records changes in I_t as the tip moves over the surface for each x and y point in an area. The resulting STM images correspond to the surface's LDOS only (*i.e.* an STM current map). In

comparison to CC mode, CH mode requires a very flat surface and a relatively slow scanning speed to avoid the tip crashing into the surface during scanning. In this work, all STM images were collected in CC mode.

Vibrational noise is one of the most important experimental considerations of STM analysis. To prevent noise induced motion of the tip during scanning, an eddy current damping system is incorporated into the STM tip stage[4]. The tip stage is suspended by three vertical springs with a series of copper fins around its periphery. While scanning, the tip stage is lowered such that it is supported only by the springs and is mechanically isolated from the rest of the chamber. Fixed permanent magnets are positioned around the perimeter of the tip stage between, but not in contact with, each of the copper fins, see Fig. 3.2. In combination with the rubberised feet of the STM itself, this damping system provides excellent noise isolation during operation.

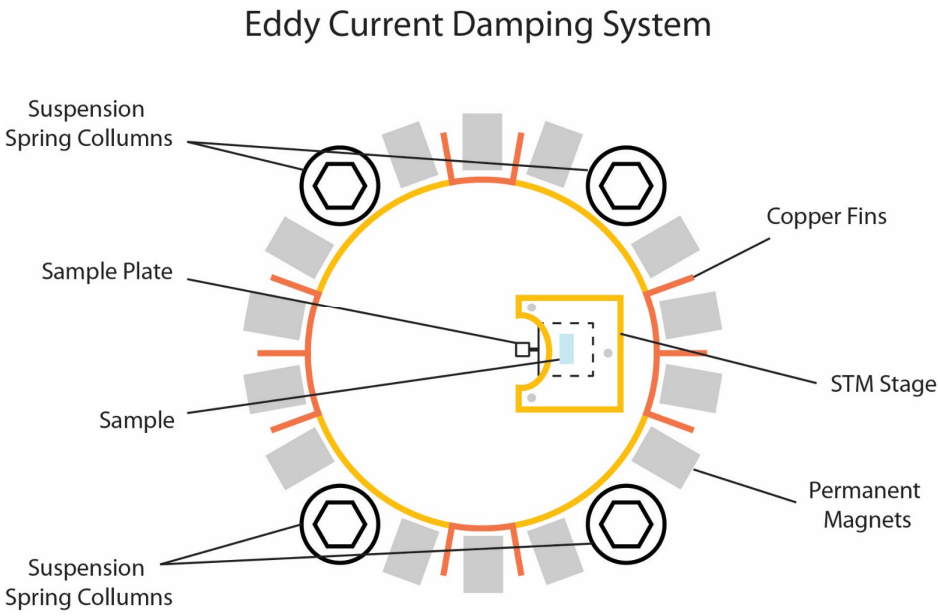

Fig. 3.2, illustration showing the eddy current damping and spring suspension system implemented in the LT-STM and VT-STM (Omicron GmbH) instruments.

In the work presented here, two different STM systems were used to collect images, a low temperature STM (LT-STM) and a variable temperature STM (VT-STM).

3.2.1 | LT-STM System

Low temperature STM measurements were carried out using a commercial Omicron *GmbH* LT-STM system. The LT-STM consists of two stainless steel chambers, a sample preparation chamber and an STM analysis chamber, separated by a single gate valve, see Fig. 3.3. STM images lack chemical sensitivity, therefore, a well maintained UHV environment is vital for accurate surface analysis. By separating analysis and sample preparation, contamination of the analysis chamber is minimised, thereby maximising the available timescale of the experiment.

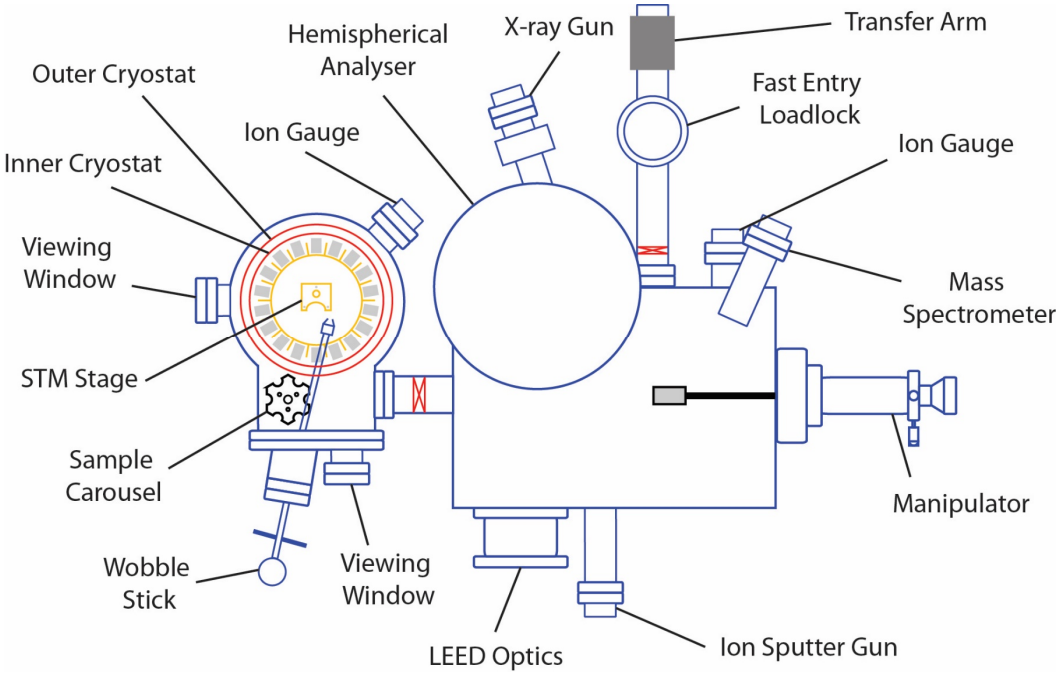

Fig. 3.3, schematic diagram of the Omicron LT-STM system used in this work. In addition to the microscope, a second UHV 'preparation' chamber is attached to the system, with an array of auxiliary analytical equipment and a fast entry load-lock.

A sample manipulator is attached to the preparation chamber of the LT-STM and is used for sample preparation and transport between both chambers. An electron bombardment heater is attached to the sample holder of the manipulator, which can be used to heat the sample, as described in the sample preparation section of this chapter. The preparation chamber incorporates an ion sputter gun (fed by high purity Ar gas), LEED optics, a

quadrupole mass spectrometer and an ion gauge, used for monitoring chamber pressure in the UHV range. In addition, a dual anode Al/Mg X-ray gun (VSW Atomtech Ltd) and a concentric hemispherical analyser are attached to the preparation chamber facilitating XPS analysis. A load-lock is connected to the preparation chamber via a UHV gate valve. Through this, samples and STM tips can be introduced into the system without the need to re-pressurise the preparation chamber. The load-lock consists of a rotary backed turbomolecular pump, a magnetic arm for sample transfers and a fast entry window.

The analysis chamber houses the LT-STM itself, which is typically operated at temperatures between 5 and 300 K. The STM stage incorporates a high precision sample heater and a bath cryostat. Combining simultaneous cooling and heating (counter heating) of the sample with robust thermal shielding, and the UHV environment, allows for excellent thermal stability while scanning. The bath cryostat consists of a two-stage system. An inner bath contacts directly with the STM stage and can be filled with either LN_2 or LHe to cool the sample directly. An outer bath of LN_2 surrounds the inner bath providing thermal insulation. A rotating carousel sample holder is attached to the inside of the analysis chamber, which can store up-to 6 samples/STM tips. As with the preparation chamber, an ion gauge is attached to monitor pressure of the analysis chamber in the UHV range.

3.2.1.1 | Au Manipulation

To induce movement of Au atoms over the TiO_2 surface, voltage pulses were applied via the STM tip. First an area of the sample was imaged at high resolution, and single Au atoms were identified. Second, the STM tip was centred above one Au atom. The tip/sample bias voltage was then ramped, while the feedback loop maintained the height of the tip above the surface. Each pulse was applied for a fixed amount of time. During the pulse, movement of the Au atom will cause a sharp drop in tunnelling current before the feedback loop can

compensate. By measuring tunnelling current as a function of time this negative spike in tunnelling current could be seen, and therefore, the time of displacement could be determined for each pulse. Movement of the Au atoms was then confirmed by recording a second topographic image of the same area.

3.2.2 | VT-STM System

Room temperature STM measurements were carried out using a commercial Omicron *GmbH* VT-STM system. As with the LT-STM, the VT-STM consists of a two-chamber system, one used for sample preparation chamber and the other for analysis, see Fig. 3.4.

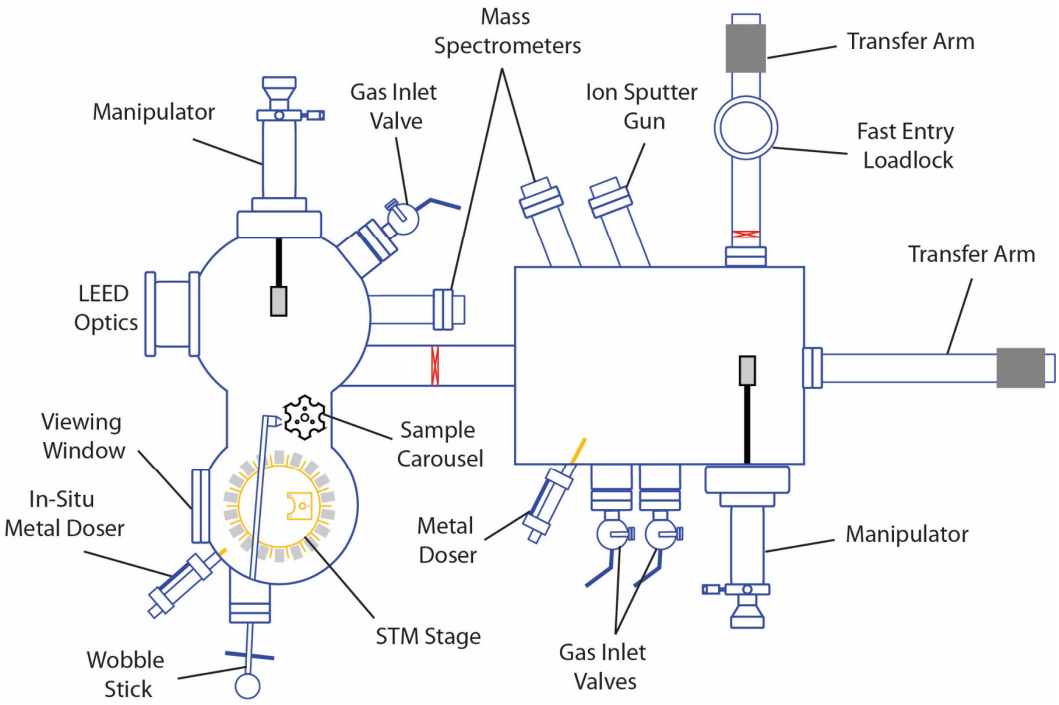

Fig. 3.4, schematic diagram of the Omicron VT-STM system used in this work. In addition to the microscope, a second UHV 'preparation' chamber is attached to the system, with an array of auxiliary analytical equipment and a fast entry load-lock.

A sample manipulator, with incorporated electron bombardment heater, is housed in the preparation chamber of the VT-STM. Unlike the LT-STM, the VT-STM's manipulator does not facilitate sample transfer between the two chambers, for which a magnetic transfer arm is used instead. Additionally, an ion

sputter gun (fed by high purity Ar gas), a quadrupole mass spectrometer, an electron beam metal evaporator, an ion gauge and two UHV gas inlet valves are attached to the preparation chamber. A load-lock is also connected in the same configuration as with the LT-STM.

The analysis chamber houses the VT-STM, which can operate at temperatures in the range of 80 to 1500 K. Sample cooling is achieved by circulating LN_2 through a loop in thermal contact with the STM stage. An in-situ metal evaporator is positioned pointing towards the STM stage such that metal can be deposited onto a sample while the STM is in operation. In addition, LEED optics (capable of both LEED and Auger), a second sample manipulator (with electron beam heater), a quadrupole mass spectrometer, an ion gauge and a sample carousel (capable of holding up to 6 samples/STM tips) are attached to the analysis chamber.

3.2.3 | Tip Fabrication

From theory, an atomically sharp, well defined tip is required to obtain the maximum resolution with STM[5]. All STM data presented in this work were collected using electrochemically etched W tips. Tips were fabricated in-house using one of two methods. In both methods W wire is used as an electrode and 2M NaOH as an electrolyte. In the 'dip method', Fig. 3.5 left, a length of W wire is submerged in NaOH solution. Due to capillary action, the surface of the NaOH solution rises around the W wire. A metal ring sitting at the surface of the solution acts as a counter electrode. As current is applied, the surface of the submerged W wire is etched, and the wire close to the surface becomes thinner. At a critical point, the W can no longer support the weight of the wire below causing it to be stretched beyond its elastic limit into a narrow tube, which eventually fractures. As the wire breaks, so too is the circuit stopping the etching process and leaving a sharp tip suitable for STM. The 'ring method', Fig. 3.5 right, involves a similar process to the dip method. Rather than submerging it, the W intersects a thin

meniscus of NaOH solution stretched across a hole in the counter electrode. Again, the tip is etched by application of a current to the circuit. As the tip breaks so too does its contact with the meniscus, opening the circuit and leaving behind a sharp W tip.

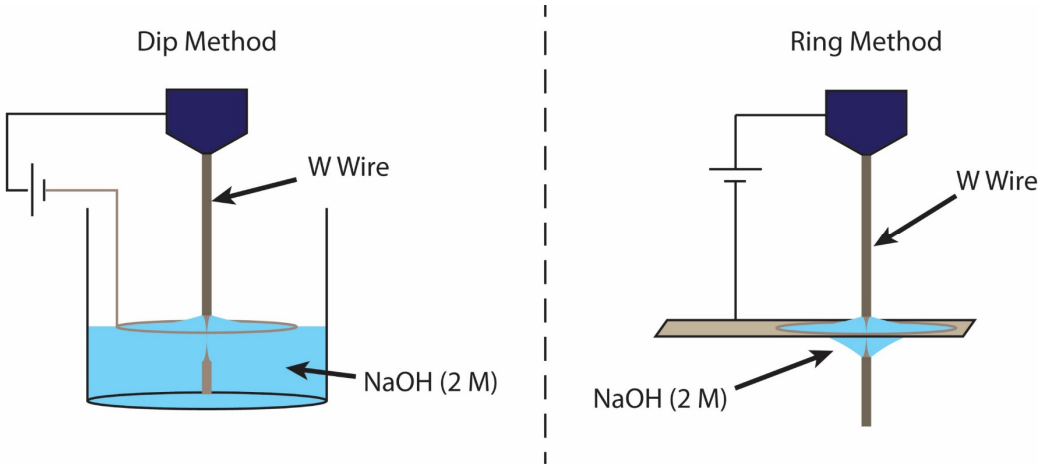

Fig. 3.5, illustration showing the two methods of STM tip preparation used in this work.

3.3 | HREELS System

HREELS experiments presented in this work were performed using a commercial VSW EELS instrument. The HREELS system, see Fig. 3.6, is comprised of an electron monochromator and analyser, contained in a stainless steel UHV chamber. A sample manipulator, with an inbuilt electron bombardment heater, and a Varian three grid front-view LEED unit are also integrated into the design of the system. Additional facilities include a Bayard Alpert ion gauge, an ion sputter gun, an Ar gas leak valve, a quadrupole mass spectrometer and an organic dosing line. The organic dosing line consisted of a rotary pumped glass vial, in which organic materials are placed, connected to the chamber via a UHV leak valve. Sample introduction is done via a fast entry load-lock of the same configuration as for the LT-STM and VT-STM systems. A combination of a rotary backed turbomolecular pump and a titanium sublimation pump are used to achieve and maintain UHV pressures in the range of 10^{-10} mbar.

External magnetic fields are known to interfere with the trajectory of scattered electrons during HREELS measurements, reducing both resolution and signal-to-noise ratio. To record an optimum energy loss spectrum, it is necessary to shield the internal components of the system from external influences such as the earth's magnetic field. An outer mu-metal case lines the inner walls of the UHV chamber and an inner cylindrical mu-metal shield encloses the HREELS monochromator and analyser, providing sufficient magnetic shielding. Further to this, only non-magnetic components are used in the construction of the sample manipulator.

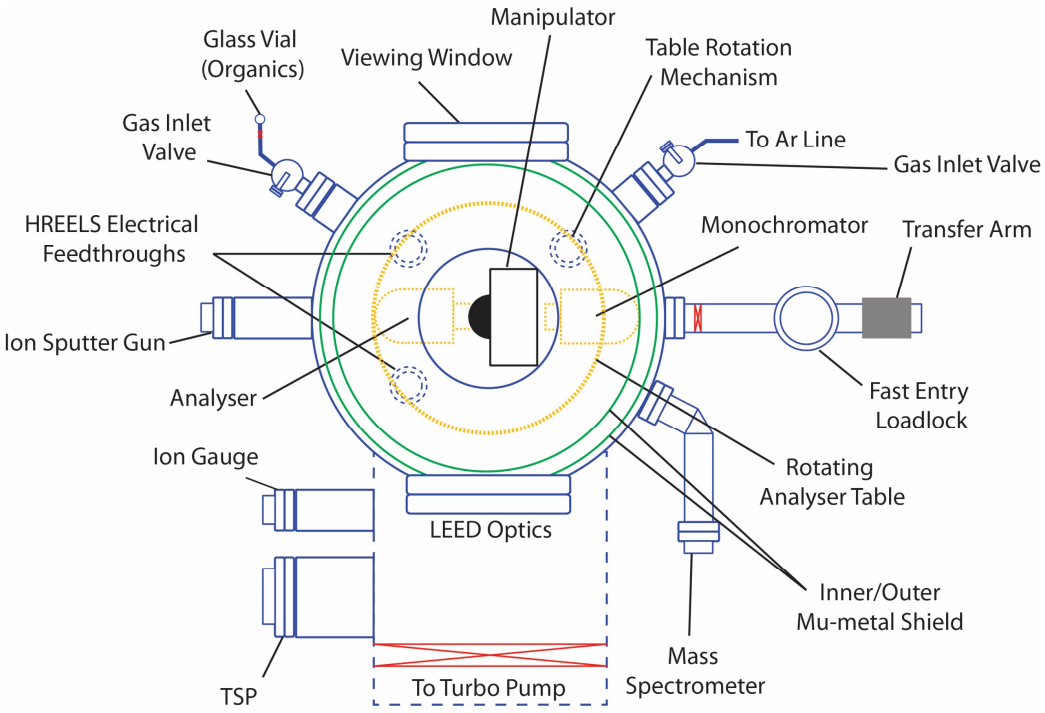

Fig. 3.6, schematic diagram of the VSW EELS system used in this work. The system is comprised of a single UHV chamber to which all necessary analytical instrumentation is attached, and a fast entry load-lock.

3.3.1 | Monochromator

The HREELS monochromator, Fig. 3.7, is used to generate a well-focused, highly monochromatic beam of electrons that can be directed at, and subsequently scattered from a sample surface. The monochromator mainly consists of three components, an electron source (tungsten filament), a hemispherical resolving section, consisting of two concentric hemispheres with a common centre, and an electrostatic lens system. Passing current through the filament generates a Maxwellian thermal distribution of electrons. The electrons are accelerated by an anode and then passed through a focusing lens to the entrance of the hemispherical resolving section. The hemispherical filter is used to select a narrow energy bandwidth at the centre of the Maxwellian distribution. The now monochromatic electrons are accelerated/decelerated to the required kinetic energy. They are then focused onto the sample by a series of electrostatic lenses on the exit aperture of the hemispherical resolving section. The pass

energy of the monochromator is controlled by the monochromator control unit with a range of 0-50 eV.

3.3.2 |HA 50 Analyser

The HREELS HA 50 analyser, Fig. 3.7, is similar in design to the monochromator, only in place of the electron source there is an electron detector. Unlike the monochromator, the analyser is mounted on a rotatable goniometer table that, in conjunction with the rotation of the sample manipulator, allows for off-specular HREELS analysis. A four element input lens covers the entrance of the analyser, specifically designed to match the exit lens of the monochromator. Incoming electrons scattered from the sample are focused by the lens system into the 1 mm channel between the two hemispheres of the resolving section, while accelerating/decelerating the electrons to a constant pass energy. Exit and entrance slits sit at both ends of the 1 mm channel. These slits help to reduce any effects of mechanical misalignment between the sample, resolving section and electron detector. The electron detector used is a channel electron multiplier (CEM). During operation, a potential of 1.9 keV was applied to the rear of the CEM (approximately 10 times that applied to the front). When an electron strikes the CEM, the resulting potential gradient, together with its high secondary electron emissivity, results is a cascade of electrons. A gain of approximately 10^8 is achieved via this process creating a ‘current pulse’ for each electron striking the front of the CEM. A preamplifier converts this into a voltage pulse signal, which is then fed to a computer for analysis.

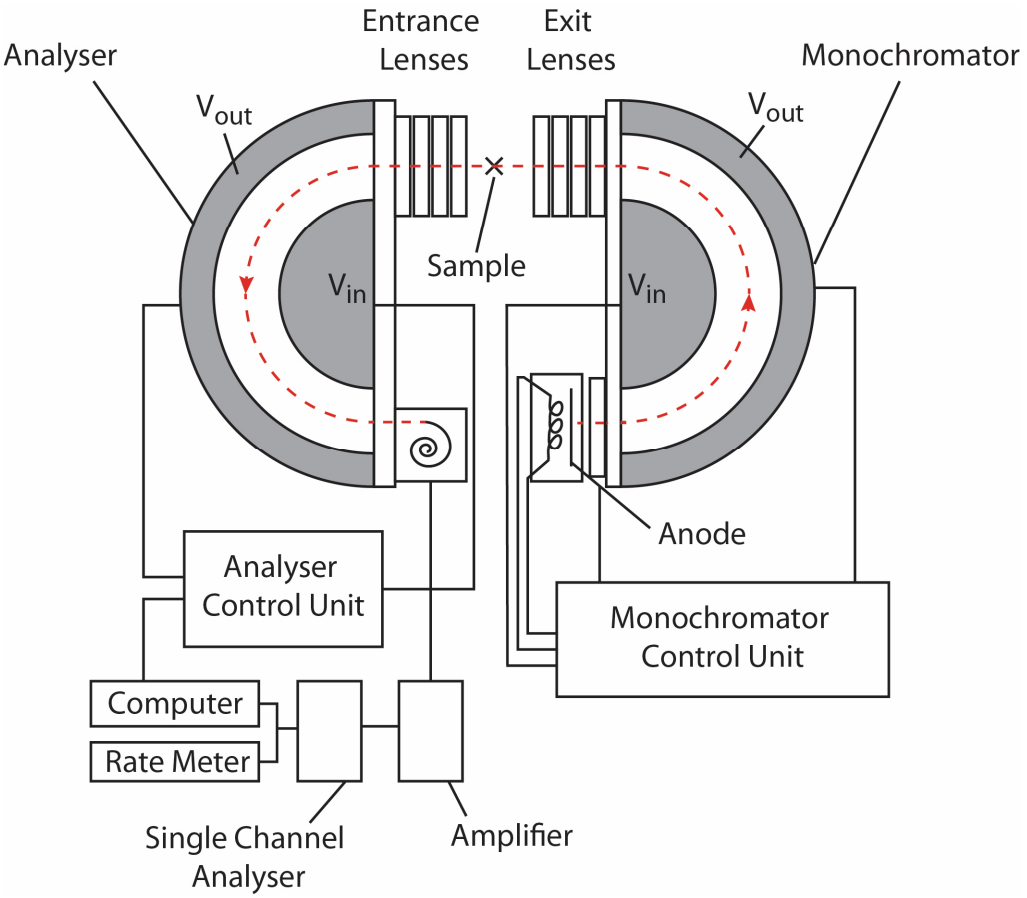

Fig. 3.7 diagram showing the physical design and electronic connections of the monochromator and HA 50 analyser used to perform HREELS in this work.

The instrumental resolution achieved during HREELS is determined by a combination of the monochromator and analyser pass energies. Typically, an analyser pass energy of 1 eV, and a monochromator pass energy of 1.35 eV were used to collect the data presented in this work. The resulting energy resolution (full width at half maximum) was measured from the elastic peak to be approximately 10 meV from a clean rutile TiO_2 sample. This resolution degraded following deposition of organic material onto the rutile surface.

3.3.3 | Fourier Deconvolution Macro

To perform vibrational analysis of TiO_2 it is necessary to remove the intense multiple phonon loss features that appear in HREEL spectra. To perform

the necessary Fourier deconvolution, as detailed in chapter 2, a procedure was adapted from the work of Thomas for the Igor Pro 6 software package (WaveMetrics)[6]. The procedure used is given in the appendix section, with a detailed description of each individual macro.

3.4 | LEED and AES

LEED data presented in this work was collected using a Varian front-view LEED system. This system consists of a four-grid optics unit and integrated electron gun attached to the HREELS UHV chamber. A schematic diagram of the LEED optics is shown in Fig. 3.8 a). The optics consist of a series of hemispherical components with a common focal point, typically the position of the sample. The outermost hemisphere of the system is a fluorescent screen, used to detect electrons scattered from a sample and visualise the resulting diffraction pattern. LEED data is recorded by photographing the fluorescent screen during measurements. The inner and outermost grids of the optics are grounded to provide a field free region between the sample and the fluorescent screen. The middle (retarding) grids are biased at a value just below the currently set beam voltage. This decelerates scattered electrons filtering out (or retarding) any lower energy electrons generated by inelastic scattering events. The filtered, elastically scattered, electrons are then reaccelerated towards the screen, which is held at a potential of 5 kV. The electron gun is positioned at the centre of the optics, such that a monochromatic beam of electrons can be directed through the focal point of the optics. Typically, an electron beam of ~50 μA is used, with energy in the range of 20-300 eV. The beam energy (voltage) and retarding field potential are set by a single electronic control unit that keeps the two values at a fixed potential separation. The control unit also outputs the applied 5 kV to the fluorescent screen and controls the focusing and beam current of the electron gun.

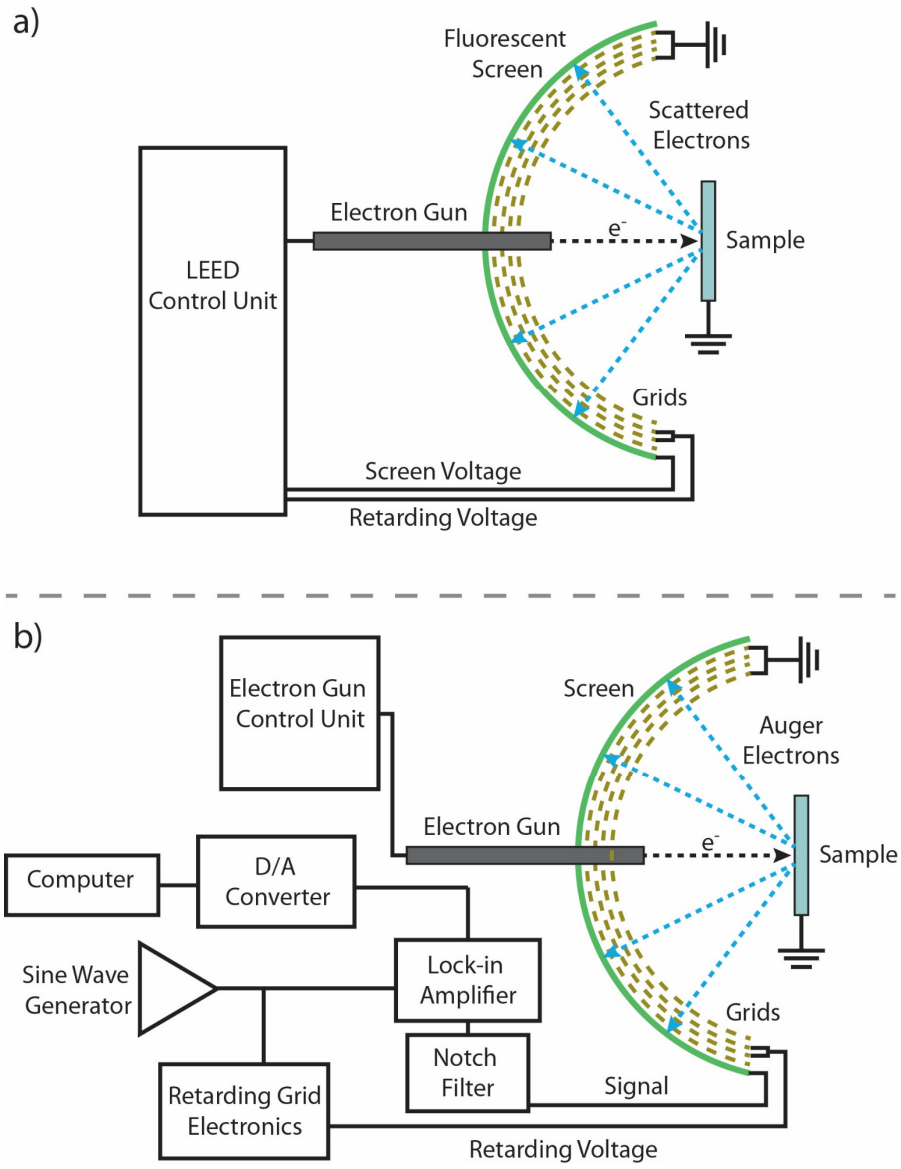

Fig. 3.8, diagram illustrating the instrumental and electronic configuration of the Varian LEED optics used in this work for both LEED, a), and Auger, b), modes.

AES data presented in this work was collected using the same Varian optics used for LEED measurements, as described above. To collect AES spectra, the LEED optics were re-configured as per Fig. 3.8 b). In AES mode, the voltage of the retarding grid is no longer linked to the electron beam energy, but rather a constant beam energy of ~800-3000 V is used. A modulation, produced by a sinewave generator, is applied to the retarding grids. The accelerating potential of the screen is set to +300 V relative to the sample. Rather than inducing and measuring fluorescence, in AES mode a current is measured from the screen

corresponding to the total electron flux hitting it at the set retarding potential. The signal from the screen is fed via a notch filter (through which the +300 V screen bias is applied) to a lock-in amplifier. Once amplified by the lock-in the differentiated signal is fed to a computer, via a digital/analogue converter. Software on the computer records the detected electron intensity as a function of retarding potential. By sweeping the retarding potential through an energy range, an AES spectrum of the sample is recorded on the computer.

3.5 | Diamond IO6

The experiments presented in chapter 5 of this work were performed at the UK synchrotron facility 'Diamond Light Source' on the nanoscience beamline, IO6. The facilities at IO6 utilise variable circular and linearly polarised soft X-rays, produced by the synchrotron, to probe the surfaces of materials in the nanoscale regime. The X-ray beam energy may be selected within the range of 80-2100 eV[7]. The data shown in chapter 5 were recorded using a constant beam energy of 200 eV for all measurements. In the beamline configuration, two APPLE II undulators give access to both left and right circularly polarised photons as well as s or p linearly polarised photons. Following the undulators, a series of mirrors focus the beam into a monochromator. The resolving power of the collimated light plane grating monochromator (ΔE/E) is 10,000 at 400 eV and produces a beam with a spot size of 30 μm^2. After passing through the monochromator, the beam is diverted using two toroidal mirrors to either the PEEM or the branch exit slits. A Kirkpatrick-Baez refocussing mirror is used for the PEEM instrument, while a toroidal refocussing mirror is employed for the branchline. The PEEM end station of the IO6 beamline is comprised of a dedicated PEEM UHV chamber, housing an Elmitec LEEM III instrument. Additionally, a surface analysis chamber adjoining the PEEM chamber provides facilities for AES, LEED, sample preparation, metal vapour deposition (Omicron EFM III) and variable temperature STM (Omicron VT-STM). The Omicron VT-STM of the PEEM end station is of the same design and configuration as the VT-STM detailed above.

3.5.1 | XPEEM and LEEM

In addition to XPEEM analysis, the inclusion of a high stability electron gun and UV illumination source allow for LEEM and UV-PEEM to be performed using the Elmitec III apparatus. As such, the instrument is commonly known as a

spectroscopic photoemission and low energy electron microscope (SPELEEM). Using soft X-rays produced by the synchrotron, XPEEM can resolve features as small as 50 nm in diameter.

A schematic diagram of the PEEM instrument is shown in Fig. 3.9 for four different configurations; μ-XPS, XAS/LEEM, energy filtered imaging and LEED mode[8]. In the most basic configuration of the instrument, X-rays or electrons (generated by the electron gun and focused via an illumination column) are directed towards the sample through the objective lens. Excitation of the surface by the incident beam causes electrons to be emitted from the sample and pass back through the objective lens to the imaging column (via a beam splitter). The imaging column consists of a series of lenses (transfer, field, and intermediate) that magnify the image of the beam onto the first projective lens. The beam then passes through an energy analyser, which filters the energy of the beam via two retarding lenses. The electrons are then accelerated in the analyser by two accelerating lenses. On leaving the analyser the electrons are further energy filtered by the presence of an exit slit. Finally, second and third projecting lenses focus the beam onto a 2D electron detector, which then records the subsequent PEEM image.

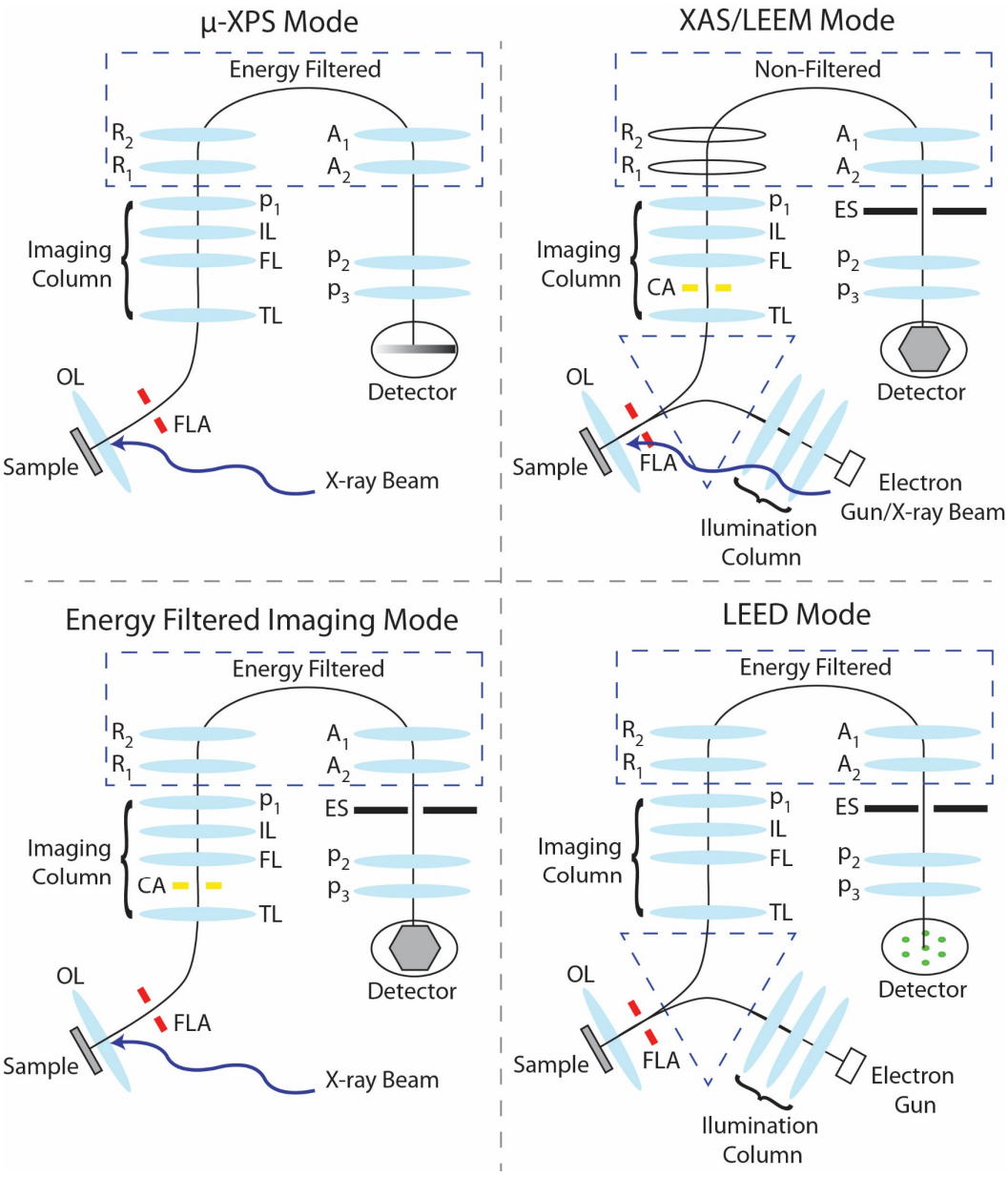

Fig. 3.9, diagram showing the instrumental setup of the Elmitec III LEEM on the IO6 beamline at Diamond Light Source UK. Configurations for four different modes of operation, μ-XPS, XAS/LEEM, energy filtered imaging and LEED, are shown. OL - objective lens. R - retarding lenses. A - accelerating lenses. P - projecting lenses. IL - illumination lens. FL – field lens. TL - transfer lens. FLA - Field limiting aperture. CA - contrast aperture. ES - exit slits. Adapted from Locatelli[8].

In μ-XPS mode, a field-limiting aperture is inserted prior to the objective lens that restricts the probed area (down to 2 μm). The intermediate and first projective lenses are used to magnify the objective image of the sample. In this configuration, the exit slit is removed to allow the full dispersive plane of the analyser to pass through. The final two projective lenses project the dispersive

plane of the analyser onto the detector. A core level energy spectrum can be generated by taking a line profile from the image recorded on the detector comparable to that recorded by conventional XPS.

In XPEEM/LEEM mode a field-limiting aperture may or may not be used as is needed. In addition, a contrast aperture is inserted into the imaging column between the transfer and field lenses. The purpose of the contrast aperture is to restrict the angular acceptance of electrons passing through, thereby creating structure related contrast in subsequent images. In XPEEM/LEEM mode, the retarding lenses of the analyser are not active and a variable beam energy is used instead.

LEED mode operates in a similar way as the XPEEM/LEEM mode, however the contrast limiting aperture is not inserted. This results in the projection of a surface diffraction pattern onto the detector, rather than an image of the surface.

3.5.1.1 | Data Processing

μ-XPS spectra collected at IO6 were analysed using a custom written procedure of the Igor Pro software package, provided by Diamond Light Source. For all spectra shown in chapter 5, binding energy scales were calibrated using the position of the Ti 3p peak which is well defined in the literature, appearing centred at 38 eV[9]. This calibration point was confirmed by the correct alignment of TiO_2's band gap state, known to be at ~0.8 eV and the Fermi level (0 eV)[10].

A flat field image was recorded and subsequently subtracted from all μ-XPS data prior to analysis. This had the effect of removing any fixed pattern noise caused by imperfections in the electron detector itself. In addition to subtracting a flat field image, background spectra were recorded for all measurements at points in the spectrum close to the energies of interest, but where no features appear. Subtracting these measurements from the appropriate data set effectively removed any remaining noise present in the recorded spectra.

Prior to this, a linear baseline was subtracted from each background and data spectrum to correct any differences in gradient caused by the non-linear background of low energy electrons, see Fig. 3.10. All peak fitting was performed using the Igor Pro Multi-Peak Fit 2.0 package following background subtraction.

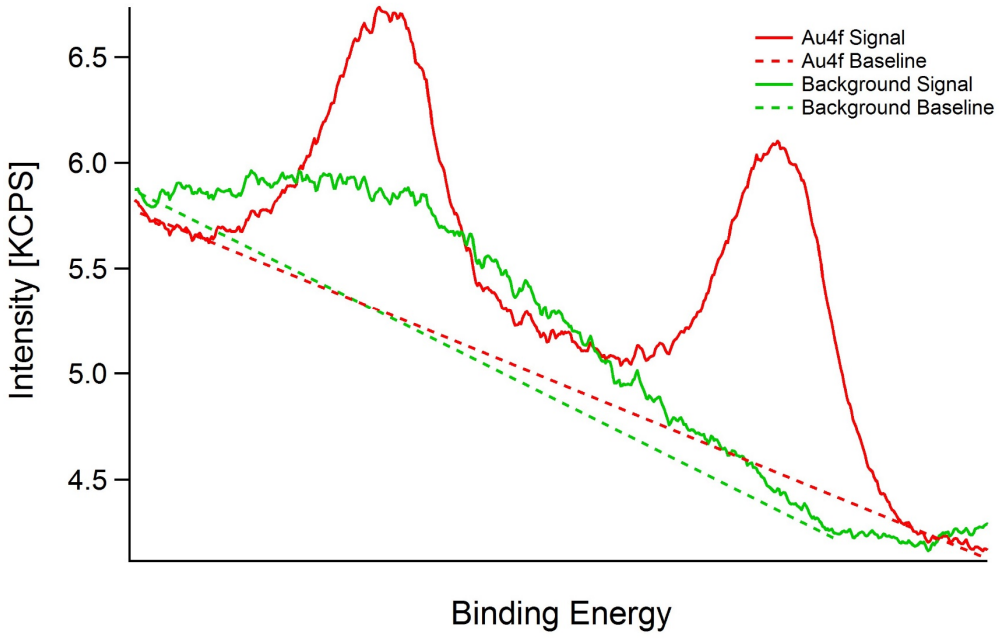

Fig. 3.10, Au 4f (red) and background (green) XPEEM spectra collected from an Au/TiO_2 sample. Baseline correction was used to remove any gradient differences caused by variations in the background of low energy electrons at different energies in the spectrum. Dashed lines indicate the linear baseline subtracted from each spectrum. The background spectrum shown was collected between 80.2 and 72.5 eV. The Au 4f spectrum was collected between 90.2 and 85.5 eV.

3.5.2 | EFM III In-situ Metal Evaporator

During sample preparation at IO6, Au was vapour deposited onto rutile TiO_2 samples via an Omicron EFM III in-situ doser connected to the VT-STM of the surface analysis chamber. A diagram of the EFM III doser is shown in Fig. 3.11. During operation, the Mo crucible is positively biased relative to a grounded thoriated tungsten filament. By applying a current to the filament, electrons are emitted and subsequently accelerated towards the crucible causing it to heat up via electron bombardment. As its temperature rises, the metal sample within the

crucible, inserted before attaching the doser to the chamber, will begin to vaporise. The subsequent vapour is filtered into a beam and directed towards a sample. A water cooling system is connected to the crucible, and a flux monitor can be used to precisely control the rate of sample deposition.

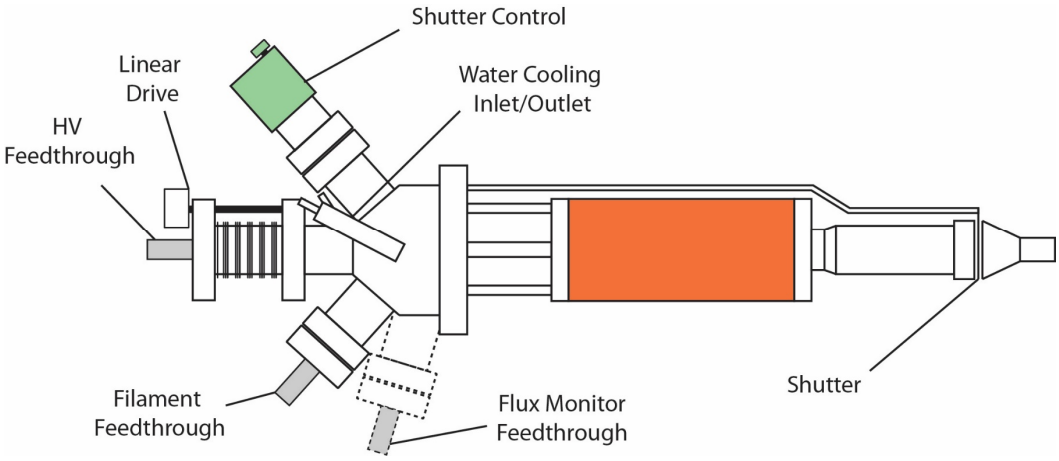

Fig. 3.11, illustration of the Omicron EFM III metal evaporator used at IO6 (Diamond Light Source, UK) for Au nanoparticle deposition.

3.6 | References

1. Kolasinski, K. W. in *Surface Science* 185–228 (John Wiley & Sons, Ltd, 2012).
2. Attard, G. & Barnes, C. *Surfaces*. (Oxford University Press, 1998).
3. Binnig, G. & Smith, D. P. E. Single tube three dimensional scanner for scanning tunneling microscopy. *Rev. Sci. Instrum.* **57,** 1688–1689 (1986).
4. Omicron GmbH. *The Low Temperature STM User's Guide*. (Omicron GmbH, 2002).
5. Melmed, A. J. The art and science and other aspects of making sharp tips. *J. Vac. Sci. Technol. B Microelectron. Nanom. Struct. Process. Meas. Phenom.* **9,** 601–608 (1991).
6. Thomas, A. G. Adsorbate Studies of Titanuim Oxides. (University of Liverpool, 1994).
7. Dhesi, S. S. *et al.* The nanoscience beamline (I06) at diamond light source. in *AIP Conference Proceedings* 311–314 (2010).
8. Locatelli, A. Basic concepts for LEEM and XPEEM and applications. (2012). Available at: http://indico.ictp.it/event/a11156/session/51/contribution/31/material/0/0.pdf. (Accessed: 18th January 2017)
9. Espinos, J. P. *et al.* Synchrotron photoemission characterization of TiO_2 supported on SiO_2. *Langmuir* **14,** 4908–4914 (1998).
10. Yim, C. M., Pang, C. L. & Thornton, G. Oxygen vacancy origin of the surface band-gap state of TiO_2(110). *Phys. Rev. Lett.* **104,** 36806 (2010).

Chapter 4

Gold atoms occupy oxygen vacancy sites on TiO_2(110)

Outline

Au nanoparticle based systems exhibit significantly enhanced catalytic activity compared to bulk gold analogues. In particular, highly dispersed Au nanoparticles supported by reducible metal oxide surfaces are known to be active catalysts for a number of reactions including CO oxidation and hydrogen production. Interestingly, the observed trend of increasing activity as Au particle size decreases cannot be accounted for by an increased number of surface active sites alone. The exact choice of metal oxide support has been shown to have a marked impact on activity, suggesting that interactions between Au and the support play a key role in catalysis. In this study, STM (Scanning Tunnelling Microscopy) was used to explore the characteristics of Au/TiO_2, a low

temperature oxidation catalyst and a potential catalyst for the water gas shift reaction (WGS). Using in-situ deposition, the nucleation site for single Au atoms has been identified as surface oxygen vacancies on a reduced TiO_2 substrate. Further to this, a reproducible method for atomic manipulation has been developed to provide further evidence for Au atom nucleation at oxygen vacancies. The manipulation technique used was analysed in more detail to provide insight into the chemical interactions between Au and the substrate.

4.1 | Introduction

The nature of the interaction between Au nanoparticles and reducible metal oxide substrates remains a key area of research in catalysis[1–10]. In particular, TiO_2 supported Au nanoparticles form an effective low temperature oxidation catalyst[11]. Mixed phase powder catalysts have proven to be highly active systems, however, single crystal substrates are still studied as model catalyst systems to aid future investigations[12–16]. Au adsorption on rutile TiO_2 (110) has received extensive study largely owing to the fact that TiO_2 is one of the most well characterised metal oxide systems to date[17–24]. It has been observed that reduction of single crystal rutile TiO_2 leads to the formation of point defects on the surface in the form of oxygen vacancies ($O_{b\text{-}vacs}$), bridging hydroxyl species (OH_b), as well as Ti interstitial atoms in the bulk. $O_{b\text{-}vacs}$ in particular are a widely studied aspect of TiO_2 catalysis as they represent reactive features on the surface and in many cases they act as bonding sites for surface adsorbates[25–28].

A key aspect of the Au/TiO_2 system that remains controversial is the nucleation properties of individual Au atoms (Au_1) on the surface. Whether Au_1 are of significance for oxidation catalysis is not known, but single atom catalysis has been demonstrated for other systems and Au_1 on TiO_2(110) has been shown

to be stable up to at least 600 K[29,30]. After soft landing Au^+, Tong *et al.* observe Au atoms bonding to bridging oxygen rows on TiO_2 using STM, assigning the adsorption site to a bridging oxygen vacancy ($O_{b\text{-}vac}$)[30]. On cooling to 300 K, they observe a reversible shift of the adsorption site to Ti rows, assigning the new position to atop a five-fold coordinated Ti site (Ti_{5c}). This was interpreted as a displacement of the Au_1 by interaction with adventitiously co-adsorbed water. This observation is in line with earlier spectroscopic work and STM measurements[31,32]. Although the STM results referenced above clearly observe Au_1 associated with bridging O rows, no direct evidence is given for bonding to $O_{b\text{-}vac}$. However, the results of several density functional theory (DFT) calculations suggest that $O_{b\text{-}vacs}$ are the preferred adsorption site for Au_1[33–36]. More recent results have challenged the $Au_1/O_{b\text{-}vac}$ assignment. In a recently published paper, aberration-corrected STEM was used to image Pt_1 on TiO_2(110). The authors conclude that Pt_1 occupies in-plane O vacancies and not $O_{b\text{-}vac}$[37]. The implication being that Au_1 will behave in a similar fashion to Pt_1. In a related system, Au/CeO_2(111), kinetic effects appear to dominate over thermodynamic stability, thereby preventing occupation of oxygen vacancies by Au_1[38].

There are many experimental and theoretical studies of Au on TiO_2(110) in the literature. One study combined experimental and computational work on Au/TiO_2 for various levels of substrate reduction. First, they identify single Au atoms (Au_1) using STM then, using DFT, they calculate their adsorption energy at different surface sites on the TiO_2[31]. Matthey *et al.*'s results, in agreement with previous computational studies, suggest Au initially adsorbs at $O_{b\text{-}vacs}$ on TiO_2 (110). Chretien and Metiu expanded on this, suggesting Au_1 forms covalent bonds with the five-fold Ti (Ti_{5c}) atoms either side of an $O_{b\text{-}vac}$[39]. A more recent study by Heyden and Ammal further supports this view, showing Au_n will covalently bond to an $O_{b\text{-}vac}$ for odd values of n[33]. This dependence on the number of Au atoms per nanoparticle is in line with Matthey's experimental results, which identify Au_1 and Au_3 on the surface but not Au_2. Using vapour deposition and STM imaging, Tong

et al. have shown Au_1 to move position on TiO_2 (110) after the adsorption, and subsequent dissociation, of H_2O molecules on the surface[30]. Before exposure to H_2O, Au_1 appears centred over O_b rows, but after exposure they appear atop Ti_{5c} rows and always in close proximity to an OH_b. Tong *et al.* conclude that Au_1 is displaced from $O_{b\text{-}vac}$ sites by the OH_b generated during water dissociation, but some ambiguity remains[18]. Water dissociation is known to produce two OH_b species for each $O_{b\text{-}vac}$, therefore, proximity to an OH_b does not guarantee that an $O_{b\text{-}vac}$ is initially present beneath the Au_1, only that Au_1 has an attractive interaction with OH_b. A recent publication by Loffreda *et al.* has revealed that the presence of OH_b species on TiO_2 stabilises Au particle adsorption. For hydrated surfaces, they observe the most stable Au configuration on stoichiometric TiO_2 is in a bridging position between Ti_{5c} and O_{2c} sites. In contrast to the work of Tong *et al.*, on reduced TiO_2 Loffreda *et al.* find the density of $O_{b\text{-}vacs}$ reduces following deposition of Au, suggesting these are the most stable Au adsorption sites. In addition, they also observe that Au atoms preferentially nucleate at TiO_x clusters over $O_{b\text{-}vacs}$[40]. TiO_x clusters are caused by reconstructions of the surface as the sample becomes more heavily reduced.

In 1980, Eigler demonstrated that the tip of an STM can be used to position single Xe atoms on a Ni (110) surface[23]. Since then many different methodologies for atomic and molecular manipulation have been developed using STM, making it possible to not only relocate individual species[41–43] but also induce dissociation, desorption and even create charged species[8,18,44]. Most methodologies employ mechanical interaction[45,46], a field effect[23], vibrational excitation[47], or electronic excitation[18,31,48] to interact with the target species.

This chapter presents direct evidence of single Au atoms (Au_1) nucleating at $O_{b\text{-}vacs}$ on a reduced rutile TiO_2 (r-TiO_2) (110) surface. By comparing STM images of the same area on the surface before and after dosing Au_1 it is possible to identify the initial nucleation site. In addition to this, a method for selectively displacing Au_1 from $O_{b\text{-}vacs}$, using voltage pulses from an STM tip (tip pulses), has been developed to provide evidence for Au_1 nucleation site. A detailed analysis of

this manipulation method, similar to those used by others in the literature[23,42,49–51], is also given. From this analysis, an underlying mechanism of Au_1 displacement is suggested, which provides an insight into the nanoparticle/substrate interaction.

4.2 | Experimental Procedure

Low temperature experiments were carried out at 78 K using an Omicron *GmbH* low-temperature scanning tunnelling microscope (LT-STM) housed in a bath cryostat in an ultrahigh vacuum (UHV) chamber with a base pressure of 3×10^{-11} mbar (See Chapter 3). The adjoining preparation chamber was equipped with an ion sputter gun, sample heater, and facilities for X-ray photoelectron spectroscopy (XPS) and low energy electron diffraction (LEED) measurements. A rutile TiO_2 (110) single crystal (MaTecK) sample was prepared by successive cycles of argon ion sputtering and annealing (in vacuum) to 1000 K. The sample cleanliness and long-range order were checked using XPS and LEED respectively. Au was deposited onto an as-prepared TiO_2 (110) surface at room temperature. The deposition source consisted of a tungsten filament wrapped around a pure Au sample. To induce sublimation, the Au sample was resistively heated by applying a current to the tungsten filament. The presence of Au on the TiO_2 substrate was confirmed using XPS with Al Kα (hν = 1486.7 eV) as a photon source. XPS spectra were collected at normal emission.

Room temperature experiments were carried out by David Humphrey. They employed an Omicron *GmbH* variable temperature scanning tunnelling microscope (VT-STM) in an ultrahigh vacuum (UHV) chamber (base pressure = 5×10^{-11} mbar). The adjoining preparation chamber is equipped with an ion sputter gun, sample heater, and facilities for Auger electron spectroscopy (AES) and low energy electron diffraction (LEED) measurements. As above, a rutile TiO_2 (110) (MaTecK) sample was prepared by successive cycles of argon ion sputtering and annealing in vacuum to 1000 K. The sample cleanliness and long-range order were checked using AES and LEED, respectively. Au was deposited onto an as-prepared TiO_2 (110) surface at room temperature. In-situ deposition was performed using a line-of-sight e-beam evaporator. The deposition source consisted of an Au sample placed in the recess of a molybdenum crucible and was

heated via electron bombardment. The subsequent molecular beam was directed onto a TiO_2 (110) sample while in the sample stage of the VT-STM. The STM tip was retracted prior to deposition. In both systems, STM micrographs were collected in constant current mode using an electrochemically etched W tip conditioned by degassing at 500 K and voltage pulsing. From the STM data no significant differences in Au coverage or dispersion were evident when scanning at either 78 K and 300 K.

4.3 | Results and Discussion

4.3.1 | Clean Rutile TiO_2 (110)

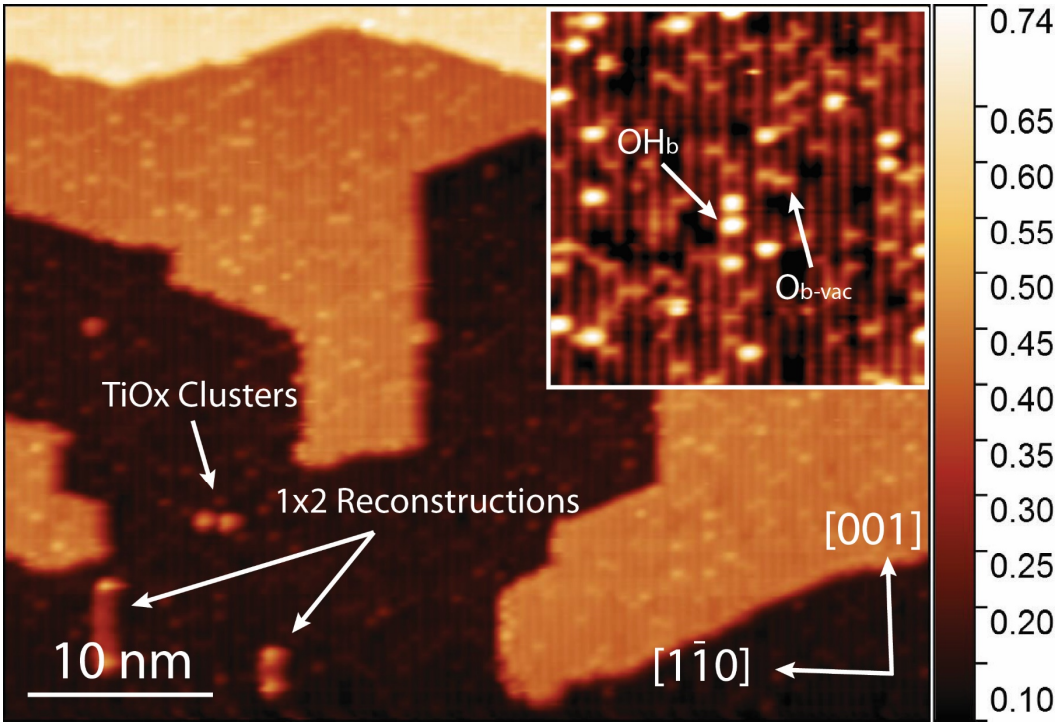

Fig. 4.1, STM image of a clean, as-prepared r-TiO_2 (110) sample. Some TiO_x clusters and 1x2 reconstructions, indicated on the image, can be seen dispersed over the clean surface. The inset shows a 10 nm^2 magnified view taken from the main image with examples of an OH_b and $O_{b\text{-}vac}$ indicated. Alternating bright and dark rows running vertically across the terraces correspond to Ti_{5c} and O_b rows, respectively. Image recorded at 78 K. The z-scale of the colour map used is given, in nm, on the right-hand side of the image. Scan parameters: V_S = +1.3 V, I_T = 50 pA.

A clean r-TiO_2 (110) single crystal surface was prepared by ion sputtering and annealing to 1000 K in UHV. Before imaging with STM, surface cleanliness and order of the sample were confirmed by XPS and LEED. Fig. 4.1 shows an STM image of an as prepared r-TiO_2 (110) surface. In the literature It is well established that rows of Ti_{5c} and O_b atoms running along the surface in the [001] appear as alternating bright and dark lines, respectively[17,18].

4.3.2 | Au nanoparticle Identification

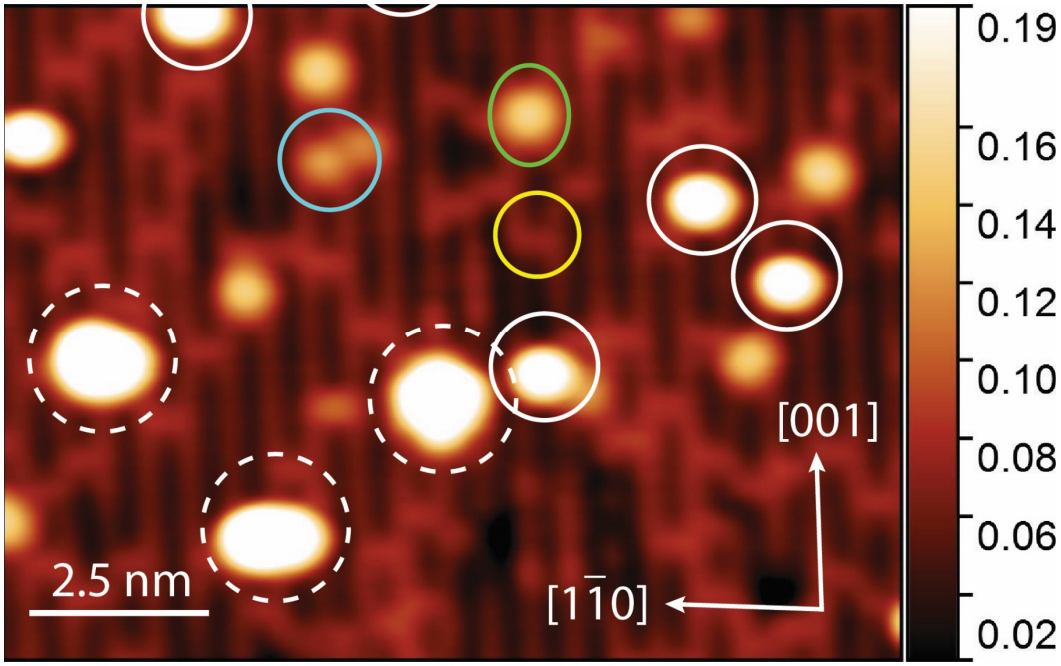

Fig.4.2, STM image of r-TiO_2 (110). Before acquisition, 0.08 ± 0.001 MLE of Au was deposited onto the surface at room temperature (where 1 MLE is equal to 1.387×10^{15} Au atoms per cm^2). An $O_{b\text{-}vac}$ has been marked by a yellow circle. Blue and yellow circles highlight single and double OH_b species, respectively. White solid and dashed lines mark Au_1 and Au_3 species respectively. The z-scale of the colour map used is given, in nm, on the right-hand side of the image. Image recorded at 78 K. Scan parameters: V_S = +1.3 V, I_T = 50 pA.

Fig.4.2 shows an STM image of the as-prepared TiO_2 (110) surface after deposition of a 0.08 MLE of Au, where 1 MLE is equal to 1.387×10^{15} Au atoms per cm^2. Four distinct types of surface feature appear evenly distributed over the surface. The two smallest features are both centred over the O_b rows on the surface. The first appears as a small horizontal line, while the second is larger and more circular. Such features are well characterised in the literature and are typically attributed to $O_{b\text{-}vacs}$ and OH_b[21,31,30,52]. Acharya *et al.* have shown that application of a +3 V tip pulse can desorb OH_b from the surface, while $O_{b\text{-}vacs}$ remain unaffected[53]. Using this method, Bikondoa et al[53] determined the first feature type to be $O_{b\text{-}vacs}$ (yellow circle) and the second OH_b (blue circles). The two remaining unidentified features are not typical of STM images from clean r-TiO_2 (110) and can be attributed to deposited Au species. The first (white solid circles, Fig.4.2) appear centred over the O_b rows on the surface with an average height of

193 ± 60 pm. The second (white dashed circles Fig.4.2) are larger, spanning multiple O_b rows in the [$\bar{1}$10] direction with an average height of 233 ± 10 pm. The larger Au species can be centred over either O_b or Ti_{5c} rows. Using STM in conjunction with density functional theory (DFT) Matthey *et al.* identified the smallest Au species present on an Au deposited r-TiO_2 (110) to be Au_1. The second smallest species they assign as Au trimers (Au_3) that may adsorb in one of two geometries either centred over O_b or Ti_{5c} rows[31]. By direct comparison of our data with Matthey *et al.*'s work the smallest Au species observed in Fig.4.2 were assigned as Au_1 and the larger ones Au_3.

4.3.3 | Nucleation of Atomic Au

Based on their observations of the Au/TiO_2 system, Matthey *et al.* suggest that Au_1 adsorbs at $O_{b\text{-}vacs}$ on r-TiO_2 (110), while on oxidized TiO_2 (110) (*o*-TiO_2) Au_1 bind to oxygen adatoms (O_{ad}) (which are themselves adsorbed at Ti_{5c} sites)[31]. Scanning transmission electron microscopy (STEM) measurements by Shibata *et al.* support Matthey *et al.*'s suggestions; however, none of the data provided give direct evidence and therefore are not conclusive[54].

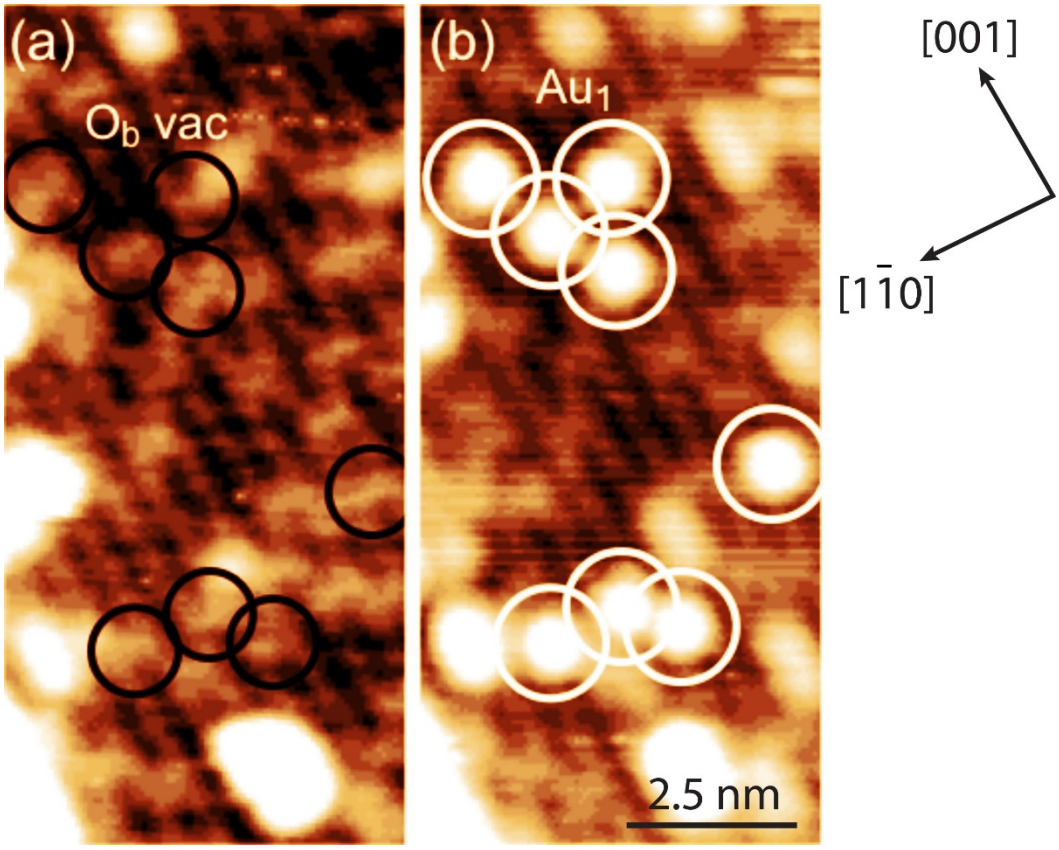

Fig.4.3, STM images of the rutile TiO_2 (110) surface before (a) and after (b) deposition of nanoparticulate Au. Circles mark the same positions in both images. Black circles in (a) can be seen to lie over $O_{b\text{-}vacs}$ while the white circles in (b) indicate Au_1. Scan parameters: V_S = +1.3 V, I_T = 20 pA. Both images were recorded at 300 K.

To conclusively identify the nucleation site of Au_1, Au has been deposited in-situ onto r-TiO_2 (110). Fig.4.3(a) shows the as-prepared surface before deposition. By applying the same methodology set out above, features on the surface were assigned as $O_{b\text{-}vac}$ and OH_b species. After collecting the image shown in Fig.4.3(a) the STM tip was retracted and Au was deposited onto the surface using an in-situ e-beam doser. The STM tip was then re-approached to the sample to the exact position it was previously, and the area in Fig.4.3(a) located and imaged a second time. After deposition, Au related features appear having the same height and appearance as those assigned to Au_1 in Fig. 4.2. They are identified by white solid lines in Fig. 4.3(b). Using STM images of the same area on the surface, taken before (Fig.4.3(a)) and after (Fig.4.3(b)) deposition, the exact sites at which Au_1 adsorb can be directly identified. The positions at which Au_1 adsorb have been highlighted in Fig.4.3(a) as solid black circles. By comparing

Fig.4.3(a) and (b) it is clear, following deposition, Au_1 nucleate at sites on the surface previously occupied by $O_{b\text{-}vacs}$.

4.3.4 | Manipulation of Atomic Au via STM

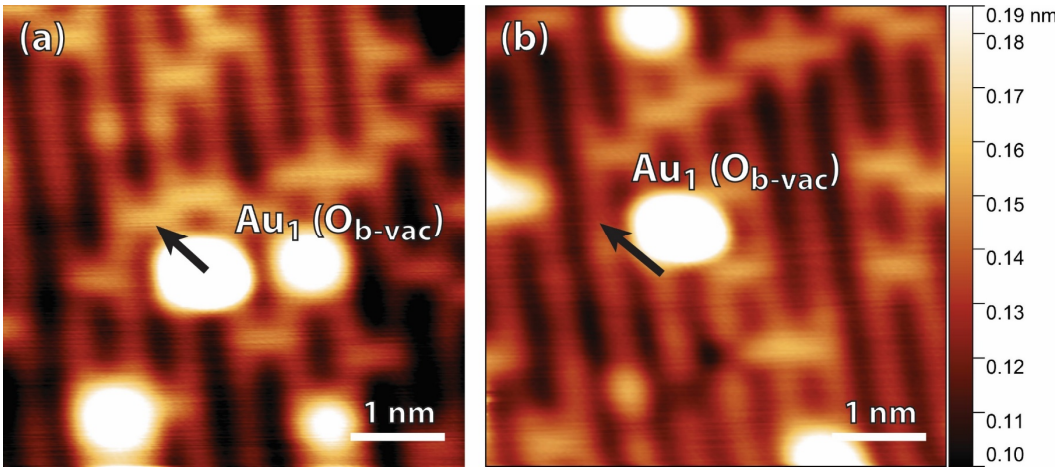

Fig.4.4, (a) STM image of an Au_1 species centred along an O_b row. (b) As (a), after an Au_1 species was displaced from its original position to an $O_{b\text{-}vac}$ site. A -2 V, 100 ms tip pulse was used to induce displacement. The original position of the Au_1 is revealed to be an $O_{b\text{-}vac}$ site. Arrows indicate the directions of tip-induced displacement of Au_1. Scan parameters: V_S = +1.2 V, I_T = 10 pA. All images were recorded at 78 K.

To provide further evidence that Au_1 binds to $O_{b\text{-}vacs}$, STM tip pulsing was used to laterally manipulate Au_1 on r-TiO_2 (110). Fig.4.4(a) and Fig.4.4(b) show atomically resolved STM images of Au_1 on r-TiO_2 (110) taken before (Fig.4.4(a)) and after (Fig.4.4(b)) application of a -2 V, 100 ms tip pulse above the central Au_1 feature. By tracking its position before and after pulsing, Au_1 appears to move from its original site into an $O_{b\text{-}vac}$ site on an adjacent O_b row. Comparing the appearance of Au_1 in both images there is no obvious difference between the Au_1 after movement to an $O_{b\text{-}vac}$ ($Au_{1\text{-}ov}$) or in its original position. This suggests both species are equivalent and therefore provides evidence that Au_1 bind at $O_{b\text{-}vac}$ sites. On closer inspection of Fig.4.4(b), the original position of the Au_1, which is now uncovered, is identified as an $O_{b\text{-}vac}$. To eliminate the possibility that an $O_{b\text{-}vac}$ was generated as a consequence of the applied tip pulse further tip pulses were performed over bare O_b rows using the same parameters. No $O_{b\text{-}vacs}$ could be

created by pulsing the bare r-TiO_2 (110). Minato *et al.* have shown it is possible to desorb O_b atoms using -2 V tip pulses, however in their work they use a pulse duration of 1 s compared to the 100 ms pulses applied in this work[55].

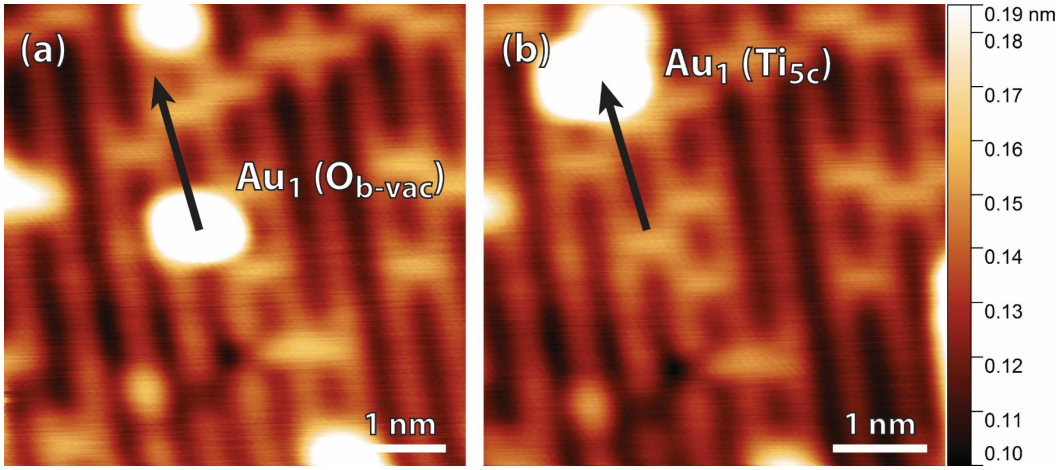

Fig.4.5, (a) STM image of an Au_1 species centred at an O_b row, as in Fig.4.4 (a). (b), as (a) after the Au_1 species was displaced from its original position to a Ti_{5c} site. *A -2 V, 100 ms tip pulse was used to induce displacement*. Arrows indicate the direction of tip-induced Au_1 movement. Scan parameters: V_S = +1.2 V, I_T = 10 pA. All images were recorded at 78 K.

In addition to movement from one $O_{b\text{-}vac}$ to another, Au_1 were observed moving from an $O_{b\text{-}vac}$ onto a Ti_{5c} row ($Au_{1\text{-}Ti}$) (centred over a Ti_{5c} site, see appendix A1) following application of a tip pulse (Fig.4.4(a)-(b)). The formation of these $Au_{1\text{-}Ti}$ species was observed in a minority of movement events. After several successive scans with STM (~20 minutes) the $Au_{1\text{-}Ti}$ were seen to spontaneously move onto nearby $O_{b\text{-}vacs}$ sites becoming $Au_{1\text{-}ov}$. After moving from $Au_{1\text{-}Ti}$ to $Au_{1\text{-}ov}$ no subsequent changes were observed, supporting the popular view that Au_1 binds weakly to Ti_{5c} sites and strongly to $O_{b\text{-}vacs}$[39,33,56,57]. In this case the observed $Au_{1\text{-}Ti}$ complex is likely to have been stabilised by the low temperature conditions used (78 K). This observation is in alignment with evidence that Au_1 nucleates at Ti_{5c} sites on stoichiometric TiO_2 (where no $O_{b\text{-}vacs}$ are present) and exhibits higher mobility compared with Au_1 on r-TiO_2 (110)[31,39]. Note that in Fig.4.5(b) an Au_1 species occupies a Ti_{5c} site with an OH_b close by. In this work, in contrast to the observations of Tong *et al.*, there was no observed tendency for $Au_{1\text{-}Ti}$ to move towards nearby OH_b[30].

4.3.5 | Mechanism of Au Manipulation

To determine the underlying mechanism of Au_1 displacement, a detailed statistical analysis of pulsing events was performed. During a pulsing experiment the STM tip is first centred over an Au_1 species. By monitoring the tunnelling current (I_T) for the duration of each pulse, after the desired sample bias is reached, a plot of I_T vs t is generated (Fig.4.6 inset). For each pulse a set point (I_T) is reached and held constant by the feedback loop of the STM. During each pulse an increase in the tip-sample distance, caused by the now absent Au_1, creates a sharp decrease in I_T. The feedback loop then acts to return I_T to the initial set point thereby forming a peak in the plot of I_T vs t. By measuring the time from when the initial set point is reached to the onset of the peak caused by the Au_1's displacement, one can determine the pulse duration required for displacement at that given parameter (see Fig.4.6 inset). By repeating this process many times, a distribution of Au_1 displacement times can be plotted for each set of pulsing parameters. In this work, over 1200 individual movement events were recorded across a range of voltages and set points (16 unique pulsing parameter sets). From the statistical distribution of displacement times the average lifetime of an Au_1 prior to displacement was then determined for each set of pulsing parameters.

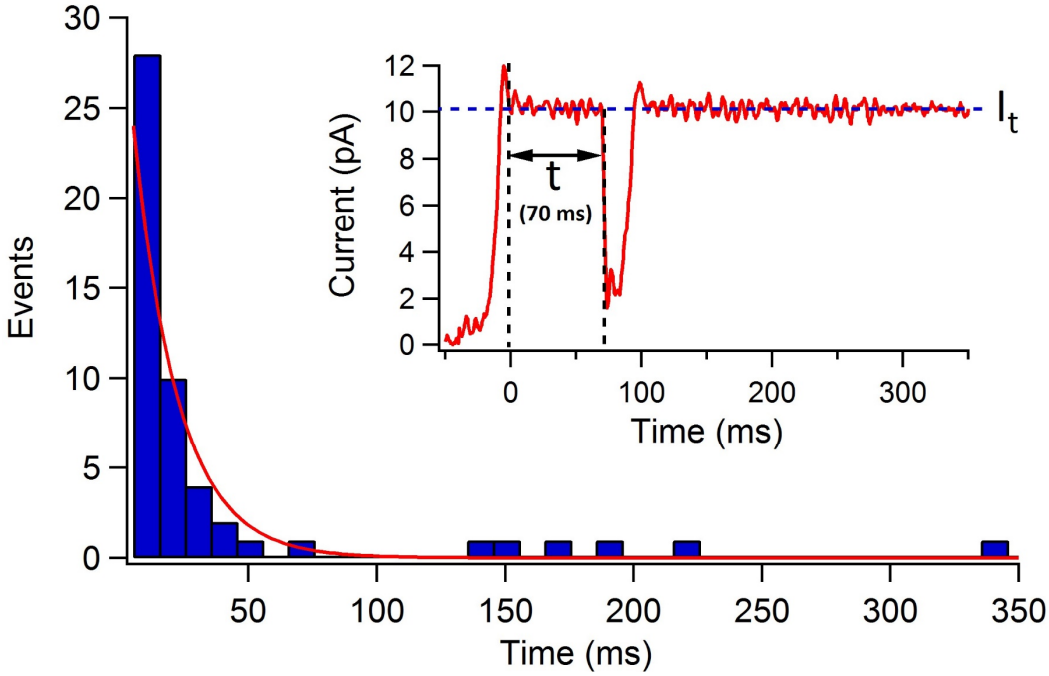

Fig.4.6, histogram showing the distribution of Au_1 displacement times for tip pulses of V_S = -1.8 V and I = 10 pA. The red line represents an exponential fit to the distribution of statistically independent events. The inset is an example of an individual I(t) trace used to compile the histogram where I_t is the set point of the pulse (10 pA) and τ is the pulse duration prior to Au displacement.

Fig.4.6 shows an example of the distribution of measured displacement times for a single pulsing parameter set plotted as a histogram. In this case tip pulses of -1.8 V and 10 pA were used. In a similar experiment, Acharya *et al.* have shown that STM tip induced dissociations of H adatoms from TiO_2 (110) follow an exponential distribution, this is also consistent with other studies in the literature[41-43,46,51,58]. Based on the literature, the following exponential function was fitted to the histogram of pulsing times for each recorded set of pulsing parameters (red line in Fig.4.6):

$$N(t) = A\exp\left(-\frac{t}{\tau}\right), \qquad (4.3.1)$$

where *t* is the pulse duration before displacement, A is the pre-exponential factor, N is the number of movement events and the decay constant, τ, represents the average lifetime of an Au_1 during a pulse (*i.e.* prior to displacement).

It is necessary to consider the appropriateness of assuming that the above data follows an exponential decay. By taking the natural logarithm, Eq. (4.3.1) can be written in the following linear form:

$$\ln(N_t) = \ln(\mathrm{A}) + \left(-\frac{t}{\tau}\right), \tag{4.3.2}$$

In theory, if the distribution of N_t does follow an exponential decay it should be possible to fit a linear function to a graph of $\ln(N_t)$ vs t, where the gradient of the line is equal to $\frac{-1}{\tau}$. As such a plot of $\ln(N_t)$ vs t was generated for each set of pulsing parameters, an example of this can be seen in Fig. 4.7. For the last 8 points on the graph (circled) N = 1 and they occur in random distribution of times, therefore, these points are attributed to random noise and omitted from the linear fitting (red line). From Fig. 4.7 it is apparent that the values of $\ln(N_t)$ vs t correspond well with a linear distribution thus confirming the assignment of Eq. (4.3.1) to N_t. Each fitting of $\ln(N_t)$ vs t was used to refine the value of τ for each data set collected.

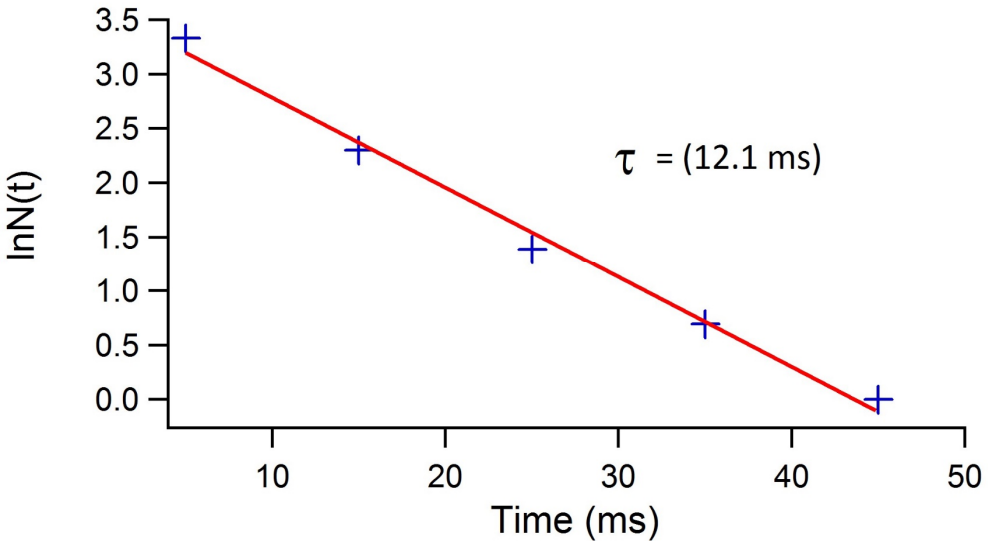

Fig. 4.7, plot of $\ln N_t$ vs Time for the data shown in Fig.4.6 (-1.8 V, 10 pA). The red line shows a linear fit to the data. The last 8 points of the plot (not shown) have been attributed to random noise and are omitted from the fitting. From the slope of the linear fit, τ was determined to be 12.1 ms. The fitting from this plot was used to refine the exponential fitting to the histogram shown in Fig.4.6.

When plotting a histogram, the width/number of bins used can have a significant effect on the distribution of the data, and this in turn affects the fitting of any function to that data. Using smaller/more bins allows for increased precision, however, if the bin size (count) it too small (large) then the data will appear flattened out and sampling noise may dominate over any real trend in the data. If the bin size (count) is too large (small) the signal-to-noise ratio of the data will be improved, but some features may be lost due to lack of precision see appendix A2.1. To plot a histogram effectively a compromise must be made regarding the number of bins to achieve a reasonable signal-to-noise ratio while maintaining precision. Though there are many methodologies for assigning bin widths/count there is no 'correct' method and these generally make assumptions regarding the data distribution. Trial and error is most commonly used to determine suitable binning by plotting multiple histograms of the same data set with varying bin sizes/counts. The most suitable bin width/count is then chosen based on the most reasonable distribution of the data considering the goal of the analysis. In this work, multiple histograms were plotted for each data set with varying bin sizes/counts. For each histogram, a plot of $\ln(N_t)$ vs t was generated to help assess the appropriateness of the binning for that histogram, and the most sensible distribution was then chosen from those plotted. Histogram bin size/count was also found to influence the calculated values of τ. Therefore, for each data set multiple of histograms were plotted within a 'sensible' bin width/count range. The variation of τ within this range was then factored into the quoted error of τ.

Appendix A2.1 shows an example of three histograms plotted from same data set with 25, 50 and 500 bins. Insets show corresponding plots of $\ln(N_t)$ vs t. It is clear from the fitting of a linear function to $\ln(N_t)$ vs t that, in this case, 50 bins yielded the most suitable data distribution. The calculated values of τ for each histogram is given in appendix A2.2 together with the bin widths used.

While τ is equal to the lifetime of an Au_1 during an STM tip pulse, $\frac{1}{\tau}$ represents the rate of Au_1 displacement, R. In the literature, it has been shown that by exploring the relationship between R and I_T one can infer the underlying mechanism of STM tip induced displacement/desorption. Surface reactions induced by tunnelling electrons are typically interpreted as occurring via one of two mechanisms. The first involves singular electronic excitation of a surface adsorbate, where an electron is promoted into an anti-bonding state. This results in motion of the adsorbate along an adiabatic potential and is called the Menzel-Gomer-Redhead model (MGR). In this case, the applied bias required is usually relatively high, and R has a linear dependence on I_T

$$R \propto I_T. \tag{4.3.3}$$

In the second mechanism, called the ladder climbing model, a vibrational mode of the surface/adsorbate species becomes directly excited by an inelastically tunnelling electron. If the energy of this excited vibrational mode, $\hbar\omega$, is greater than the potential barrier for adsorbate motion along a particular reaction coordinate, E_B, lateral motion of the adsorbate can occur. When $\hbar\omega < E_B$, energy can be accumulated by multiple excitation of the vibrational mode via successive inelastically tunnelling electrons. For this process to occur, the rate of energy dissipation of the vibrational mode must be lower than its rate of excitation. Eventually the accumulated energy of the excited vibrational mode may exceed E_B, thereby inducing displacement of the adsorbate. Compared to the MGR model, ladder climbing mechanisms typically require lower applied bias, and, as it involves multiple electronic excitations, R has a power law relationship with I_T

$$R \propto {I_T}^n, \tag{4.3.4}$$

where n is the number of vibrational excitations required (reaction order)[59].

Given that the value of I_T is constant and known during a tip pulse, it is common practice to express the rate of dissociation in terms of the number of displacement events that occur per tunnelling electron, this is known as the quantum yield, Y. Remembering that R = $\frac{1}{\tau}$, Y can be calculated from τ using Eq. (4.3.5):

$$Y = \frac{e}{I_T \tau}, \tag{4.3.5}$$

where *e* denotes the elementary charge (1.602×10^{-19} C). It is important to note that $Y \propto \frac{R}{I_T}$. Therefore, unlike R, Y automatically accounts for variations in excitation probability due to increased electron flux (higher I_T). As such, Y values collected at different set points can be compared directly. This in turn allows one to assess the variation of τ with I_T. Considering Eqs. (4.3.3) and (4.3.4), one can infer the following relationship:

$$Y \propto {I_T}^{(n-1)}, \tag{4.3.6}$$

In the MGR model Y is independent of I_T, therefore, the exponent of Eq. (4.3.5) becomes zero, as is expected for a single electron process. Conversely, in the ladder climbing model Y is dependent on I_T and the exponent of Eq. (4.3.5) is equal to n-1. Using logarithms, Eq. (4.3.5) can be expressed in the following linear form:

$$\log_{10} Y = A + (n-1)\log_{10} I_T. \tag{4.3.7}$$

From this it is apparent that, one should be able to distinguish between an MGR or ladder climbing model by fitting a linear function to a plot of log(Y) vs log(I_T), where the gradient of the line is equal to (n-1). (*i.e.* an MGR displacement

mechanism (single electronic excitation) will result in a linear gradient of 0, whereas for a ladder climbing model mechanism the gradient will be >1)[44,46,57-59].

After pulsing, no 'area of effect' was observed in subsequent STM images (only one Au_1 moved per pulse). This observation is characteristic of an electron mediated manipulation processes and rules out a purely field induced effect[50]. It is worth pointing out, as tunnelling current increases tip-sample distance decreases, therefore the influence of the tips electric field will become more significant at higher currents. This increasing field effect may explain the increased error for measurements collected above 100 pA. Further statistical analysis was hindered by two factors. Firstly, the rate of Au_1 displacement tends to increase with increasing bias voltage. For pulses ≤ -2.0 V the speed of displacement regularly exceeded the maximum temporal resolution of the STM, making subsequent data analysis increasingly inaccurate. Secondly, at higher currents (>300 pA) Au_1 was seen to desorb from the surface rather than being displaced laterally. As it cannot be assumed the mechanism underlying desorption is the same as for displacement, all desorption events were omitted from this analysis.

From the tip pulsing data collected in this experiment, a series of histograms, like the one shown in Fig.4.6, were plotted for each set of pulsing parameters (bias voltages of -1.6, -1.7, -1.8 and -1.9 V collected across a range of set points from 1 to 300 pA). The dependence of Y on I_T was then extracted from this using Eq. 4.3.7. Fig.4.8Fig. *4.7* shows the experimentally-obtained plot of log(Y) vs log(I_T). From Fig.4.8, for each voltage parameter log(Y) has a clear linear dependence on log(I_T), with a gradient of approximately 1 (avg. 0.96), thereby, evidencing a reaction order of 2 (see Eq. (4.3.6)). This rules out a single electronic excitation mechanism (MGR model) and supports a ladder climbing mechanism, where two tunnelling electrons successively excite a vibrational mode of the Au_1/TiO_2 species before the dissociation barrier is exceeded and Au_1 is displaced. In the literature, similar investigations have also evidenced ladder climbing

mechanisms for STM tip induced adsorbate displacement/desorption over various sustrates[41,48,60].

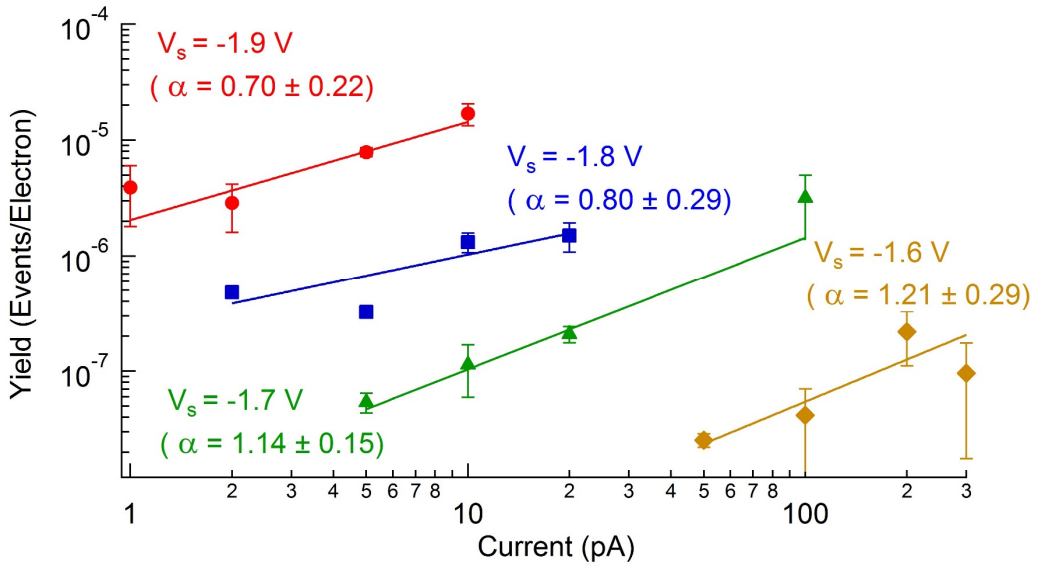

Fig.4.8, double-logarithmic plot of displacement yield, Y, as a function of tunnelling current, I_T. Solid circles, squares, triangles and rhombi represent the measured yields of Au_1 displacements at different pulse voltages (labelled). Lines show power-law fits to the experimental data, with exponents (α) given for each pulse voltage.

Previous work in the literature by Chrétien and Metiu suggests, for the Au/TiO_2 system, the high energy singularly occupied Au 6s orbital overlaps favourably with states in the conduction band of the reduced substrate localised at Ti_{5c} sites[33]. From this, they conclude that Au covalently bonds to Ti_{5c} atoms either side of an $O_{b\text{-}vac}$ on the surface. The oscillation of such a covalent bond could provide the vibrational mode required for the proposed ladder climbing mechanism. A schematic illustration of the Au_1/Ti_{5C} ladder climbing mechanism is given in Fig.4.9 showing the reaction coordinate for Au displacement and the two-dimensional potential of the Au_1/Ti_{5c} vibrational mode. Chrétien and Metiu further propose that the singularly occupied Au 6s orbital is only present for Au_n where n is odd[39,33]. This corresponds well with STM observations of the Au/TiO_2 system showing Au_1 and Au_3 are the dominant species on r-TiO_2 at low Au coverage, while Au_2 species are seemingly absent.

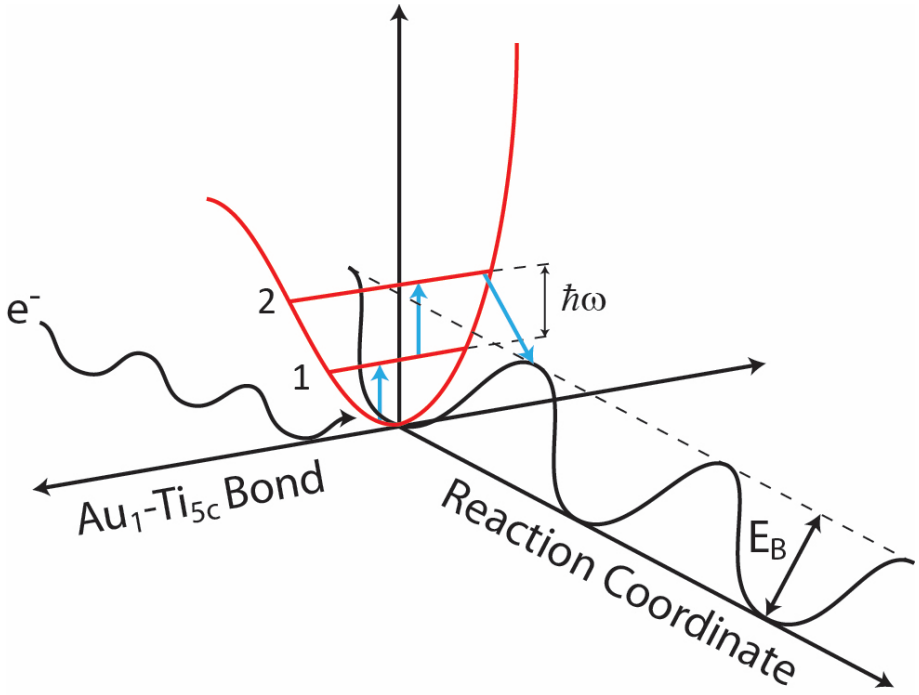

Fig.4.9, schematic illustration of the proposed vibrationally assisted ladder climbing mechanism for STM pulse induced Au_1 dissociation. The potential well for the Au_1-Ti_{5c} vibrational mode is shown on one axis, while the reaction coordinate for Au_1 displacement is shown on another. An incoming inelastically tunnelling electron excites the Au_1-Ti_{5c} vibrational mode from its ground state to its first excited state (1). A second incoming electron then excites the vibrational mode to its second excited state (2), which has an energy greater than E_B. Through anharmonic coupling with the excited vibrational mode, energy is transferred to the reaction coordinate allowing it to overcome E_B. Subsequently Au_1 dissociates from its adsorption site and can move laterally along the TiO_2 surface.

Given the proposed mechanism of successive excitation of a vibrational mode by two incoming electrons, it follows that the time required to induce Au_1 displacement (τ) is inversely related to the lifetime of the excited vibrational mode. From Fig.4.8 the value of Y increases with applied pulse bias and set point. As Y is calculated from τ for a given set of pulsing parameters, it can be concluded that the lifetime of the excited Au_1/Ti_{5c} vibrational mode increases as the energy and/or flux of the inelastically tunnelling electrons is increased. Given that the manipulation mechanism is determined to be a two-electron process at tunnelling currents as low as 1 pA (corresponding to 10^7 electrons per second), one can deduce that the vibrational life time must be at least 0.1 ns when using tip pulses of 1.9 V. Vibrational lifetimes of adsorbates on metals are typically of the order of 1 ps. However, due to much less efficient vibrational de-excitation mechanisms,

this can be much longer on wide bandgap semiconductors (such as TiO_2), typically on the order of 1 ns[58]. This fits well with the observation of a minimum vibrational lifetime of 0.1 ns for the Au/TiO_2 during an STM tip pulse.

4.4 | Summary and Conclusions

The adsorption of small Au clusters on a r-TiO_2 (110) surface has been investigated using STM. Using both in-situ dosing and Au_1 manipulation, the adsorption site of Au_1 has been directly visualised and identified to be $O_{b\text{-}vacs}$, thereby providing a conclusive answer to the question of Au atom adsorption on r-TiO_2 (110). Moreover, using statistical analysis of the employed manipulation method, the relationship between displacement yield (Y) and tunnelling current (I_T) has been deduced. This has revealed Au_1 manipulation to be a two-electron process, indicating vibrational excitation as the likely mechanism. Such evidence further supports previous suggestions of Au_1 covalently bonding to Ti_{5c} atoms either side of an $O_{b\text{-}vac}$[28,30,31,34,39,61].

4.6 | References

1. Tenney, S. A., He, W., Ratliff, J. S., Mullins, D. R. & Chen, D. A. Characterization of Pt-Au and Ni-Au clusters on TiO_2(110). *Top. Catal.* **54,** 42–55 (2011).

2. Tang, Y. *et al.* Electronic states of metal (Cu, Ag, Au) atom on CeO_2(1 1 1) surface: The role of local structural distortion. *J. Power Sources* **197,** 28–37 (2012).

3. Chen, Y., Hu, P., Lee, M. H. & Wang, H. F. Au on (111) and (110) surfaces of CeO_2: A density-functional theory study. *Surf. Sci.* **602,** 1736–1741 (2008).

4. Okazaki-Maeda, K., Maeda, Y., Morikawa, Y., Tanaka, S. & Kohyama, M. Study of Interaction between Au and TiO_2(110) at Low Coverage. *Mater. Trans.* **47,** 2663–2668 (2006).

5. Rodriguez, J. A., Liu, P., Hrbek, J., Evans, J. & Pérez, M. Water gas shift reaction on Cu and Au nanoparticles supported on CeO_2(111) and ZnO(0001): Intrinsic activity and importance of support interactions. *Angew. Chemie - Int. Ed.* **46,** 1329–1332 (2007).

6. Chrétien, S., Buratto, S. K. & Metiu, H. Catalysis by very small Au clusters. *Curr. Opin. Solid State Mater. Sci.* **11,** 62–75 (2007).

7. Rodriguez, J. A., Liu, P., Pérez, M., Liu, G. & Hrbek, J. Destruction of SO_2 on Au and Cu nanoparticles dispersed on MgO(100) and CeO2(111). *J. Phys. Chem. A* **114,** 3802–3810 (2010).

8. Sterrer, M. *et al.* Control of the charge state of metal atoms on thin MgO films. *Phys. Rev. Lett.* **98,** 1–4 (2007).

9. Connelly, K., Wahab, a. K. & Idriss, H. Photoreaction of Au/TiO_2 for hydrogen production from renewables: a review on the synergistic effect between anatase and rutile phases of TiO_2. *Mater. Renew. Sustain. Energy* **1,** 3 (2012).

10. Chen, M. S. & Goodman, D. W. The structure of catalytically active gold on titania. *Science* **306,** 252–5 (2004).

11. Haruta, M. Size- and support-dependency in the catalysis of gold. *Catal. Today* **36,** 153–166 (1997).

12. Iizuka, Y. *et al.* Adsorption of CO on gold supported on TiO_2. *Catal. Today* **36,** 115–123 (1997).

13. Williams, W. D. *et al.* Metallic corner atoms in gold clusters supported on rutile are the dominant active site during water-gas shift catalysis. *J. Am. Chem. Soc.* **132,** 14018–14020 (2010).

14. Pang, C. L., Lindsay, R. & Thornton, G. Chemical reactions on rutile TiO_2(110). *Chem. Soc. Rev.* **37,** 2328–2353 (2008).

15. Connelly, K. A. & Idriss, H. The photoreaction of TiO_2 and Au/TiO_2 single crystal and powder surfaces with organic adsorbates. Emphasis on

hydrogen production from renewables. *Green Chem.* **14,** 260–280 (2012).

16. Waterhouse, G. I. N. & Idriss, H. in *On Solar Hydrogen & Nanotechnology* (ed. Vayssieres, L.) 77–89 (John Wiley & Sons, Ltd, 2009).

17. Diebold, U. Structure and properties of TiO_2 surfaces: A brief review. *Appl. Phys. A Mater. Sci. Process.* **76,** 681–687 (2003).

18. Pang, C. L., Lindsay, R. & Thornton, G. Structure of clean and adsorbate-covered single-crystal rutile TiO_2 surfaces. *Chem. Rev.* **113,** 3887–3948 (2013).

19. Diebold, U. The Surface Science of Titanium Dioxide. *Appl. Surf. Sci.* **48,** 53–229 (2003).

20. Batzill, M., Katsiev, K., Gaspar, D. J. & Diebold, U. Variations of the local electronic surface properties of TiO_2(110) induced by intrinsic and extrinsic defects. *Phys. Rev. B* **66,** 235401 (2002).

21. Minato, T. *et al.* The electronic structure of oxygen atom vacancy and hydroxyl impurity defects on titanium dioxide (110) surface. *J. Chem. Phys.* **130,** 124502 (2009).

22. Busayaporn, W. *et al.* Geometric structure of TiO_2 (110) (1×1): Confirming experimental conclusions. *Phys. Rev. B* **81,** 153404 (2010).

23. Eigler, D. M. & Schweizer, E. K. Positioning single atoms with a scanning tunnelling microscope. *Nature* **344,** 524–526 (1990).

24. Rohrer, G. S., Henrich, V. E. & Bonnell, D. A. A scanning tunneling microscopy and spectroscopy of the TiO_{2-x} (110) surface. (1992).

25. Papageorgiou, A. C. *et al.* Electron traps and their effect on the surface chemistry of TiO_2(110). *Proc. Natl. Acad. Sci. U. S. A.* **107,** 2391–6 (2010).

26. Henderson, M. A. the Interaction of Water With Solid Surfaces : Fundamental Aspects. *Surf. Sci. Rep.* **46,** 1–308 (2003).

27. Henderson, M. A., Otero-Tapia, S. & Castro, M. E. The chemistry of

methanol on the TiO_2(110) surface: the influence of vacancies and coadsorbed species. *Faraday Discuss.* **114,** 313–329 (1999).

28. Okazawa, T., Kohyama, M. & Kido, Y. Electronic properties of Au nano-particles supported on stoichiometric and reduced TiO_2(1 1 0) substrates. *Surf. Sci.* **600,** 4430–4437 (2006).

29. Thomas, J. M. Tens of thousands of atoms replaced by one. *Nature* **525,** 325–326 (2015).

30. Tong, X. *et al.* Direct visualization of water-induced relocation of au atoms from oxygen vacancies on a TiO_2(110) surface. *J. Phys. Chem. C* **114,** 3987–3990 (2010).

31. Matthey, D. *et al.* Enhanced Bonding of Gold Nanoparticles on Oxidized TiO_2(110). *Science* **315,** 1692 (2007).

32. Lee, S., Fan, C., Wu, T. & Anderson, S. L. CO Oxidation on Au_n/TiO_2 Catalysts Produced by Size-Selected Cluster Deposition. *J. Am. Chem. Soc.* **126,** 5682–5683 (2004).

33. Ammal, S. C. & Heyden, A. Modeling the noble metal/TiO_2 (110) interface with hybrid DFT functionals: A periodic electrostatic embedded cluster model study. *J. Chem. Phys.* **133,** (2010).

34. Wang, Y. & Hwang, G. S. Adsorption of Au atoms on stoichiometric and reduced TiO_2(110) rutile surfaces: A first principles study. *Surf. Sci.* **542,** 72–80 (2003).

35. Zhang, Z., Tang, W., Neurock, M. & Yates, J. T. Electric charge of single Au atoms adsorbed on TiO_2(110) and associated band bending. *J. Phys. Chem. C* **115,** 23848–23853 (2011).

36. Wörz, A. S., Heiz, U., Cinquini, F. & Pacchioni, G. Charging of Au atoms on TiO_2 thin films from CO vibrational spectroscopy and DFT calculations. *J. Phys. Chem. B* **109,** 18418–18426 (2005).

37. Chang, T. Y. *et al.* Direct imaging of pt single atoms adsorbed on TiO_2

(110) Surfaces. *Nano Lett.* **14,** 134–138 (2014).

38. Lustemberg, P. G. *et al.* Diffusion Barriers Block Defect Occupation on Reduced CeO_2(111). *Phys. Rev. Lett.* **116,** 236101 (2016).

39. Chŕtien, S. & Metiu, H. Density functional study of the interaction between small Au clusters, Au_n (n=1-7) and the rutile TiO_2 surface. II. Adsorption on a partally reduced surface. *J. Chem. Phys.* **127,** 244708 (2007).

40. Iachella, M. *et al.* Promoter effect of hydration on the nucleation of nanoparticles: direct observation for gold and copper on rutile TiO_2 (110). **8,** 16475–16485 (2016).

41. Chiaravalloti, F., Riedel, D., Dujardin, G., Pinto, H. P. & Foster, A. S. STM topography and manipulation of single Au atoms on Si(100). *Phys. Rev. B* **79,** 245431 (2009).

42. Sloan, P. A. & Palmer, R. E. Two-electron dissociation of single molecules by atomic manipulation at room temperature. *Nature* **434,** 367–71 (2005).

43. Nickel, A. *et al.* Moving nanostructures: Pulse-induced positioning of supramolecular assemblies. *ACS Nano* **7,** 191–197 (2013).

44. Repp, J., Meyer, G., Olsson, F. E. & Persson, M. Controlling the charge state of individual gold adatoms. *Science* **305,** 493–495 (2004).

45. Kühnle, A., Meyer, G., Hla, S. W. & Rieder, K. H. Understanding atom movement during lateral manipulation with the STM tip using a simple simulation method. *Surf. Sci.* **499,** 15–23 (2002).

46. Kraus, A., Hanbücken, M., Koshikawa, T. & Neddermeyer, H. Manipulation experiments on Si(111)7 x 7 by scanning tunnelling microscopy. *Surf. Interface Anal.* **37,** 96–100 (2005).

47. Tikhodeev, S. G. & Ueba, H. How vibrationally assisted tunneling with STM affects the motions and reactions of single adsorbates. *Phys. Rev. Lett.*

102, 1–4 (2009).

48. Sloan, P. A., Hedouin, M. F. G., Palmer, R. E. & Persson, M. Mechanisms of Molecular Manipulation with the Scanning Tunneling Microscope at Room Temperature: Chlorobenzene. *Phys. Rev. Lett.* **91,** 118301 (2003).

49. Dolocan, A., Acharya, D. P., Zahl, P., Sutter, P. & Camillone, N. Two-color ultrafast photoexcited scanning tunneling microscopy. *J. Phys. Chem. C* **115,** 10033–10043 (2011).

50. Momose, T. *et al.* Molecular motion induced by multivibronic excitation on semiconductor surface. *J. Phys. Chem. C* **118,** 1554–1559 (2014).

51. Pan, T. L., Sakulsermsuk, S., Sloan, P. A. & Palmer, R. E. Site- and energy-selective intramolecular manipulation of polychlorinated biphenyl (PCB) molecules. *J. Am. Chem. Soc.* **133,** 11834–11836 (2011).

52. Göpel, W. *et al.* Surface defects of TiO_2(110): A combined XPS, XAES and ELS study. *Surf. Sci.* **139,** 333–346 (1984).

53. Bikondoa, O. *et al.* Direct visualization of defect-mediated dissociation of water on TiO_2(110). *Nat. Mater.* **5,** 189–192 (2006).

54. Shibata, N. *et al.* Interface structures of gold nanoparticles on TiO_2(110). *Phys. Rev. Lett.* **102,** 136105 (2009).

55. Minato, T., Kawai, M. & Kim, Y. Creation of single oxygen vacancy on titanium dioxide surface. *J. Mater. Res.* **27,** 2237–2240 (2012).

56. Pabisiak, T. & Kiejna, A. Stability of gold nanostructures on rutile TiO_2(110) surface. *Surf. Sci.* **605,** 668–674 (2011).

57. Okazaki, K., Ichikawa, S., Maeda, Y., Haruta, M. & Kohyama, M. Electronic structures of Au supported on TiO_2. *Appl. Catal. A Gen.* **291,** 45–54 (2005).

58. Acharya, D. P., Coibanu, C. V., Camillone, N. III, & Sutter, P. Mechanism of Electron Induced Hydrogen Desorption from Hydroxylated Rutile TiO_2 (110). *J. Phys. Chem. C* **114,** 21510-21515 (2010).

59. Momose, T. *et al.* Molecular Motion Induced by Nultivibronic Excitation on Semiconductor Surface. *J. Phys. Chem. C* **118,** 1554-1559 (2013).

60. Hla, S.-W. Scanning tunneling microscopy single atom/molecule manipulation and its application to nanoscience and technology. *J. Vac. Sci. Technol. B Microelectron. Nanom. Struct.* **23,** 1351 (2005).

61. Chen, M. S. & Goodman, D. W. Interaction of Au with titania: The role of reduced Ti. *Top. Catal.* **44,** 41–47 (2007).

Chapter 5

Spectroscopic Investigations of Au Nanoparticles on Rutile TiO_2 (110) with Synchrotron Radiation

Outline

Owing to their significance in several industrial processes, like green production of clean hydrogen, Au nanoparticles have become a highly pursued topic in catalysis[1]. For future catalyst design, it is essential to develop a greater understanding of the unique properties of Au nanoparticles. The choice of support material has been shown to have a dramatic effect on catalytic activity of nanoparticles, and the question of electron transfer between nanoparticle and substrate is a much debated aspect of Au based catalysis[2–4]. Photoelectron spectroscopy (PES) has been widely employed to explore the electronic characteristics of nanoparticles and their interactions with substrate

materials[5–10]. In particular, PES shows how the binding energy of core level electrons varies with Au particle size[11]. Such shifts can be explained by changes in the nanoparticle electronic configuration, and in some cases this can be used to evidence charge transfer with the substrate. In the case of Au on TiO_2, the extent of reduction of the substrate can have a dramatic effect on nanoparticle activity[12,13]. Precise control of sample reduction can be difficult. As such, the extent of reduction often varies from sample to sample or even between different preparations of the same sample. Differences between samples can affect core level electron binding energies and therefore complicate the interpretation of such data. Au/TiO_2 samples have been created using an STM 'tip-shadowing' method, whereby discrete regions of varying Au coverage are deposited onto a single Au/TiO_2 sample. After preparation of such a sample, XPEEM was employed to collect spatially resolved core level spectra from each Au coverage region, and therefore binding energy shifts could be recorded as a function of particle size alone. Experiments were carried out at the UK's synchrotron radiation facility Diamond Light Source (beamline IO6). In addition, the effects of synchrotron beam damage on the sample were explored, and it was found that introducing O_2 into the vacuum could effectively counteract photon-induced reduction of the TiO_2 surface.

5.1 | Introduction

For metal oxide supported Au nanoparticles, the exact nature of the substrate has been shown to play an important role in catalysis[14,15]. TiO_2 in particular has been widely studied, not only for its own catalytic capabilities but, as a model metal oxide substrate[16–18]. Reduction of TiO_2 generates an electronic state within the band gap of the material[19]. The presence of this band-gap-state

(BGS) is associated with the generation of defects such as interstitial Ti atoms and bridging oxygen vacancies ($O_{b\text{-}vac}$) in the bulk and at the surface[20–22]. On rutile TiO_2, $O_{b\text{-}vacs}$ act as electron trap sites and often play a role in surface mediated molecular reactions[23]. $O_{b\text{-}vacs}$ are typically characterised by an area of excess electron density[24]. Minato *et al.*, and more recently Yim *et al.*, have shown that the electronic charge associated with an $O_{b\text{-}vac}$ (polaron) is localised around the neighbouring Ti_{5c} atoms[25,26].

Regarding Au catalysis, the nanoparticle charge state is expected to play a critical role in the interactions between Au and reactant molecules on the surface. Understanding the interactions between surface polarons and Au nanoparticles, specifically the nature of electron transfer, is key to understanding the increased catalytic activity of the Au/TiO_2 system over pure TiO_2. The nanoparticle charge state remains one of the most heavily disputed aspects of Au/TiO_2 catalysts and, while many independent studies appear in the literature, a consensus has yet to be reached[16,27–29]. Ultraviolet photoelectron spectroscopy (UPS) studies of Au/TiO_2 conducted by Minato *et al.* and Okazawa *et al.* both show reduction of BGS intensity as the Au coverage increases[24,30]. Each group differs in their interpretation of the nature of this interaction. Minato *et al.* surmise that band gap quenching evidences electron transfer from $O_{b\text{-}vacs}$ to Au nanoparticles, thereby creating anionic Au species[24,31]. In contrast, Okazawa *et al.* suggest that $O_{b\text{-}vacs}$ are characterised by electron deficiency. This leads them to conclude that electrons are transferred from Au to the substrate, forming cationic Au. Using Kelvin probe force microscopy Chung *et al.* support Minato *et al.*'s interpretation by providing indirect evidence of anionic Au on TiO_2. Unlike Minato *et al.* and Okazawa *et al.*, however, Chung *et al.* studied Au on a hydroxylated, rather than reduced, TiO_2 sample. This may be the source of discrepancies between their results and others[31]. A more recent PES study by Wendt et al shows no reduction in TiO_2 band gap state intensity as Au is deposited, suggesting Au nanoparticles are neutral[32].

In 2001, Guo *et al.* provided evidence that TiO_2 supported Au nanoparticles transition from metallic to non-metallic character as the nanoparticle diameter decreases from 3 to 2 nm[33]. This transition coincides with the onset for catalytic activity of Au nanoparticles, which has been well studied in the literature for various systems[34–37]. The density of surface active sites alone does not adequately account for the outstanding activity of Au nanoparticles, and therefore other phenomena must be considered to better understand the Au/TiO_2 system[38]. Core level spectroscopy is the technique of choice for monitoring changes in electronic structure. In some cases, shifts in core level binding energy have been shown to reveal the charge state of a sample, from which one can infer the nature of charge transfer to/from that material. The core level electron binding energies of nanoparticles are also influenced by initial and final state effects, making their interpretation more difficult.

Initial state effects arise from intrinsic factors of the nanoparticles themselves, *i.e.* the 'initial' electronic state of the system. As the particle size decreases, the ratio of surface-to-bulk atoms increases. Due to undercoordination of the surface atoms, this causes the d-band of the nanoparticles to shift towards the Fermi level, resulting in a negative binding energy shift of the core level electrons. Charge transfer to/from the nanoparticles is also considered an initial state effect and can cause either positive or negative shifts in core level electron binding energy[39]. Final state effects arise from differences in the electronic structure of a system after photoemission *i.e.* its 'final' electronic state. The ionised species will have a coulombic potential that does work on the photoemitted electron, thereby reducing its kinetic energy. This results in an apparently positive shift in the measured binding energy of the photoelectron. When an electron is removed from an atom, the local electronic environment will relax to stabilise the newly generated core hole (screening). If relaxation occurs before an ejected electron is completely decoupled from the system, the coulombic effect of the 'final' state on that electron will be reduced. As particle size increases, the electronic relaxation of a system becomes easier as the core

hole can be delocalised over the cluster. The net result of these effects is an apparently positive core level binding energy shift, which reduces in magnitude as particle size increases. In addition to particle size, final state effects are strongly related to the nanoparticle support material[40-42].

Much effort has gone into elucidating the role that initial and final state effects play on the binding energy of core level electrons for Au nanoparticles supported on various substrate materials (SiO_2, C, NaCl, HOPG, ZrO_2). These studies show positive shifts in core level binding energy as particle size decreases[43,44]. Whether this is due to initial or final state effects has been widely disputed, but it seems likely that both effects are present. Cordes and Harsdorff hypothesise that core level shifts are mainly due to relaxation processes, *i.e.* final state effects, while initial state effects have a dominant influence over the valence band[34]. Based on XANES measurements in the literature, Meyer *et al.* remark that positive binding energy shifts of the Au 4f core level for silica supported Au nanoparticles, observed by XPS, must arise from final state effects[15]. By accounting for final state effects, using XPS one can infer Au charge state from core level binding energy shifts as a function of nanoparticle diameter. Determining the nature of charge transfer between Au and TiO_2 using this methodology is complicated by the fact that the interactions between Au and $O_{b\text{-}vacs}$ are not yet fully understood.

In this work, to eliminate any discrepancies arising from the reduction state of the substrate, Au was deposited onto a rutile TiO_2 (110) surface in discrete regions of varying coverage. This means that binding energy shifts could be measured as a function of Au particle size over areas with exactly the same level of reduction. Therefore, shifts in core level binding energy measured from this sample arise solely from particle size variations. To create this sample, the tip of an STM was utilised to develop a 'tip-shadowing' method of vapour deposition. Synchrotron radiation (Diamond Light Source UK) was then employed to record spatially resolved core level spectra of the various Au coverage regions on the sample. Initially, high intensity photon irradiation induced significant, irreversible

reduction of the TiO_2 substrate. The dynamics of this 'beam damage' effect were explored further. Introducing a partial pressure of O_2 into the vacuum could effectively counteract any photon-induced sample reduction.

5.2 | Experimental Procedure

UV photoelectron emission microscopy (UV-PEEM), X-ray photoelectron emission microscopy (XPEEM), scanning tunnelling microscopy (STM) and micro-spot low energy electron diffraction (μLEED) measurements were performed at the IO6 beamline in the UK synchrotron facility Diamond Light Source. All experiments were carried out in a two chamber, ultra-high vacuum (UHV) system with a base pressure of 10^{-10} mbar (see Chapter 3). The preparation chamber was equipped with an Omicron *GmbH* variable-temperature STM, ion sputter gun, sample heater, EFM III line-of-sight e-beam doser and facilities for STM, low energy electron diffraction (LEED) and Auger (AES) analysis. The analysis chamber comprised of an Elmitec LEEM III spectroscopic photoemission and low energy electron microscope (SPELEEM) with a UHV leak valve (connected to an O_2 line). Using the Elmitec LEEM III, it was possible to use a variety of analytical techniques including UV-PEEM, XPEEM and μLEED. A rutile TiO_2 (110) (1×1) single crystal (MaTecK) sample was prepared in the preparation chamber via successive cycles of argon ion sputtering and vacuum annealing to 1000 K. Sample cleanliness and long-range order were verified using AES and μLEED respectively. XPEEM measurements were collected for a range of O_2 partial pressures as controlled via the UHV leak valve. A beam energy of 200 eV was used to collect core level spectra via XPEEM. STM images were collected using constant current mode at 300 K with an electrochemically etched tungsten tip (see Chapter 3). Au deposition was performed in the preparation chamber using the EFM III line-of-sight doser. The deposition source consisted of an Au sample placed in the recess of a molybdenum crucible, which was heated via electron bombardment. The subsequent molecular beam was directed onto a TiO_2 (110) sample, while in the sample stage of the VT-STM. A constant e-beam flux of 100 nA (I_{fil} = 1.77 A @ 850 V) was maintained during Au deposition and exposure time was varied to obtain the desired Au coverage. The STM tip was used to create regions on the

sample surface of different Au coverage. This method is explained in more detail in section 5.3.

5.3 | Results and Discussion

5.3.1 | Au/TiO_2 Sample Preparation

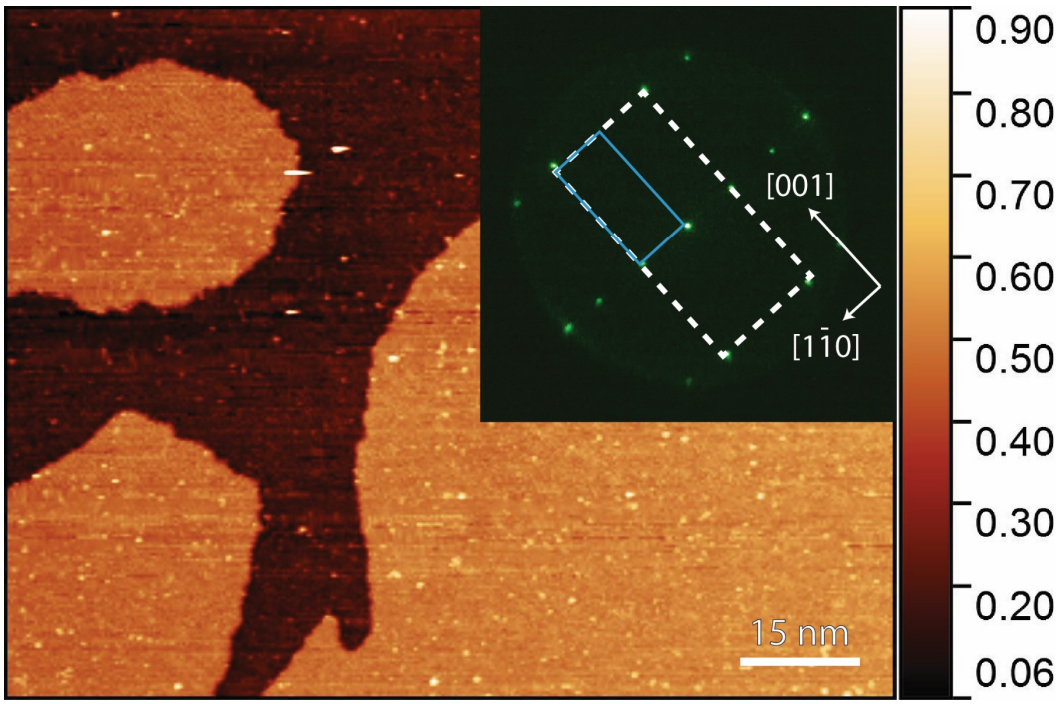

Fig. 5.1, STM topography image of the clean, as prepared TiO_2 surface after successive cycles of Ar ion sputtering and annealing to 1000 K. Inset shows a LEED pattern collected from the sample at 35 eV using µLEED. A sharp 1×1 Rutile LEED pattern is seen. Integer diffraction spots are indicated by blue solid and white dashed rectangles, respectively. The z-scale of the colour map used is given, in nm, on the right-hand side of the image. STM scan parameters: V_S = +1.4 V, I_T = 100 pA. Scale bar: 15 nm. Recorded at 300 K.

A clean Rutile TiO_2 (110) sample was prepared by successive cycles of Ar ion sputtering and vacuum annealing to 1000 K. After preparation, the surface cleanliness and long range order were verified by STM and µLEED respectively. Fig. 5.1 shows an STM image taken from the sample, after preparation, exhibiting large flat terraces on the surface. The inset of Fig. 5.1 shows a diffraction pattern, taken from the surface via µLEED, that corresponds well with an ordered 1×1 rutile surface.

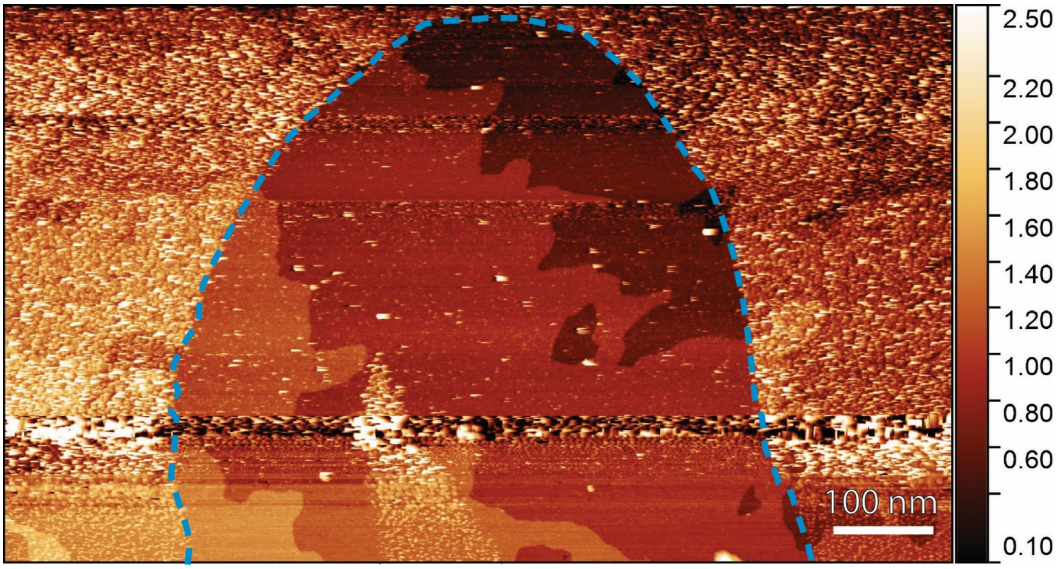

Fig.5.2, STM topography image of the TiO_2 surface after ~0.4 MLE of Au has been deposited using the tip-shadow method. The blue dashed line indicates the edge of the tip-shadow. Within the tip-shadow, terraces of the bare TiO_2 surface can be seen, while the rest of the sample is covered by Au nanoparticles. The z-scale of the colour map used is given, in nm, on the right-hand of the image. STM Scan parameters: V_S = +1.4 V, I_T = 100 pA. Scale bar: 100 nm. Recorded at 300 K.

To create the variable coverage Au/TiO_2 sample, Au nanoparticles were deposited onto a clean TiO_2 sample using a 'tip-shadowing' method. This involved placing the sample into an STM stage prior to dosing. First, the tip of the STM was approached to within tunnelling distance of the sample surface, but held stationary. Then, Au was vapour deposited onto the surface via a well-calibrated in-situ e-beam evaporator. During evaporation, the STM tip acted as a barrier to incoming Au atoms, following a line of sight trajectory, leaving a shadowed area of bare TiO_2 on the surface. After deposition, STM imaging shows a bare TiO_2 surface within the shadowed area, while the rest of the sample is populated by Au nanoparticles. As seen in Fig.5.2, this 'tip-shadow' forms a highly resolved impression of the tip apex, revealing that Au nanoparticles have low lateral mobility after landing on the surface. Due to limitations of optical microscopy, and the impracticality of using other techniques such as SEM or TEM, the exact shape of an STM tip at its apex is not usually known, despite being of critical importance for high resolution imaging. From the impression of the tip left by the shadow dosing method, it is clear the STM tip used for this experiment was bent at the

end forming a 100 nm wide hook, see Fig.5.2. In this tip shadowing method, the Au coverage outside the shadow is directly related to deposition time. By moving the STM tip laterally during deposition, parts of the surface initially within the shadowed area could be exposed to incoming Au vapour, allowing for control of the Au coverage within the initial shadow.

The method of core level spectroscopy (μ-XPS) used in this study collects spatially averaged data from a 2 μm^2 area, while PEEM measurements have a maximum resolution of ~50 nm. To accommodate this limitation, it was necessary to create several discrete regions of Au coverage on the sample, within which the nanoparticle size was uniform. To this end, an Au/TiO_2 sample, with multiple areas of discrete nanoparticle coverage, was created using the tip-shadowing method described above. First, Au was deposited onto the sample to a predetermined coverage with the STM tip approached, creating an initial tip shadow. Then, deposition was halted, and the STM tip was moved 100 μm away from the apex of the shadow, in a direction parallel to the beam of the evaporator. After this, Au deposition was repeated creating a second shadow at the new position of the STM tip. During the second deposition, the total Au coverage outside of the initial tip shadow increased, while a new coverage region was created within the 100 μm distance between the apices of the new and initial tip-shadows. Repeating this process created a precise pattern of Au deposited areas, with incrementally increasing coverage, on the TiO_2 (110) surface. A schematic diagram of this 'multiple tip-shadowing' method is shown in Fig.5.3.

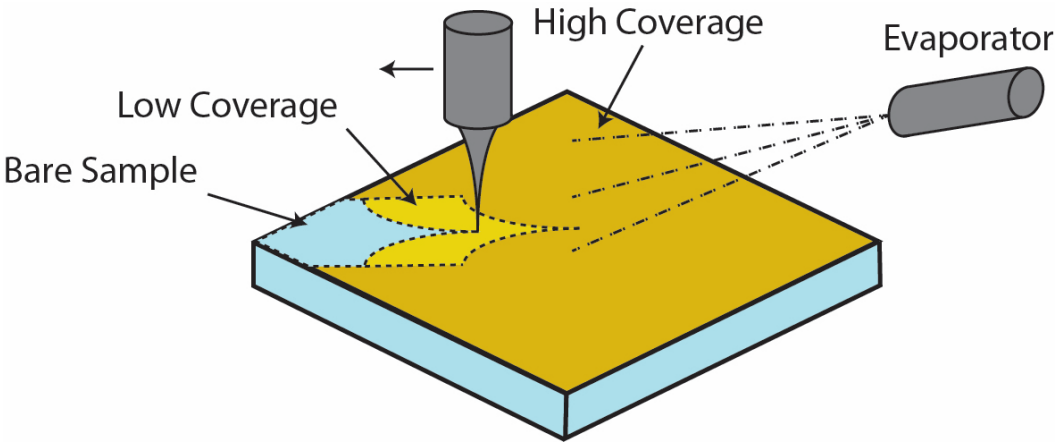

Fig.5.3, schematic diagram of the multi-tip-shadow method used to deposit discrete regions of varying Au coverage onto a single TiO_2 crystal. The motion of the tip between deposition stages is indicated in the diagram. Two tip-shadows are shown, the first (outer) exhibits a lower Au coverage than the non-shadowed area of the sample, while the second (inner) shows the bare substrate.

After deposition, the Au coverage, and particle size, of each area was determined by STM. Fig.5.4 shows a series of STM images taken from five different Au coverage areas. The nanoparticle coverage of each region was determined to be 0.05, 0.10, 0.21, 0.40 and 2.3 MLE for Fig.5.4 a), b), c), d) and e) respectively. At 0.05 MLE Au, the smallest features measured on the surface had an average height and diameter of 172 ± 10 pm and 1.23 ± 0.06 nm, respectively. This corresponds well with measurements of single Au atoms on TiO_2 (110)[45]. Fig.5.4 f) shows a large-scale image of the surface at the border between two tip-shadows. The boundary between different Au coverages is highlighted by a white dotted line in Fig.5.4 f) that runs diagonally down the image from left to right.

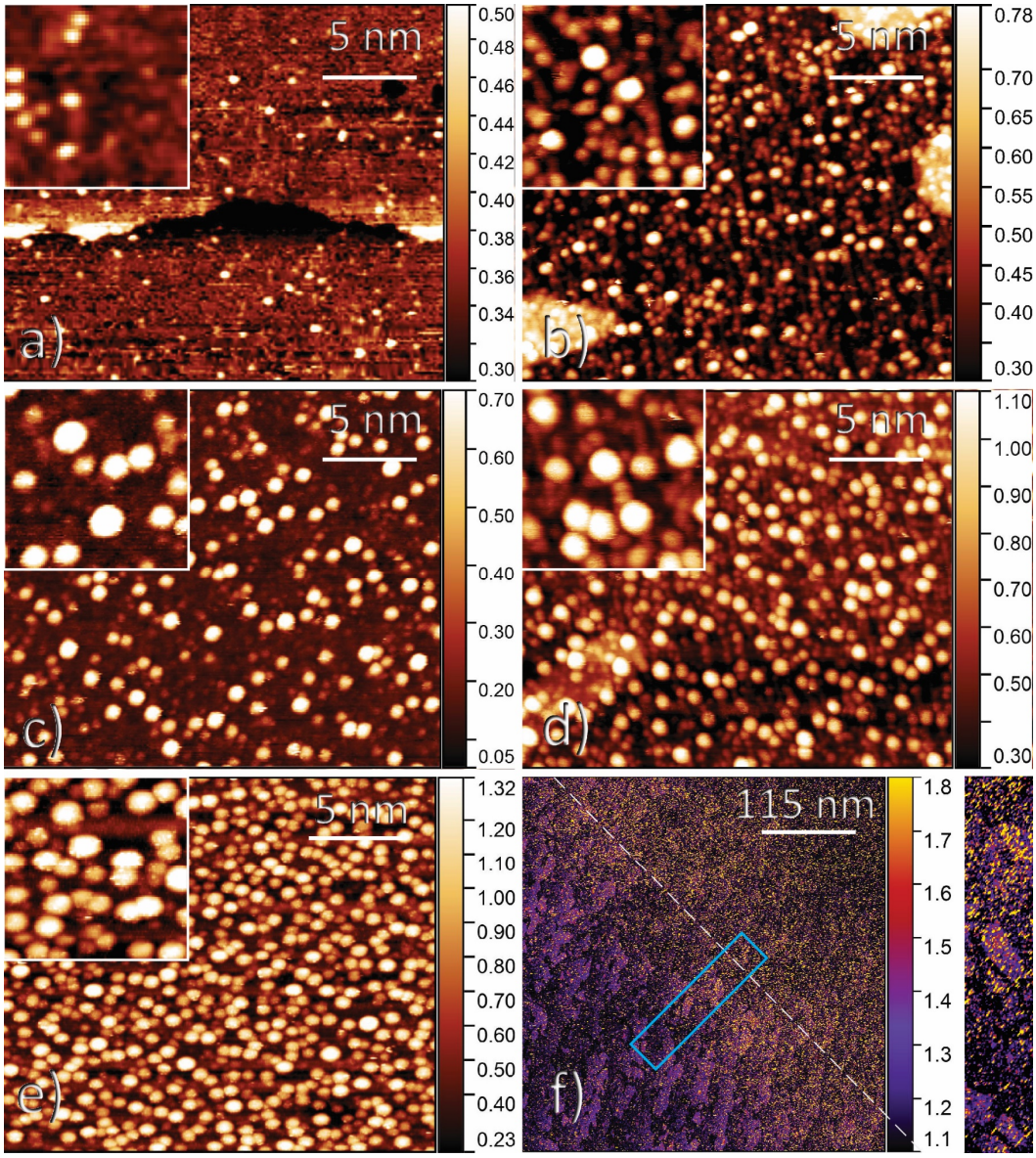

Fig.5.4, series of STM topographs taken from different tip-shadow regions on the Au/TiO_2 surface. The total surface coverage was determined to be 0.05, 0.1, 0.21, 0.34 and 2.3 MLE Au in Fig. 5.4 a), b), c) d) and e) respectively. Insets show 10 nm^2 magnified views of the nanoparticles in each image. Fig. 5.4 f) shows a large-scale image taken at the boundary between two tip-shadows (emphasised by a white dashed line). To make the boundary clearer, a high contrast colour scheme has been applied to f). The z-scale of the colour maps used are given, in nm, on the right-hand side of each image. Scan parameters: V_S = +1.4 V, I_T = 100 pA. Scale bar: a)-e) 5 nm, f) 115 nm. All images were recorded at 300 K.

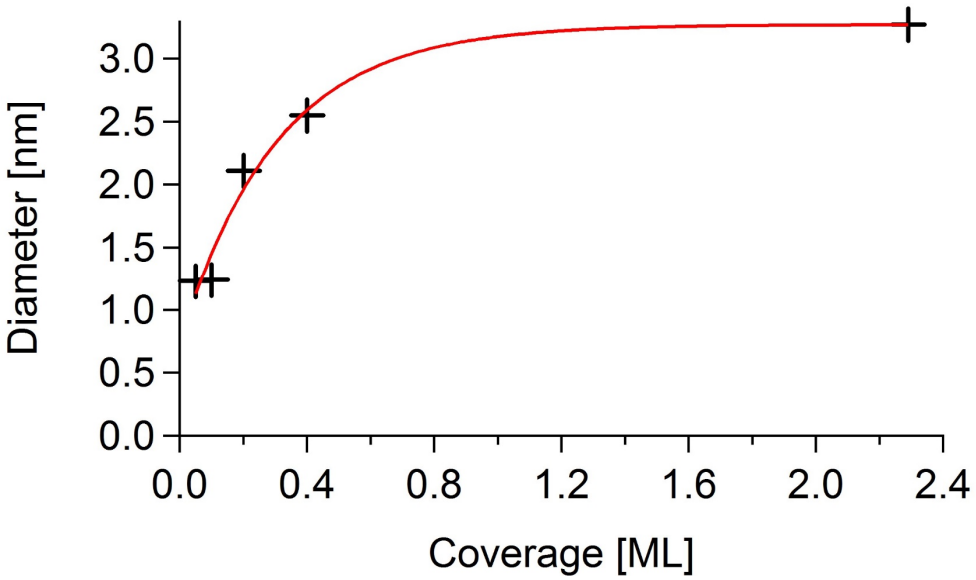

Fig.5.5, graph showing the variation of Au nanoparticle diameter with total Au coverage on the surface of a rutile TiO_2 single crystal. Both nanoparticle diameter and total surface coverage were determined by STM.

Lateral resolution in STM is complicated by the relatively poorly defined shape of the tip apex as features are a convolution of the electronic states of the surface and the tip itself. Using the STM's vertical resolution proves to be more accurate for measuring small nanoparticles. Lai *et al.* have shown that a hemispherical approximation can effectively account for the height-to-diameter ratio of Au nanoparticles supported by TiO_2[46]. In their work, Lai *et al.* give an Au nanoparticle height-to-diameter ratio of ⅓ for Au coverages between 0.1 and 1 MLE. Using this ratio, average (deconvoluted) Au nanoparticle diameters were calculated for each coverage using measured nanoparticle heights. Fig.5.5 shows a plot of nanoparticle diameter as a function of total Au coverage. Due to the hemispherical approximation used, the height-to-diameter ratio used is not expected to remain valid at coverages <0.1 MLE, *i.e.* where single Au atoms are present on the surface. To solve this, a previously determined height-to-diameter ratio of 0.15, taken from rutile TiO_2 deposited with 0.08 MLE Au (see appendix A3), was used to approximate nanoparticle diameters at 0.05 MLE Au. Applying an exponential fit to the data in Fig.5.5 gives a reasonable approximation of the

relationship between Au diameter and coverage. Such an approximation is similar to the method used by Lu et al[47].

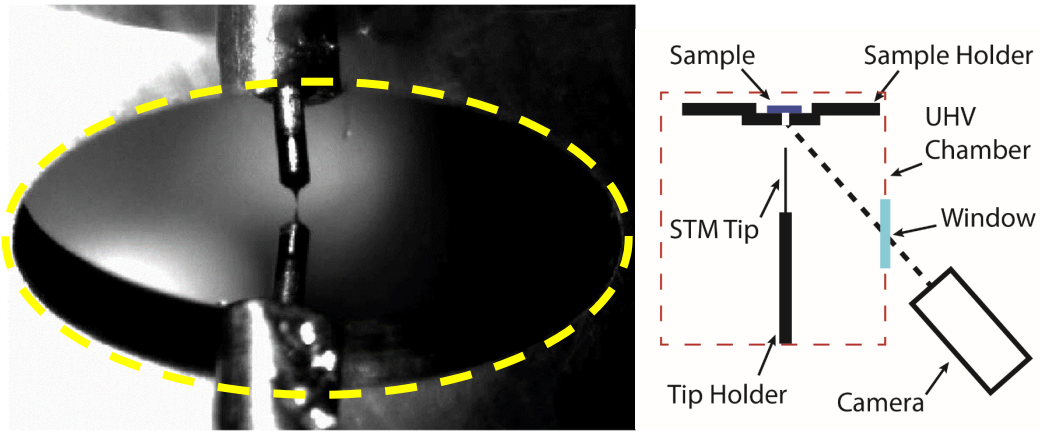

Fig.5.6, (left) photograph taken from the high-resolution CCD camera mounted externally to the STM chamber. In the image the STM tip can be seen extending from the bottom up, while its reflection on the sample can be seen from the top down. The edge of the sample holder has been indicated on the image (yellow dashed circle). (right) Illustration sowing the relative positions of the camera, STM tip and sample.

Au coverages deposited during this experiment were too low to be optically visible. Also, as the 'tip-shadow' area measures only 100 nm at its apex, it was not practically feasible to find it by exploring the entire sample with STM/PEEM. Therefore, the ability to reproducibly locate a common point in both the STM and PEEM apparatus was essential for studying the effects of varying Au coverage via the tip-shadow method. To do this, a special sample (Siemens Star™) was used on which a 500 µm ring marking its exact centre was visible both optically, via the STM CCD camera, and with LEEM. With the Siemens Star™, an absolute set of X and Y coordinates consistent in both PEEM and STM could be defined relative to the sample. To do this, the STM tip was positioned over the centre point of the ring and a high-resolution image was taken using the externally mounted CCD camera. The position of the tip on the captured image, with respect to the sample holder (a common reference point for all samples), was taken as the origin point for coarse movement of the STM tip. Using this image as an overlay on the live CCD camera feed, the STM tip could be reproducibly, and accurately, approached to the exact centre of any sample. An example image taken from the CCD camera, with the STM tip approached, is shown in Fig.5.6

(left). Afterwards, the sample was transferred to the PEEM instrument and the same centre point, as indicated by a small ring visible in UV-PEEM, was located. The exact X and Y coordinates of the centre point were recorded and could be recalled using high precision piezo motors attached to the X/Y manipulation stage of the PEEM instrument. A UV-PEEM image of the Siemens star™ central ring is shown in Fig.5.7.

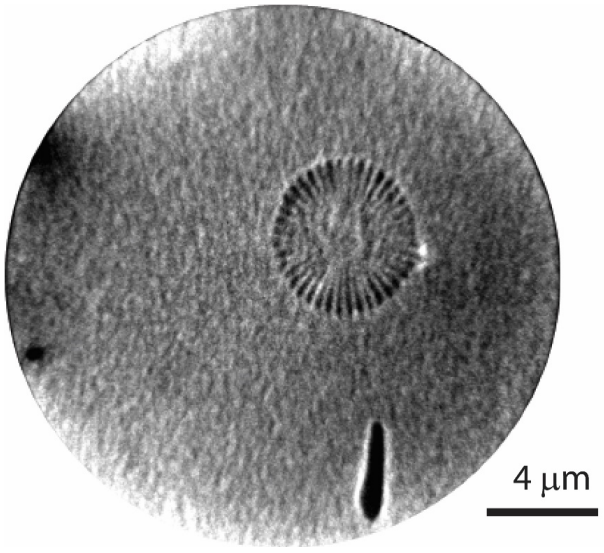

Fig.5.7, PEEM image taken from the Siemens star™ sample showing the central ring feature. Beam energy = -0.34 eV, FOV = 20 μm.

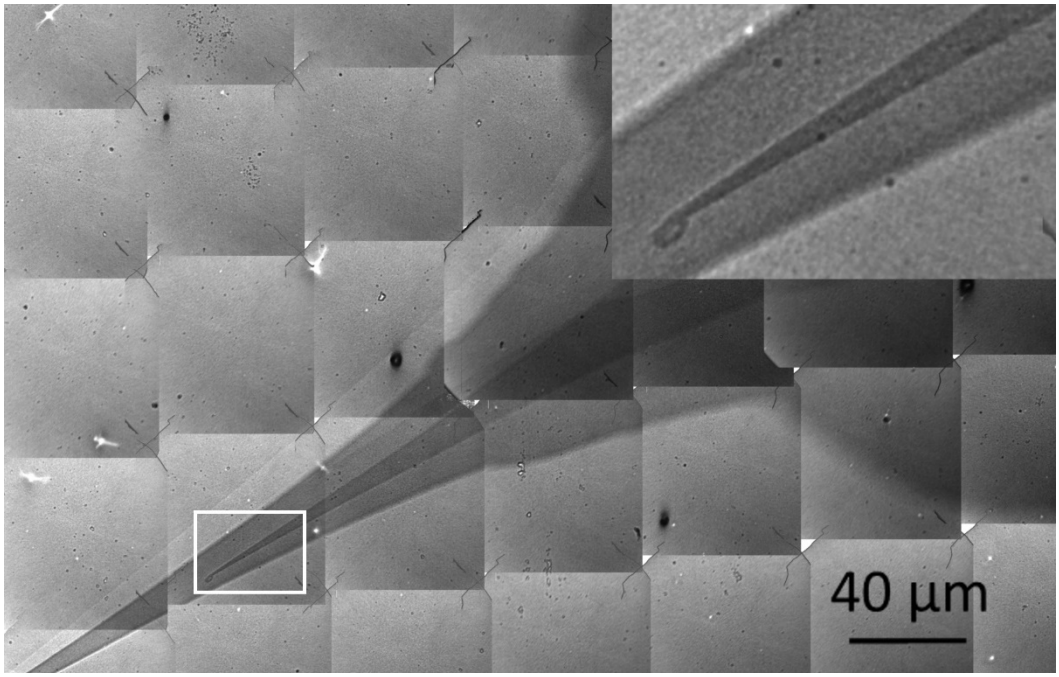

Fig.5.8, a series of digitally stitched UV-PEEM images, taken from the Au/TiO_2 sample, showing a tip shadow extending diagonally down from right to left as an area of darker contrast. Within the first 'outer' shadow a second 'inner' shadow can be seen. The inset image shows a magnified view of the apex of the inner tip shadow. The inner shadow was well enough resolved to leave an impression of the 'hook' at the end of the tip. Image contrast is derived from the local workfunction of the sample. Beam energy = -0.5 eV, FOV = 80 µm per image taken.

After creating the tip-shadowed sample, and defining the position of the shadow's apex in both STM and PEEM, the sample's surface was imaged using UV-PEEM. Fig.5.8 shows a series of digitally stitched UV-PEEM images taken from the Au/TiO_2 sample. In the images, multiple, well defined impressions of the STM tip are seen on the surface that become incrementally darker towards the sample's edge. The edge of each STM tip impression represents the boundary between two Au coverage regions. The change in image contrast can be explained by an increased local workfunction of the surface for areas with higher Au coverage[48]. The inset of Fig.5.8 shows a magnified view of the apex of an STM tip impression. The 'hook' of the tip, as seen previously in STM, is well resolved in PEEM.

5.3.2 | Synchrotron Beam Induced TiO_2 Reduction

To study its electronic characteristics, core level electron spectra were recorded from an Au/TiO_2 sample using µ-XPS, see Fig.5.9 (top). The Ti 3p core level of TiO_2 is well defined in the literature appearing as a single peak centred around 38 eV binding energy[49]; however, initial measurements of the Au/TiO_2 sample show a broad feature between 34-40 eV. Previously, Rödel *et al.* recorded core level spectra from anatase TiO_2, using synchrotron radiation, that show a similar feature between 34 and 40 eV[50]. After running a Gausian peak fitting function (Multi-peak Fitting 2.0, Igor Pro), three distinct features are revealed between 34 and 40 eV; the as expected singlet at 38.01 eV and two other features centred at 35.85 and 34.08 eV. A shift of the Ti 3p peak to lower binding energy is explained by reduction of the Ti^{4+} atoms. While studying oxidation of MgO supported Rh particles, Gregoratti *et al.* observed similar X-ray induced reduction of RhO_2 thin films[51]. Rödel *et al.* suggest that the high intensity photons of the synchrotron reduce surface Ti^{4+} to Ti^{3+} and Ti^{2+}, causing the peaks at approx. 34 and 36 eV respectively[50]. Grinter *et al.* have shown that introduction of an O_2 partial pressure counteracts X-ray induced reduction of CeO_2 thin films[52]. To study the Au/TiO_2 system without the influence of synchrotron induced photo-reduction a similar methodology was applied. After introducing a partial pressure of (10^{-6} mbar) O_2 into the vacuum, during continuous measurement of the sample via µ-XPS, a change in the Ti 3p feature was observed. Most notably, the intensity of the Ti^{4+} peak increases while the Ti^{3+} and Ti^{2+} peaks are reduced. The apparent conversion of Ti^{3+} and Ti^{2+} to Ti^{4+} indicates that the presence of O_2 can counteract photo-induced reduction of the surface. Introducing O_2 during a measurement did not fully re-oxidise the sample, but addition prior to X-ray exposure resulted in a single peak in the Ti 3p spectra at 38 eV (Ti^{4+}), see red line Fig.5.9 (top).

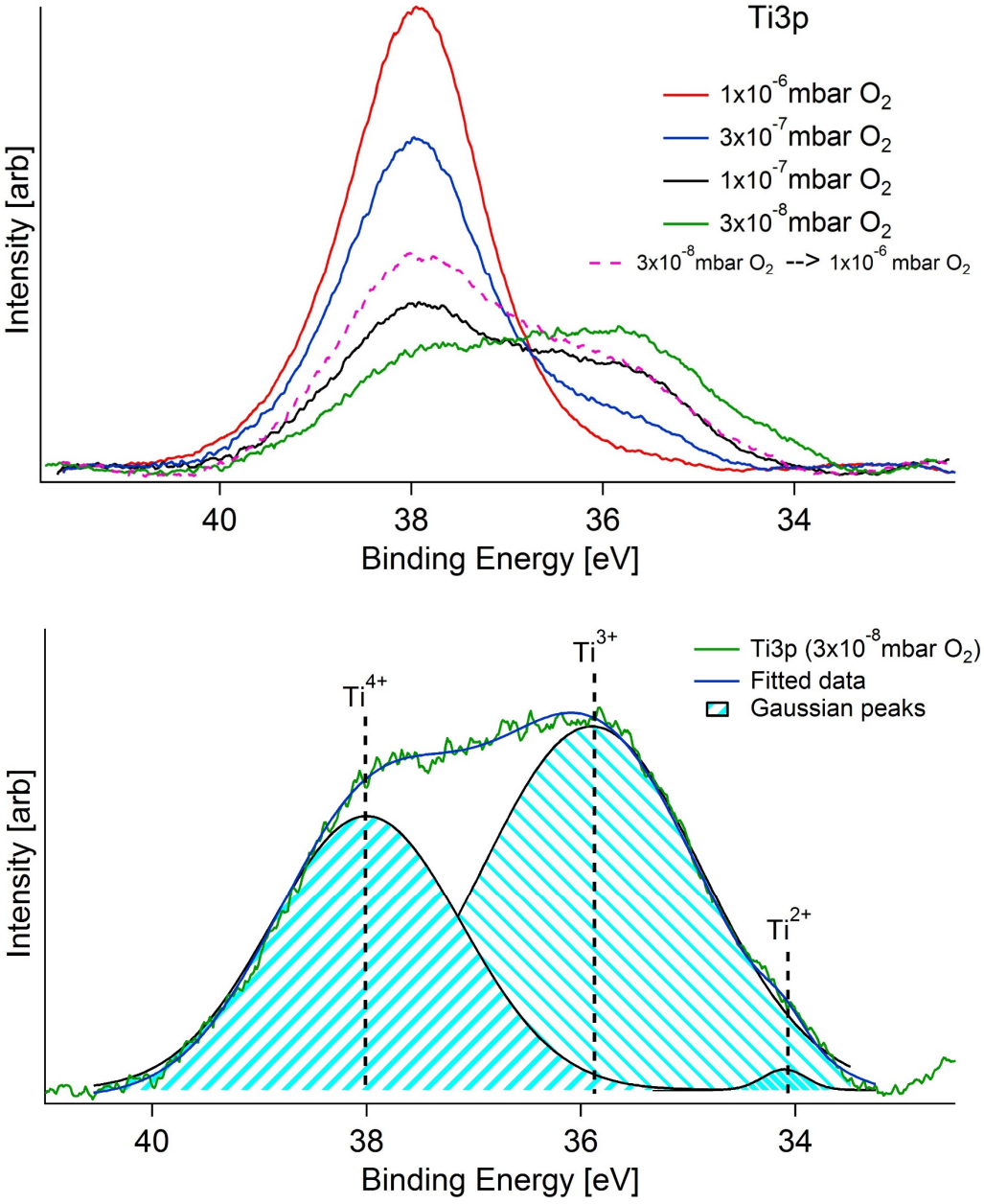

Fig.5.9, (top) background subtracted XPS spectra of the Ti 3p core level taken from an Au/TiO_2 sample. Solid lines represent spectra collected at incrementally lower O_2 partial pressure. The pink dashed line shows the Ti 3p core level after the O_2 partial pressure was reduced to 3×10^{-8} mbar then increased back to 1×10^{-6} mbar. FOV = 8 µm, beam energy = 200 eV. (bottom) Example Ti 3p spectra ($3x10^{-8}$ mbar) showing the results of a Gaussian peak fit, obtained using the Igor Pro Multi-peak fit 2.0 program.

O_2 molecules are known to dissociatively adsorb on reduced rutile TiO_2 (110) at $O_{b\text{-}vacs}$ creating a stoichiometric surface[52]. In this work, Au was vapour deposited onto a reduced rutile surface under UHV conditions prior to both O_2 and X-ray radiation exposure. Au is known to nucleate at surface $O_{b\text{-}vac}$

sites on reduced rutile TiO_2 (110) and is expected to prevent subsequent O_2 dissociation, thereby 'protecting' the $O_{b\text{-}vacs}$ underneath. Therefore, though no Ti^{3+} feature is observed in μXPS spectra taken at 10^{-6} mbar O_2 partial pressure, due to a lack of surface $O_{b\text{-}vacs}$ the substrate is considered to be in an effectively reduced state with respect to the deposited Au nanoparticles.

To better understand the effects of O_2 exposure and X-ray induced photo-reduction, spectra were recorded of the Ti 3p, Au 4f and TiO_2 valence band as a function of O_2 partial pressure.

μ-XPS spectra reveal a strong dependence of the Ti 3p core level on O_2 partial pressure. At 10^{-6} mbar O_2, a typical Ti 3p peak appears with only Ti^{4+} character. As the partial pressure is reduced to 3×10^{-7} mbar O_2 (blue line Fig.5.9 top) the intensity of the Ti^{4+} peak decreases and a Ti^{3+} feature begins to develop. As the O_2 pressure is reduced to 1×10^{-7} mbar (black line Fig.5.9 top) the ratio between Ti^{4+} and Ti^{3+} intensity approaches 1. When the O_2 pressure further decreases to 3×10^{-8} mbar (green line Fig.5.9 top) a Ti^{2+} feature appears and the Ti^{3+} peak intensity surpasses that of the Ti^{4+}. After reducing the O_2 partial pressure to 3×10^{-8} mbar it was again increased back to 10^{-6} mbar (pink line Fig.5.9 top). Rather than a single Ti^{4+} peak, originally seen at this pressure, the Ti 3p spectrum now shows both Ti^{4+} and Ti^{3+} characteristics indicating a level of reduction somewhere between that of the 3×10^{-7} mbar and 1×10^{-7} mbar spectra. From these spectra, photo-reduction of the surface by X-ray photons appears to be irreversible once the O_2 partial pressure falls below a critical value.

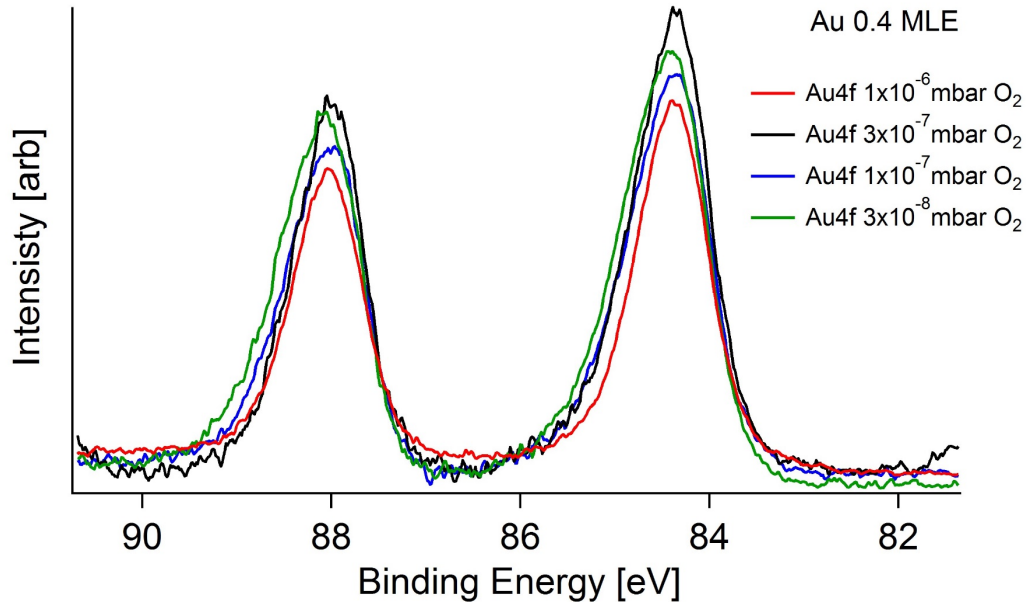

Fig.5.10, background subtracted XPS spectra taken from an Au/TiO_2 sample of the Au 4f core level within a region of 0.4 MLE Au coverage. Spectra were collected as the O_2 partial pressure was decreased. FOV = 8 µm, beam energy = 200 eV.

Fig.5.10 shows Au $4f_{5/2,7/2}$ spectra collected as a function of O_2 partial pressure at 0.4 MLE Au coverage. No change was observed for the Au 4f doublet as a function of O_2 partial pressure, indicating Au nanoparticles are unaffected by photo-induced reduction of the sample. Measurements taken from 0.1, 0.2 and 0.3 MLE Au coverages also show the same trend seen for 0.4 MLE. Previously Grinter *et al.* studied core level spectroscopy of Au nanoparticles supported by CeO_2 thin films using synchrotron radiation[53]. Their data show the Au 4f doublet undergoing a dramatic change as O_2 is removed from the vacuum. For Au deposited on CeO_2 islands, large positive shifts in binding energy are attributed to beam induced formation of an Au-Ce alloy. Over the bare Rh (111) surface, however, no change of the Au 4f core level is observed. This leads to the conclusion that the effects of photo-reduction on Au nanoparticles are highly dependent on the exact nature of the substrate.

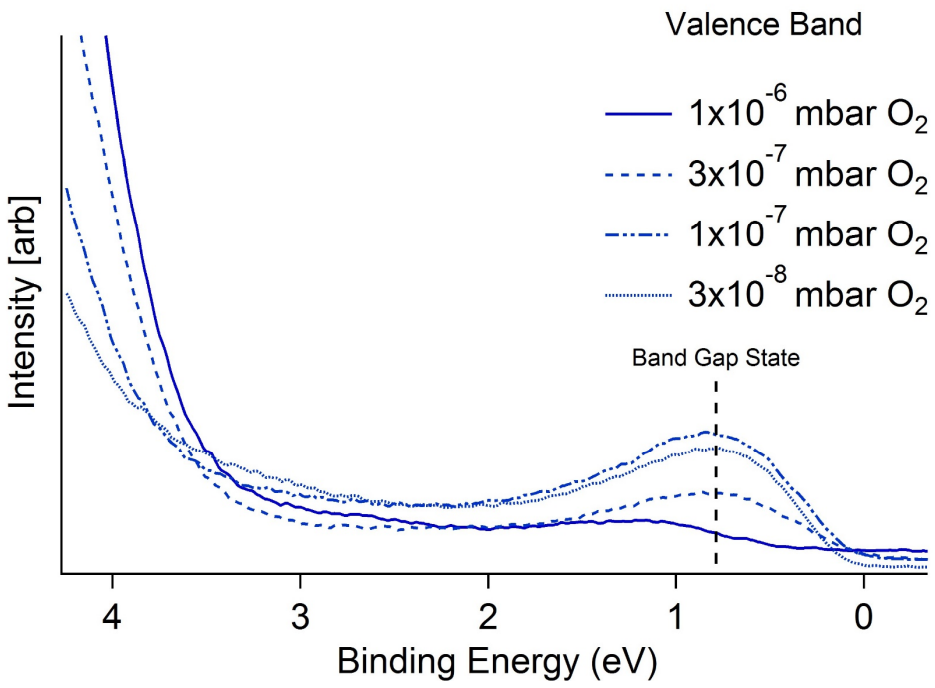

Fig.5.11, background subtracted XPS spectra taken from an Au/TiO_2 sample at the valence band. Spectra were collected as the O_2 partial pressure decreased. The TiO_2 BGS at 0.8 eV below the Fermi energy is indicated in the figure. FOV = 8 µm, beam energy = 200 eV.

Valence band spectra of the Au/TiO_2 sample are shown in Fig.5.11. The TiO_2 BGS, located 0.8 eV below the Fermi energy, was observed to grow as the O_2 partial pressure decreased. Increased BGS intensity is associated with reduction of the sample via generation of Ti^{3+} species. From this observation, it is suggested that exposure to a constant beam of X-ray photons (200 eV) causes O atoms to be removed from the TiO_2 surface, resulting in sample reduction. In the presence of an O_2 partial pressure the BGS remains minimal over time, suggesting that O_2 can counteract photo-induced reduction of TiO_2. Therefore, it is further suggested that a dynamic equilibrium exists between the removal of O from TiO_2 by incident photons and the dissociation of ambient O_2 molecules on the surface to fill the newly generated O vacancies. To avoid any issues caused by photo-induced reduction of the sample, all further measurements were carried out under an O_2 partial pressure of 10^{-6} mbar.

5.3.3 | Coverage Dependent Au 4f Binding Energy Shift

To assess the electron binding energy of Au nanoparticles as a function of their coverage (size) on reduced TiO_2, a series of spectra were collected of the Au 4f core level. Using the multiple tip-shadow method described in the Supplementary Information, a single Au/$TiOf_2$ sample was created with 5 discrete Au coverage regions on its surface ranging from 0.05 to 0.4 MLE. Au coverage regions were located using UV-PEEM, and subsequently highly spatially resolved core level spectra were collected via µ-XPS. Fig.5.12 shows the spectra collected from the sample at 0.05, 0.1, 0.2, 0.3 and 0.4 MLE Au coverage. A spectrum collected from a sample covered by 2.3 MLE Au is also included as an example of Au nanoparticles approaching bulk-like character.

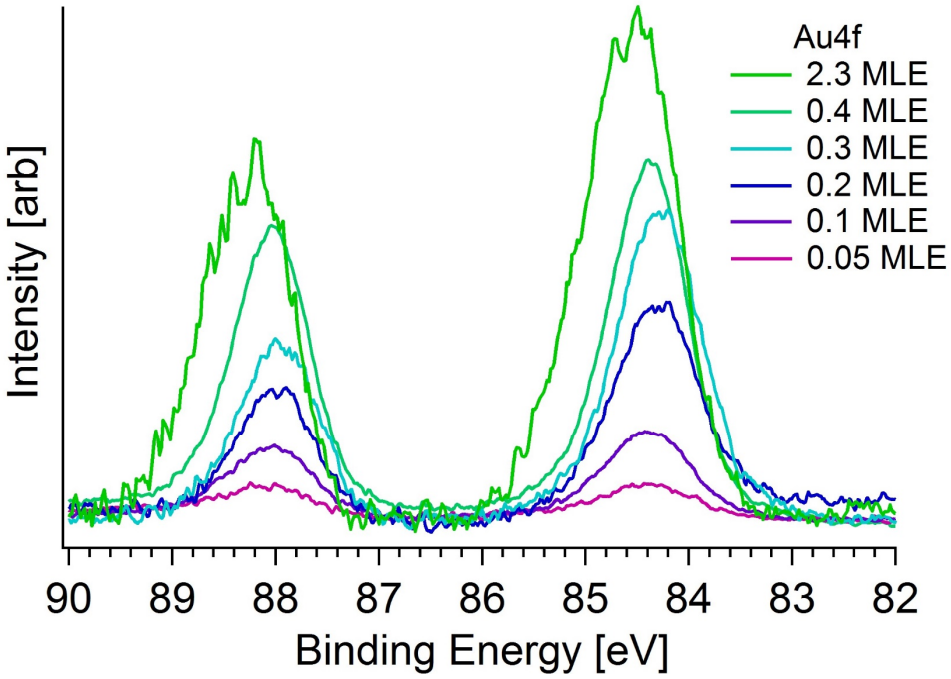

Fig.5.12, background subtracted XPS spectra taken from a multi-tip-shadowed Au/TiO_2 sample of the Au 4f core level. Spectra were taken at Au coverages in the range of 0.05 to 0.4 MLE Au. An additional spectrum collected at 2.3 MLE Au coverage is also shown representing the Au 4f core level in its bulk-like state. FOV = 8 µm, beam energy = 200 eV. All spectra recorded at 1×10^{-6} mbar O_2.

For each coverage, the Au $4f_{7/2}$ binding energy remained constant at all recorded O_2 partial pressures (1×10^{-6}, 3×10^{-7}, 1×10^{-7} and 3×10^{-8} mbar). To

eliminate the effects of sample reduction on the substrate, all spectra were collected at 10^{-6} mbar O_2. The observed trend in Au $4f_{7/2}$ binding energy is plotted in Fig.5.13 and can be separated into two regions. In the first region (0.05-0.3 MLE Au), the Au $4f_{7/2}$ peak shifts to lower binding energy by -109 meV (from 84.42 to 84.31 eV). In the second region (0.3-0.4 MLE Au) the Au $4f_{7/2}$ peak shifts back to higher binding energy by +79 meV (from 84.31 to 84.39 eV).

In contrast to spectra of the reduced surface, measurements of stoichiometric TiO_2 show only a negative shift in Au $4f_{7/2}$ binding energy as Au coverage increases. Such Au $4f_{7/2}$ binding energy shifts have been observed in the literature for various substrates and are determined to arise predominantly from final state effects[15,41,42]. Conversely, the observed positive binding energy shift on reduced TiO_2 for coverages above 0.3 MLE Au is attributed to initial state effects[41,42]. Physically, the main difference between stoichiometric and reduced TiO_2 is the presence of $O_{b\text{-}vacs}$. On the reduced surface, due to the limited number of surface $O_{b\text{-}vac}$ sites, as Au particle size increases so too will the ratio of Au atoms to $O_{b\text{-}vacs}$. In the case of charge transfer from $O_{b\text{-}vacs}$ to Au clusters, this would result in a reduction of the total negative charge per Au atom. As nanoparticles become less negatively charged, the reduced Coulomb repulsion can be expected to result in an increase in core level electron binding energy. In spectra, this would manifest as a positive binding energy shift. It is therefore suggested, the positive Au $4f_{7/2}$ shift observed between 0.3 and 0.4 MLE Au coverage on reduced TiO_2 (110), see Fig.5.13, is caused by an effectively reduced electron transfer from $O_{b\text{-}vacs}$ to Au (per Au atom). As such, this data is presented as evidence of charge transfer from $O_{b\text{-}vacs}$ to Au nanoparticles on reduced TiO_2 (110). It is worth noting that, other initial state effects (*i.e.* increasing ratio of surface-to-bulk atoms) may also contribute to a positive shift in Au $4f_{7/2}$ binding energy, however, this seems unlikely as the same trend is not observed on the stoichiometric surface. Considering initial state effects alone, one would expect a continuously decreasing binding energy shift as particle size increases. However, to explain the

two-region shift seen in Fig.5.13 it is necessary to consider the contributions of both initial and final state effects.

A study of reduced TiO_2 supported Au nanoparticles by Jiang *et al.* shows a similar shift in Au $4f_{7/2}$ binding energy as a function of Au nanoparticle coverage. Using a thickness monitor they estimate the observed positive shift of +70 meV occurs between 0.38 and 0.77 MLE Au[54]. However, by using STM to determine Au coverage directly, the data presented here can be directly linked to Au nanoparticle diameter. To the best of the authors knowledge, the work presented here is the first time core level spectra have been recorded from nanoparticles of varying size on a single sample. Unlike previous studies, such as the work by Jiang *et al.*, this should eliminate any discrepancies that arise due to the variable reduction state of the substrate material.

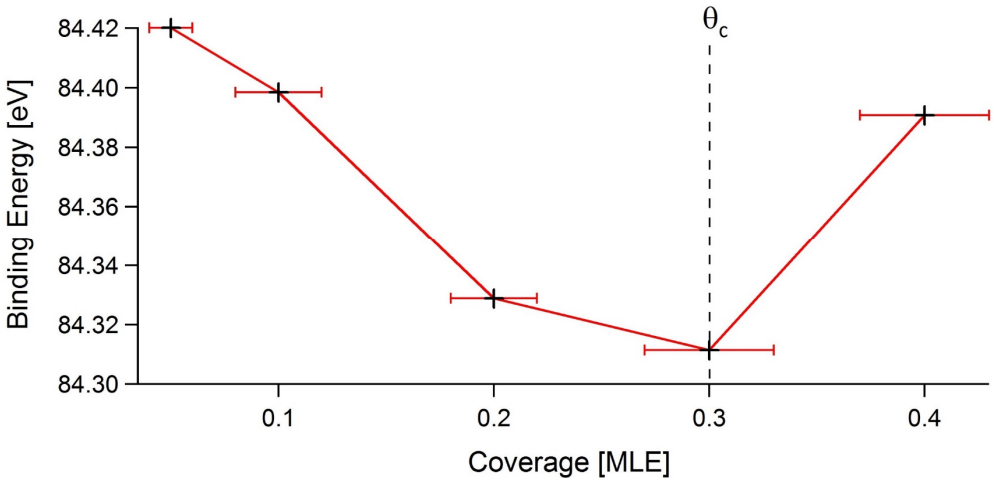

Fig.5.13, plot showing observed Au$4f_{7/2}$ binding energy shifts as a function of nanoparticle coverage, measured from a single, reduced Au/TiO_2 sample. The initial binding energy decrease, between 0.05 to 0.3 MLE, is followed by an increase as coverage further increases to 0.4 MLE.

The appearance of both negative and positive binding energy shifts, as Au particle size increases, can be explained by an interplay between initial and final state effects. From the work presented here, a critical coverage is suggested, θ_c, at 0.3 MLE. The initial negative shift in binding energy, observed as Au coverage increases, is an expected consequence of the increasing particle size due the diminishing influence of final state effects. At θ_c the influence of charge transfer

on the Au nanoparticles becomes more significant than final state effects. As Au coverage continues to rise the total negative charge transferred per Au atom decreases causing the positive shift in binding energy towards a bulk-like value. θ_c therefore, represents a threshold above which charge transfer from the substrate significantly contributes to the electronic character of Au nanoparticles. Using the relationship for nanoparticle diameter and Au coverage (Fig.5.5), the average diameter of Au nanoparticles for the 0.3 MLE Au region is determined to be 2.32 (±0.45) nm. This coincides well with previous studies that show a peak in catalytic activity occurs for Au nanoparticles somewhere between 2.0 and 3.0 nm in diameter[38,55,56]. These observations suggest that charge transfer may play a critical role in the size specific catalytic activity of TiO_2 supported Au nanoparticles. By collecting all spectra from a single sample, inconsistencies arising from variable sample reduction/morphology have been eliminated. Also, utilising STM has allowed for precise measurement of Au coverage and nanoparticle diameter for each region on the sample.

Using the previously determined coverage-to-diameter relationship, the +79 meV BE shift observed between 0.3 to 0.4 MLE Au can be correlated with an increase in nanoparticle diameter from 2.31 (±0.45) to 2.55 (±0.43) nm. Applying the same hemispherical approximation parameters mentioned above, these measurements were used to calculate the average volume of Au nanoparticles at coverages of 0.3 and 0.4 MLE. For Au (111) the volume and number of atoms per unit cell is known to be 0.068 nm^3 and 4 respectively. From this, the approximate number of Au atoms per nanoparticle at 0.3 and 0.4 MLE coverage was estimated to be 64 and 85 respectively. Though the clean TiO_2 sample used in this work was analysed by STM prior to Au deposition, the image resolution obtained was not sufficient to allow direct determination of the surface's $O_{b\ vac}$ density. The typical density of O_b vacs on rutile TiO_2, prepared via conventional sputter/anneal cycles, is reportedly between 5 and 10% (where 100% is the total number of surface O_b sites). Using an estimate of the O_b vac density on the sample's surface the approximate number of O_b vacs per Au atom can be calculated for all Au

coverages. The number of O_b vacs per Au atom for nanoparticles within all measured Au coverage regions were calculated for O_b vac densities of 5, 8 and 10% (see Table 1.)

Au Coverage (MLE)	Au atoms per Cluster	O_b vacs per Au (5%)	O_b vacs per Au (8%)	O_b vacs per Au (10%)
0.05	9	0.124	0.198	0.248
0.1	10	0.123	0.197	0.246
0.2	48	0.072	0.116	0.145
0.3	64	0.066	0.105	0.132
0.4	85	0.060	0.096	0.120

From the data in Table 1, the ratio of O_b vacs to Au atoms decreases as Au coverage increases. This trend becomes more pronounced as the density of O_b vacs on the sample surface increases. As such, this data is in line with the observed positive binding energy shift seen between 0.3 and 0.4 MLE Au, however, the change O_b vac/Au atom ratio between these coverages is much smaller than one might expect for the magnitude of this shift (+70 meV). An O_b vac density greater than 10% would give rise to a larger change in O_b vac/Au atom ratio, however this seems unlikely. By artificially increasing the reduction state of a rutile TiO_2 sample, Yim *et al*. have shown that pit-like features begin to form on the (110) surface as the density of O_b vacs increases from ~5 to ~10 %[19]. As no such features were observed in this work an O_b vac density greater than 10% is ruled out. From the literature, the unexpectedly large shift in Au $4f_{7/2}$ binding energy could be explained by a sudden change in Au nanoparticle morphology as coverage increases above 0.3 MLE (*i.e.* a change in nanoparticle height-to-diameter ratio)[11]. Though no evidence of a change in Au morphology was observed by STM it is possible that higher resolution imaging is necessary to observe such a transition. The Au 4f positive BE shift seen in Fig.5.13 may also be accounted for by considering the depletion/accumulation of electrons between at the nanoparticle/substrate interface following charge transfer. Using DFT,

Matthey *et al.* have indicated that very small Au nanoparticles experience a charge polarisation effect (analogous to an image charge) upon adsorption at O_b vac on reduced TiO_2 (110)[45]. They show that, while O_b vac sites become positively polarised, due to electron density depletion, Au atoms become slightly negatively polarised. This effect is strongest for Au atoms directly bonded to vacancy sites (+0.1 e^-/Å) and reduces in magnitude radially throughout the nanoparticle. From this, one would expect such polarisation of the Au nanoparticles to induce a negative shift in Au 4f BE, which is most significant for single Au atoms and decreases as a function of Au particle size. While this effect would have a relatively small impact on Au 4f BE compared to complete charge transfer, the combination of both phenomena may explain the unexpectedly large positive BE shift observed.

5.4 | Summary and Conclusions

The electronic characteristics of Au nanoparticles, supported by reduced TiO_2, have been explored. Inconsistencies arising from the variable reduction state of TiO_2 samples have necessitated a novel method of sample preparation. The developed STM 'tip-shadowing' method allows for nanopatterning a single TiO_2 sample with discrete regions of selected Au coverage. Additionally, STM was used to determine the relationship between nanoparticle size to Au coverage for each of these regions.

µXPS was utilised to measure core level spectra of the Au/TiO_2 system. Ti 3p measurements from the sample reveal a significant 'beam damage' effect during exposure to the high intensity photons of the synchrotron. The dynamics of this effect were explored in more detail. It was found that X-ray induced reduction of the sample could be counteracted by introducing O_2 into the instrument. Au 4f core level spectroscopy showed a two stage shift in binding energy as nanoparticle coverage decreased. Further analysis of the binding energy shift yielded evidence of charge transfer from $O_{b\text{-}vacs}$ to Au nanoparticles for Au/TiO_2, resulting in negatively charged Au species. The electronic character of Au nanoparticles appears to be dominated by charge transfer effects between 0.3 and 0.4 MLE Au coverage. Below 0.3 MLE final state effects have a more significant influence over Au electronic properties, while above 0.4 MLE, Au exhibits bulk-like characteristics. These values coincide well with published data for a peak in Au nanoparticle activity. The observed binding energy shifts suggest an interplay between the particle size effects and charge transfer may be a likely cause of the highly size dependent nature of Au nanoparticle catalytic activity. The binding energy shift observed between 0.3 and 0.4 MLE Au is larger than expected given the relatively small change in nanoparticle size, however, this may be accounted for by a change in nanoparticle morphology. Further investigation is required to explore this issue further.

5.5 | References

1. Rodriguez, J. A. Gold-based catalysts for the water-gas shift reaction: Active sites and reaction mechanism. *Catal. Today* **160,** 3–10 (2011).

2. Liu, X. Y., Wang, A., Zhang, T. & Mou, C. Y. Catalysis by gold: New insights into the support effect. *Nano Today* **8,** 403–416 (2013).

3. Grunwaldt, J. & Baiker, A. Gold / Titania Interfaces and Their Role in Carbon Monoxide Oxidation. 1002–1012 (1999).

4. Haruta, M. Size- and support-dependency in the catalysis of gold. **861,** (1997).

5. Wong, G. & Vohs, J. An XPS study of the growth and electronic structure of vanadia films supported on CeO_2(111). *Surf. Sci.* **498,** 266–274 (2002).

6. Piao, H. & McIntyre, N. S. High-resolution valence band XPS studies of thin film Au-Al alloys. *J. Electron Spectros. Relat. Phenomena* **119,** 29–33 (2001).

7. Göpel, W. *et al.* Surface defects of TiO_2(110): A combined XPS, XAES and ELS study. *Surf. Sci.* **139,** 333–346 (1984).

8. Kruse, N. & Chenakin, S. XPS characterization of Au/TiO_2 catalysts: Binding energy assessment and irradiation effects. *Appl. Catal. A Gen.* **391,** 367–376 (2011).

9. Farmer, J. Ag Adsorption on Reduced CeO_2 (111) Thin Films. *J. Phys. Chem. C* **2,** 17166–17172 (2010).

10. Liao, X., Chu, W., Dai, X. & Pitchon, V. Bimetallic Au-Cu supported on ceria for PROX reaction: Effects of Cu/Au atomic ratios and thermal pretreatments. *Appl. Catal. B Environ.* **142–143,** 25–37 (2013).

11. Radnik, J., Mohr, C. & Claus, P. On the origin of binding energy shifts of core levels of supported gold nanoparticles and dependence of pretreatment and material synthesis. *Phys. Chem. Chem. Phys.* **5,** 172–177

(2003).

12. Bugyi, L., Berkó, A., Óvári, L., Kiss, A. M. & Kiss, J. Enhanced dispersion and stability of gold nanoparticles on stoichiometric and reduced TiO_2(110) surface in the presence of molybdenum. *Surf. Sci.* **602,** 1650–1658 (2008).

13. Rodriguez, J. A. *et al.* High water-gas shift activity in TiO_2(110) supported Cu and Au nanoparticles: role of the oxide and metal particle size. *J. Phys. Chem. C* **113,** 7364–7370 (2009).

14. Starr, D. E., Shaikhutdinov, S. K. & Freund, H. J. Gold supported on oxide surfaces: environmental effects as studied by STM. *Top. Catal.* **36,** 33–41 (2005).

15. Meyer, R., Lemire, C., Shaikhutdinov, S. K. & Freund, H.-J. Surface chemistry of catalysis by gold. *Gold Bull.* **37,** 72–124 (2004).

16. Pang, C. L., Lindsay, R. & Thornton, G. Structure of clean and adsorbate-covered single-crystal rutile TiO_2 surfaces. *Chem. Rev.* **113,** 3887–3948 (2013).

17. Diebold, U. Structure and properties of TiO_2 surfaces: A brief review. *Appl. Phys. A Mater. Sci. Process.* **76,** 681–687 (2003).

18. Rønnau, A. A Closer Look at the TiO_2(110) Surface with STM. *Adsorpt. J. Int. Adsorpt. Soc.* **2,** 103 (2003).

19. Yim, C. M., Pang, C. L. & Thornton, G. Oxygen vacancy origin of the surface band-gap state of TiO_2(110). *Phys. Rev. Lett.* **104,** 36806 (2010).

20. Diebold, U. The Surface Science of Titanium Dioxide. *Appl. Surf. Sci.* **48,** 53–229 (2003).

21. Pang, C. L., Lindsay, R. & Thornton, G. Structure of clean and adsorbate-covered single-crystal rutile TiO_2 surfaces. *Chem. Rev.* **113,** 3887–3948 (2013).

22. Pang, C. L., Lindsay, R. & Thornton, G. Chemical reactions on rutile TiO_2(110). *Chem. Soc. Rev.* **37,** 2328–2353 (2008).

23. Papageorgiou, A. C. *et al.* Electron traps and their effect on the surface chemistry of TiO_2(110). *Proc. Natl. Acad. Sci. U. S. A.* **107,** 2391–6 (2010).

24. Minato, T. *et al.* Investigation of the electronic interaction between TiO_2(110) surfaces and Au clusters by PES and STM. *Surf. Sci.* **566–568,** 1012–1017 (2004).

25. Yim, C. M. *et al.* Engineering Polarons at a Metal Oxide Surface. *Phys. Rev. Lett.* **117,** 116402 (2016).

26. Minato, T. *et al.* The electronic structure of oxygen atom vacancy and hydroxyl impurity defects on titanium dioxide (110) surface. *J. Chem. Phys.* **130,** 124502 (2009).

27. Okazaki, K., Ichikawa, S., Maeda, Y., Haruta, M. & Kohyama, M. Electronic structures of Au supported on TiO_2. *Appl. Catal. A Gen.* **291,** 45–54 (2005).

28. Lopez, N. & Nørskov, J. Theoretical study of the Au/TiO_2 interface. *Surf. Sci.* **515,** 175–186 (2002).

29. Wörz, A. S., Heiz, U., Cinquini, F. & Pacchioni, G. Charging of Au atoms on TiO_2 thin films from CO vibrational spectroscopy and DFT calculations. *J. Phys. Chem. B* **109,** 18418–18426 (2005).

30. Okazawa, T., Kohyama, M. & Kido, Y. Electronic properties of Au nano-particles supported on stoichiometric and reduced TiO_2(110) substrates. *Surf. Sci.* **600,** 4430–4437 (2006).

31. Jing Chung, H., Yurtsever, A., Sugimoto, Y., Abe, M. & Morita, S. Kelvin probe force microscopy characterization of TiO_2(110)-supported Au clusters. *Appl. Phys. Lett.* **99,** 123102 (2011).

32. Lira, E. *et al.* Growth of Ag and Au Nanoparticles on Reduced and Oxidized Rutile TiO_2(110) Surfaces. *Top. Catal.* **56,** 1460–1476 (2013).

33. Guo, Q., Luo, L., Davis, K. A. & Goodman, D. W. Initial growth of Au on oxides. in *Surface and Interface Analysis* **32,** 161–165 (2001).

34. Cordes, O. & Harsdorff, M. Investigation of gold clusters with

photoelectron spectroscopy. *Appl. Surf. Sci.* **33–34,** 152–159 (1988).

35. Roulet, H., Mariot, J.-M., Dufour, G. & Hague, C. F. Size dependence of the valence bands in gold clusters. *J. Phys. F Met. Phys.* **10,** 1025–1030 (2000).

36. Costanzo, E. *et al.* Initial and final state effects in photoemission from gold clusters. *Solid State Commun.* **81,** 155–158 (1992).

37. Dalacu, D., Klemberg-Sapieha, J. E. & Martinu, L. Substrate and morphology effects on photoemission from core-levels in gold clusters. *Surf. Sci.* **472,** 33–40 (2001).

38. Valden, M., Lai, X. & Goodman, D. W. Onset of Catalytic Activity of Gold Clusters on Titania with the Appearance of Nonmetallic Properties. *Science* **281,** 1647–1650 (1998).

39. Citrin, P. H. & Wertheim, G. K. Photoemission from surface-atom core levels, surface densities of states, and metal-atom clusters: A unified picture. *Phys. Rev. B* **27,** 3176–3200 (1983).

40. Baumer, M. & Freund, H.-J. Metal deposits on well-ordered oxide films. *Prog. Surf. Sci.* **61,** 127–198 (1999).

41. Roberts, F. S., Anderson, S. L., Reber, A. C. & Khanna, S. N. Initial and Final State Effects in the Ultraviolet and X-ray Photoelectron Spectroscopy (UPS and XPS) of Size-Selected Pd_n Clusters Supported on TiO_2(110) *J. Phys. Chem. C*, **119,** 6033-6046 (2015).

42. Henry, C. R., Surface studies of supported model catalysts. *Surf. Sci. Rep.* **31,** 231-325 (1998)

43. Mason, M. G. Electronic structure of supported small metal clusters. *Phys. Rev. B* **27,** 748–762 (1983).

44. Liang, K. & Salaneck, W. X-ray photoemission studies of thin gold films. *Solid State Commun.* **19,** 0–5 (1976).

45. Matthey, D. *et al.* Enhanced Bonding of Gold Nanoparticles on Oxidized TiO_2(110). *Science* **315,** 1692 (2007).

46. Lai, X., Clair, T. P. S., Valden, M. & Goodman, D. W. Scanning tunneling microscopy studies of metal clusters supported on TiO_2(110): Morphology and electronic structure. *Prog. Surf. Sci.* **59,** 25–52 (1998).

47. Lu, J. L., Gao, H. J., Shaikhutdinov, S. & Freund, H. J. Gold supported on well-ordered ceria films: Nucleation, growth and morphology in CO oxidation reaction. *Catal. Letters* **114,** 8–16 (2007).

48. Dover, C. Synchrotron Studies of Technologically Important Metal Oxide Surfaces. (University College London, 2014).

49. Espinos, J. P. *et al.* Synchrotron photoemission characterization of TiO_2 supported on SiO_2. *Langmuir* **14,** 4908–4914 (1998).

50. Rödel, T. C. *et al.* Engineering two-dimensional electron gases at the (001) and (101) surfaces of TiO_2 anatase using light. *Phys. Rev. B - Condens. Matter Mater. Phys.* **92,** 1–11 (2015).

51. Gregoratti, L., Mentes, T. O., Locatelli, A. & Kiskinova, M. Beam-induced effects in soft X-ray photoelectron eission microscopy experiments. *J. Electron. Spectrosc. Relat. Phenom.* **170**, 13-18 (2009).

52. Pan, J. -M., Maschhoff, B. L., Diebold, U. & Madey, T. E. Interaction of water, oxygen, and hydrogen with TiO_2 (110) surfaces having different defect densities. *J. Vac. Sci. Technol.* **10,** 2470-2476 (1992).

53. Grinter, D. C. *et al.* Oxidation state imaging of ceria island growth on Re(0001). *J. Phys. Chem. C* **117,** 16509–16514 (2013).

54. Jiang, Z. *et al.* Direct XPS evidence for charge transfer from a reduced rutile TiO_2(110) surface to Au clusters. *J. Phys. Chem. C* **111,** 12434–12439 (2007).

55. Yu, X. *et al.* Synchrotron-Radiation Photoemission Study of Growth and Stability of Au Clusters on Rutile TiO_2(110)-1X1. *Chinese J. Chem. Phys.* **22,** 339–345 (2009).

56. Haruta, M., Kobayashi, T., Sano, H. & Yamada, N. Novel Gold Catalysts for

the Oxidation of Carbon Monoxide at a Temperature far Below 0 °C. *Chem. Lett.* **16,** 405–408 (1987).

Chapter 6

Probing the Effect Au Nanoparticles Have on the Interactions between Ethanol and Rutile TiO_2 (110)

Outline

Acetate is an important intermediate in many industrial processes, most notably the production of monomers such as vinyl acetate and acetic anhydride. Methanol carbonylation has been the most widely used process for acetic acid production since the late 1980s[1,2]. Despite the inherently low production costs involved, there are several drawbacks to methanol carbonylation, particularly the use of fossil fuels as a source of CO[3]. Due to growing concern over the environmental impact of the chemical industry, interest in developing reliable, 'green' alternatives to reactions like methanol carbonylation has risen in recent years. An alternative method of acetic acid production is via ethylene oxidation.

Though this method is more environmentally friendly than methanol carbonylation it still relies on fossil fuels as a source of ethylene[4]. In addition, ethylene oxidation is not a widely-employed method of acetic acid production in industry, largely due to the cost of obtaining ethylene itself, however this may change with the increasing availability of shale gas. Au nanoparticles supported by reducible metal oxides have been shown to exhibit high activity towards many organic reactions including oxidation[5,6]. A recent study by Green *et al.* has shown that, TiO_2 supported Au nanoparticles facilitate acetate formation via partial oxidation of ethylene[7]. Similarly, the work herein presents evidence of acetate formation over a TiO_2 (110) single crystal surface, modified with Au nanoparticles, following ethanol exposure. As an increasingly available, renewable resource, there are many advantages to using ethanol over ethylene or fossil fuels as a reaction feedstock. In our experiment, HREELS was used to record surface vibrational spectra from a rutile TiO_2 (110) single crystal sample after successively depositing Au nanoparticles and exposing its surface to ethanol. Combining STM, AES and HREELS, an estimate of nanoparticle coverage was determined. The Au coverage was found to be a critical factor for ethanol oxidation. Further to this, the photocatalytic properties of Au/TiO_2 were explored by monitoring the effects of UV exposure. The HREELS spectrum of acetic acid adsorbed on TiO_2 (110) is presented for comparison.

6.1 | Introduction

Developing our understanding of the processes occurring at the surfaces of heterogeneous catalysts is of great importance in both commercial and environmental research. TiO_2 is one of the most versatile, abundant and widely used materials in the world. TiO_2, and its derivatives, have shown marked catalytic

activity towards many organic reaction processes including hydrogen production[8–11]. Interactions between surface adsorbates and photo-induced electron-hole pairs (excitons) are essential to the activity of heterogeneous photo-catalysts such as TiO_2. The rate at which these electron-hole pairs recombine is a critical factor in catalysis. Typically, electron-hole pair recombination rates for TiO_2 are much faster than the electron transfer kinetics associated with chemical reactions. Therefore, to maximise the photo-catalytic activity of a material it is necessary to increase the lifetime of excitons on its surface[9,12]. For TiO_2, exciton lifetimes are influenced by a number of factors, most notably its polymorphic nature[13,14]. By following the reactions of adsorbates on different TiO_2 polymorphs one can develop a detailed understanding of how TiO_2's catalytic properties may be tuned to suit different applications.

Depositing transition metals (M) onto TiO_2 has been shown to further increase exciton lifetimes on the surface if the workfunction of the deposited metal is greater than that of the substrate. This creates a rectifying Schottky barrier between the metal and semiconductor surface thereby reducing the rate of electron-hole pair recombination. This effect is critically dependent on the size of the metal nanoparticles on the surface. For example, noble metal enhancement is known to improve the catalytic activity of TiO_2 towards reactions such as CO oxidation for a given particle size range[5,15–18].

In addition to increasing exciton lifetimes, it has been suggested that TiO_2 supported Au nanoparticles have a plasmon resonance response that facilitates visible light adsorption, further enhancing photo-catalytic activity[19]. Recently, considerable interest has gone into research of Au/TiO_2 heterogeneous catalysis, due in part to its role in 'green' H_2 and syngas production[8,20,21]. Of particular interest are the reactions of alcohols over Au/TiO_2 based catalysts. The use of simple alcohols as a reaction feedstock shows promise for alternative routes of organic synthesis[22–26]. Ethanol in particular has demonstrated the ability to undergo a range of catalytically induced reactions over TIO_2, including

dehydration, dehydrogenation, condensation, decomposition, oxidation and coupling reactions[27].

The acetate anion is an important chemical intermediate for the many organic syntheses. Over 12 million metric tons of acetic acid are consumed annually (as of 2014) for which the largest use is the production of polymer precursors such as vinyl acetate and acetic anhydride[1,2,28]. Currently, carbonylation of methanol is the dominant process for acetic acid production in the world[3]:

$$CH_3OH + CO \rightarrow CH_3COOH. \quad (6.1.1)$$

The main source of CO required in this reaction is obtained by steam reforming of fossil fuels. Therefore, with the rise of green chemistry the development of viable alternatives to reactions such as (1) has become a popular area of interest in recent years. A further complication of (1) is the difficulty involved in separating acetic acid from the reaction mixture[7]. Though several alternative methods of acetic acid production have been explored few have been adopted, largely due to high production costs. One process that has shown great promise as an alternative to CO methylation is direct oxidation of ethylene to acetic acid. In 1980, Seoane *et al.* demonstrated palladium metal catalysts enhance ethylene oxidation at temperatures as low as 500 K, and following their publication, Showa Denco patented the use of palladium for acetic acid production in 1997[4,29]. The main factor hindering ethylene oxidation as a viable replacement for CO methylation is the relative cost of obtaining ethylene itself, though this is set to change with the increasing availability of shale gas[28].

From the recent literature, it seems Au/TiO_2 could be a promising candidate for improving the viability of acetic acid production via oxidation. Green *et al.* have used FTIR measurements to evidence conversion of ethylene to acetate over a rutile Au/TiO_2 powder catalyst[7]. Studies of ethanol exposed TiO_2 evidence the presence of surface adsorbed ethoxide. Upon heating the ethanol

exposed TiO_2 substrate to ~600 K, ethylene desorbs from the surface via a β-hydride elimination process[30]. Idriss *et al.* have published several papers concerning the reactions of ethanol with TiO_2 powder catalysts[8,12,21,27,31]. Following ethanol exposure, they find the main surface species present on a Au modified anatase TiO_2 surface is ethoxide. However, the presence of Au alters the surface reactivity of the substrate at high temperatures, and benzene is observed as the main reaction product at 600 K[27]. Clearly the addition of Au nanoparticles can be a useful tool for tuning the reaction chemistry of TiO_2.

The work presented in this chapter explores the effect Au nanoparticles have on the reactions of ethanol over a rutile TiO_2 (110) single crystal. For this, surface sensitive vibrational spectroscopy has been employed, specifically HREELS. Following ethanol exposure, acetate is found to be the main surface adsorbate formed upon reaction over Au/TiO_2 (110). In addition, the effect of nanoparticle size/coverage has been investigated and found to be of critical importance for conversion of ethanol to acetate. Samples were also exposed to UV radiation in an attempt to explore the photo-catalytic potential of Au/TiO_2. The HREELS spectrum of acetic acid, adsorbed on TiO_2, was measured to provide a reference for acetate determination. To the best of the authors knowledge, this is the first time the HREELS vibrational spectrum of acetic acid adsorbed on single crystal rutile TiO_2 (110) has been presented.

6.2 | Experimental Procedure

HREELS experiments were carried out at room temperature using a VSW HREELS system housed in a UHV chamber with a base pressure of 3×10^{-10} mbar (see Chapter 3). The HREELS chamber was equipped with an ion sputter gun, sample heater, quadrupole mass spectrometer and facilities for AES and LEED analysis. A rutile TiO_2 (110) (1×1) single crystal (MaTecK) sample was prepared using successive cycles of argon ion sputtering and annealing in vacuum to 1000 K. Sample cleanliness and long-range order were checked using AES and LEED, respectively. Au was deposited onto an as-prepared TiO_2 (110) surface at room temperature. The deposition source consisted of a W filament wrapped around an Au rod, which was resistively heated to induce sublimation. The measured resistance of the doser remained constant through the experiment (0.882 Ω). While dosing, the applied filament current was kept constant and the same value was used for all doses (1.7 A). As both the applied current and the resistance of the doser were held constant, the rate of dosing is taken to be constant for all doses. The amount of Au deposited is expected to increase linearly with the time of exposure. Determining absolute Au coverage was not possible, therefore different Au doses are referred to in terms of their dosing time. The presence of Au on the TiO_2 substrate was confirmed by AES and HREELS. *Ex-Situ* STM micrographs were collected at room temperature using an Omicron VT-STM in constant current mode with an electrochemically etched W tip. Though exact nanoparticle coverage could not be determined, rough estimates of nanoparticle size and quantity were obtained using STM. HREELS measurements were collected in both specular (45°) and off-specular geometries. For off-specular measurements, the monochromator and analyser were set at 45° and 50° to the sample respectively (+5° off-specular). Off-specular measurements, as opposed to specular measurements, resulted in an increase in the intensity of vibrational modes relative to the elastic peak. An incident electron energy of 10 eV was used

for HREELS measurements. HREELS spectra were collected using a step size of 1 meV, a dwell time of 1 s and were produced as an average of 100 individual scans for each measurement. HREELS data were peak fitted using the Multi-peak fit 2.0 function of the Igor Pro software package. Fourier deconvolution of spectra was performed using a macro written for the Igor pro software package, adapted from Chang[32]. For a copy of the deconvolution macro used see appendix A4. For deconvoluted spectra the elastic peak was normalised to 1. Acetic acid (99.9%) and ethanol (99.8%) (all Sigma Aldrich) samples were used for organic dosing, contained within glass vials attached to the gas line of the chamber. Using a high precision leak valve the organics were introduced into the chamber as vapour. Prior to dosing, contaminants were removed from organic samples via multiple freeze-pump-thaw cycles. The purity of dosed gases was confirmed using an RGA mass spectrometer (VG Microtech). After organic vapour deposition, the background pressure of the chamber was allowed to recover before collecting HREELS measurements (approx. 30 minutes). UV irradiation was achieved by shining a 365 nm UV source (UVP Blak-Ray® Hg lamp) with a radiating power of 1.3 $mWcm^{-2}$ through a silica window (measured to adsorb 50% of UV light) directly facing the sample, yielding a total photon flux of 4.3×10^{16} cm^{-2} s^{-1}.

6.3 | Results and Discussion

6.3.1 | HREELS deconvolution and Data Treatment

To monitor the reactions of ethanol over clean and Au dosed TiO_2, HREELS was employed to measure the vibrational spectrum from a single crystal surface.

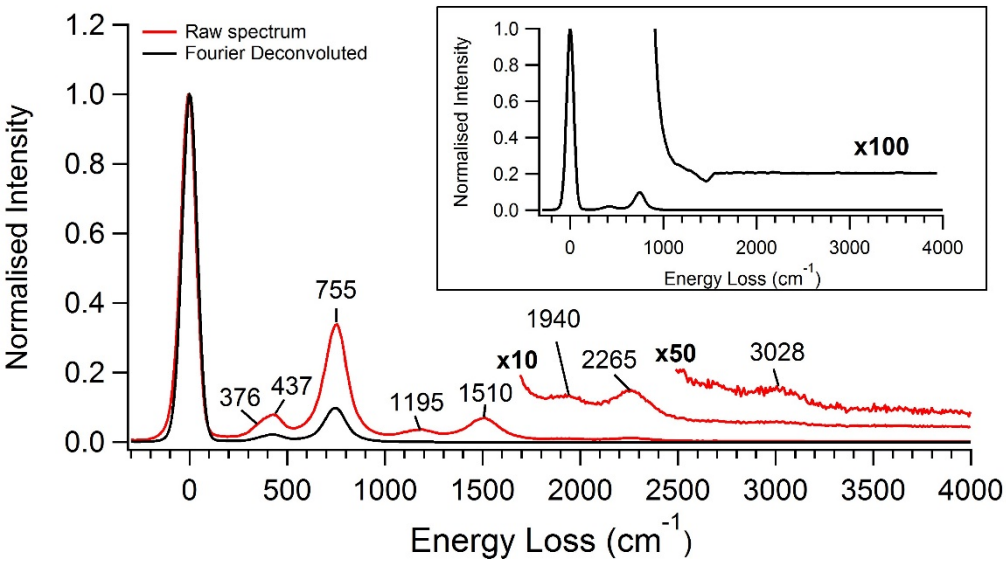

Fig. 6.1, raw (red curve) and Fourier deconvoluted (black curve) HREEL Spectra of the clean, as-prepared rutile TiO_2 (110) sample. Primary and multiple phonon loss peaks have been marked on the spectrum. The inset shows a magnified view of the deconvoluted spectrum. Both spectra were collected at 300 K in specular geometry (45°) with an incident electron energy of 10 eV. The measured FWHM of the elastic peak was 90 cm^{-1}.

The TiO_2 HREEL spectrum shows significant loss features at 376, 437, 755, 1195, 1510, 1940, 2265 and 3028 cm^{-1}. Such losses are well known in the HREELS literature and are characteristic of rutile TiO_2[23,33–36]. The losses at 376, 437, 755 cm^{-1} arise from the interaction of incident electrons with the optical surface phonons of TiO_2 (primary phonon losses). The remaining loss features, between 1200 and 3050 cm^{-1}, are assigned to multiple scattering events (multiple phonon losses), and appear at integer multiples of the primary phonon losses. The appearance of these features is consistent with previous HREELS studies of TiO_2 single crystals in the literature[32,37,38]. Typically, molecules have a vibrational

energy between 500 and 4000 cm^{-1}. Because phonon losses dominate this energy range in TiO_2 vibrational analysis using raw HREEL spectra is almost impossible. Fourier deconvolution is typically employed to remove the multiple phonon loss modes and uncover the vibrational spectrum[39]. A detailed description of the Fourier deconvolution process used in this work is given in chapter 2. Examples of the raw and Fourier deconvoluted HREEL spectra of clean TiO_2 are shown in Fig. 6.1. After deconvolution, the multiple phonon losses at 1195, 1510, 1940, 2265 and 3028 cm^{-1} were successfully removed, resulting in an almost completely featureless spectrum above 1000 cm^{-1}.

The inset of Fig. 6.1 shows a magnified view of the TiO_2 spectrum between 1000 and 4000 cm^{-1}. A negative intensity loss peak appears in the deconvoluted spectrum at 1450 cm^{-1}. Such a loss is not addressed in the literature concerning HREELS of TiO_2. There is no physical basis for a negative intensity peak in HREELS spectroscopy, and this feature is concluded to be an artefact generated by the Fourier deconvolution process. Similar work by Henderson *et al.* shows a positive artefact peak at 1515 cm^{-1} in their Fourier deconvoluted HREEL spectrum of TiO_2. They attribute this to a deviation from the perfect Poisson distribution of the multiple loss peaks, caused by measuring at an off-specular angle. This results in an underestimation of the multiple loss peak at 1510 cm^{-1}, thereby creating the artefact[33]. A similar explanation can be applied here, and the negative artefact at 1450 cm^{-1} is attributed to an overestimation of the multiple loss peak at 1510 cm^{-1} during Fourier deconvolution. HREELS data taken from clean rutile TiO_2 (110) by Wong *et al.* shows a similar negative peak at ~1450 cm^{-1}, though they do not address it in their work[22]. The negative feature is relatively broad and appears at an energy that overlaps a key portion of the vibrational spectrum for organic molecules. Removing this feature is essential to accurately describe the vibrational spectra of ethanol exposed TiO_2 as recorded by HREELS. Background subtraction is commonly employed in spectroscopy to remove signals that originate from the surrounding environment. Due to its nature, HREELS is measured under UHV conditions, and background subtraction is not commonly

employed as environmental contamination is minimal. This experiment seeks to explore the HREELS spectra of TiO_2 and Au/TiO_2 after ethanol adsorption, rather than study the samples prior to exposure. It is therefore reasonable to use measurements of clean and Au dosed TiO_2 samples as background spectra for the corresponding ethanol exposed samples. This has the desired effect of effectively removing the negative artefact at 1450 cm^{-1} without affecting the rest of the spectrum. A similar method of background subtraction was used by D'Amico *et al.* to study CO adsorption on ZnO with HREELS[40].

Fig.6.2 shows the deconvoluted spectra of TiO_2 and Au/TiO_2, taken before and after ethanol exposure (black and red curves), and of the exposed samples after background subtraction (blue curves). Pre-exposure spectra are relatively featureless apart from the negative feature at 1450 cm^{-1} that appears in both. After ethanol exposure, two distinct peaks at 2913, and 1568 cm^{-1} appear in the $EtOH/Au/TiO_2$ spectrum, with shoulders at 1378 and 1674 cm^{-1}. Following background subtraction, a new feature appears at 1478 cm^{-1}. Other features of the spectrum remain unchanged except the peak at 1674 cm^{-1}, which now appears as a shoulder at 1552 cm^{-1}. A similar effect is seen in the $EtOH/TiO_2$ spectrum where the shoulder at 1380 cm^{-1} is replaced by a peak at 1440 cm^{-1}. That only the negative loss feature is significantly affected by this process demonstrates the effectiveness of background subtraction for removing such a deconvolution artefact from HREEL spectra.

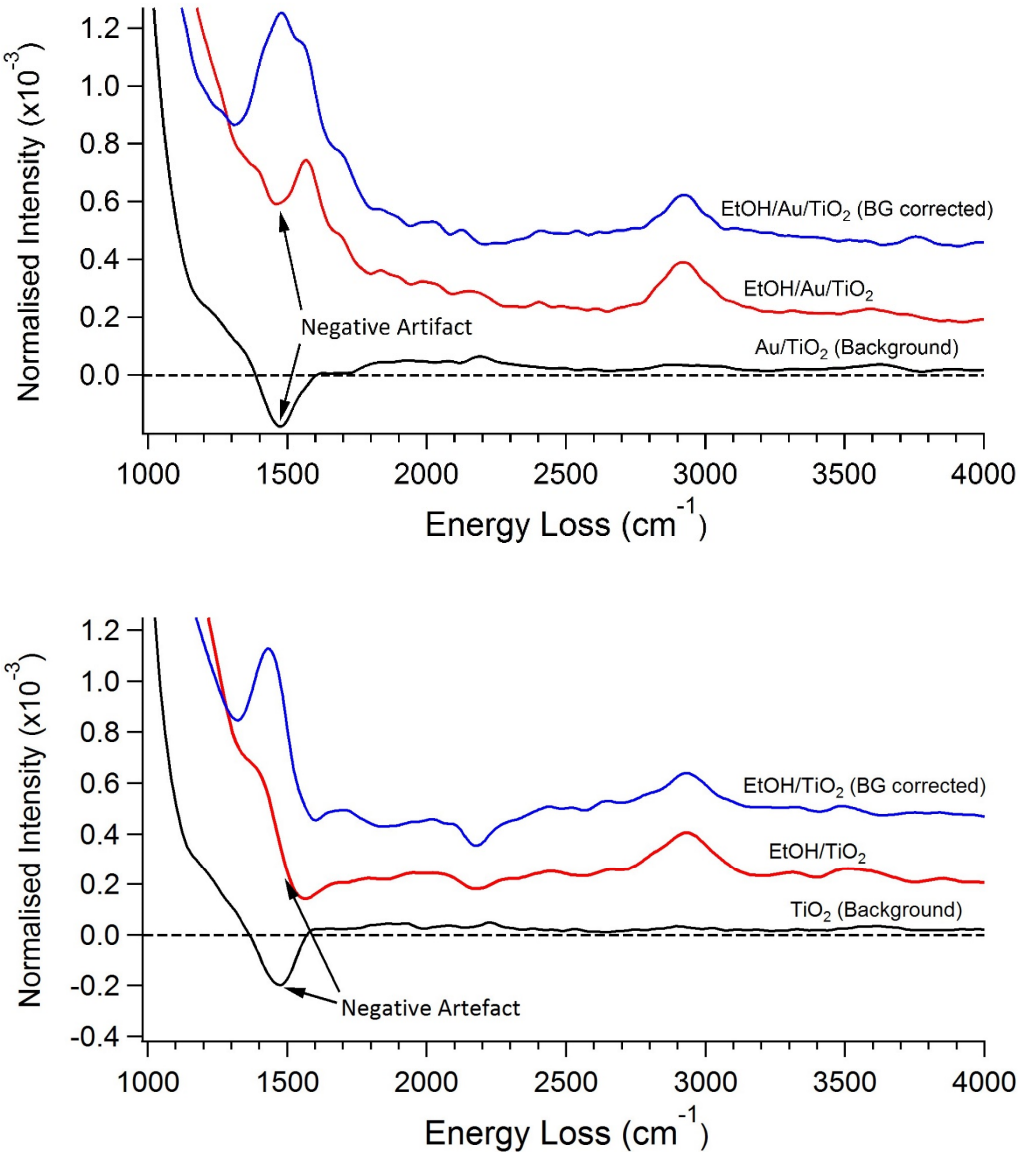

Fig.6.2, deconvoluted HREEL spectra of Au/TiO_2 (top) and TiO_2 (bottom) before and after exposure to 10 L of ethanol (black and red curves), and after background subtraction (blue curves). The pre-exposure spectra were used as a background measurements. For clarity, spectra, taken before and after background subtraction, have been offset vertically. All spectra were collected at 300 K, +5° from specular geometry with an incident electron energy of 10 eV. The measured FWHM of the elastic peak was 90 cm^{-1}.

6.3.2 | Clean Surface Characterisation

A clean, reduced rutile TiO_2 (110) single crystal was prepared by successive cycles of Ar ion bombardment and annealing to 1000 K. Fig.6.3 shows AES and LEED collected after sample preparation. The presented Auger spectrum is typical

of clean TiO_2, free from common contaminants (*e.g.* carbon)[41]. From LEED, a sharp 1×1 unit cell is seen indicating the sample has good long range surface order with no detectable 1×2 reconstruction.

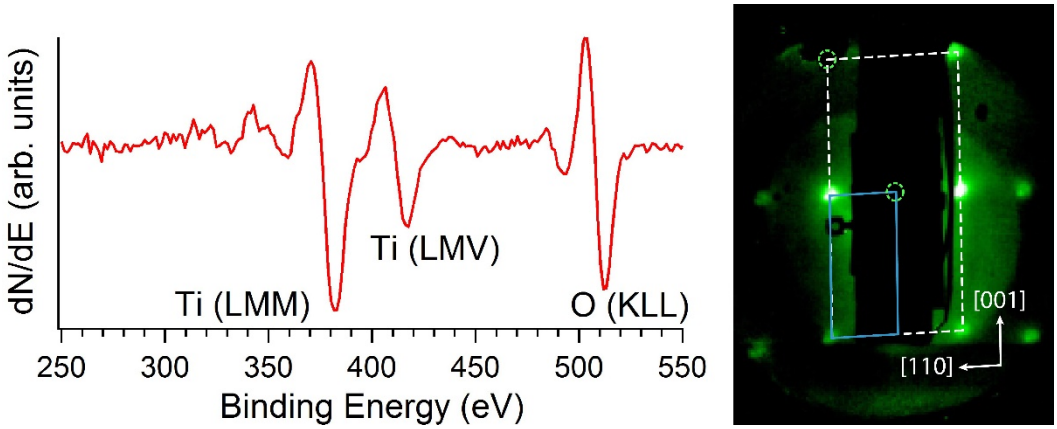

Fig.6.3, a) Auger spectrum taken from the clean rutile TiO_2 (110) surface after sample preparation. b) LEED pattern collected from the same sample. The rutile 1×1 unit cell (blue rectangle) demonstrates good surface order. Obscured spots are illustrated by green dashed circles. AES was measured with an incident beam energy of 1.4 kV and LEED at 80 eV.

6.3.3 | Au Dosing onto the Surface

Au was vapour deposited onto a clean rutile TiO_2 (110) surface, using the method described in section 6.2, for 30 seconds. After deposition, a new peak in the Auger spectrum appears at 69 eV, characteristic of the Au (NVV) Auger transition, confirming the presence of Au on the surface (Fig.6.4). A quantitative analysis of the Au coverage on the substrate is possible using a peak-to-peak analysis of the Au (NVV) and Ti (LMM) features in AES. However, it has been noted in the literature that this method of analysis can have up to a 50% margin of error and is particularly unreliable when measuring peaks below 200 eV[42,43]. Moreover, it is known that collecting spectra via a retarding field analyser (as is the case here) may further compound the error in quantitative AES analysis[44]. For these reasons, AES is presented here as a purely qualitative technique.

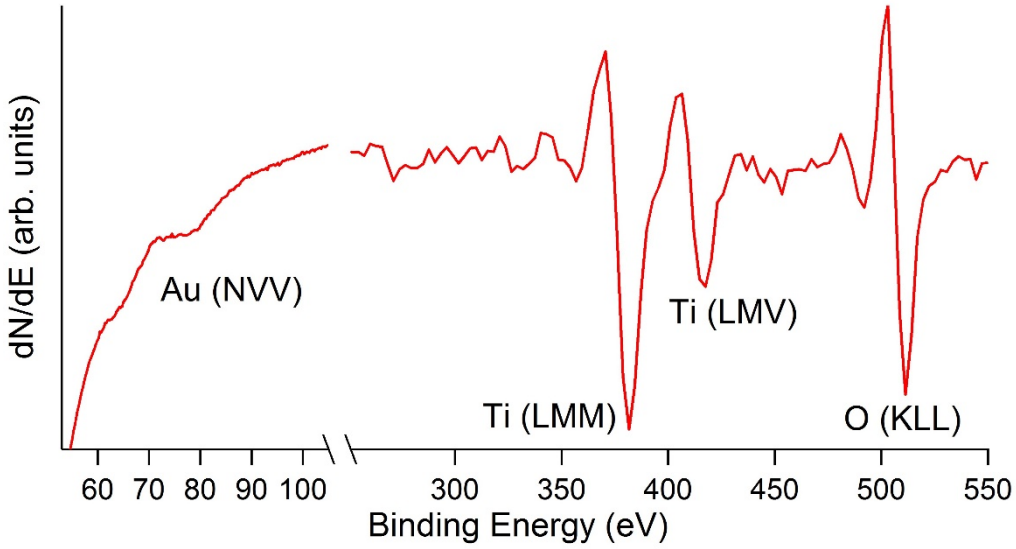

Fig.6.4, Auger spectrum of Au dosed TiO_2 surface. The area between 50 and 100 was collected in a separate scan to the rest of the spectrum. An incident beam energy of 1.4 kV was used for both measurements.

Fig.6.5 compares raw HREEL spectra of clean and Au dosed rutile TiO_2 (110). In the clean TiO_2 spectrum, a featureless depression is seen between 2 and 4 eV (16131-32262 cm^{-1}), see Fig.6.5 inset. After 30 seconds of Au deposition, a new loss appears within the depression at 2.6 eV (20970 cm^{-1}).

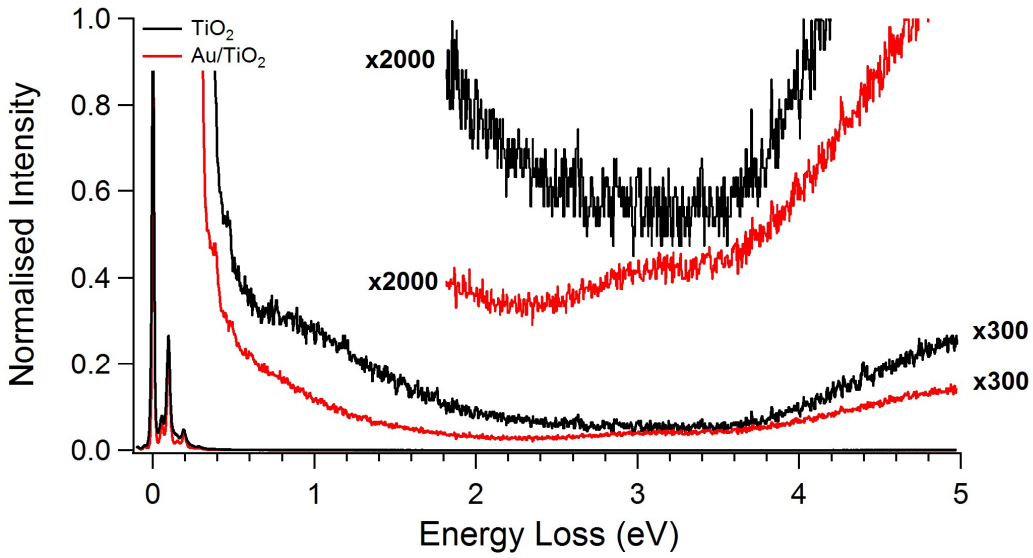

Fig.6.5, raw HREEL spectra of clean and Au dosed TiO_2. Magnified views of the 2-5 eV region are shown. Spectra were collected in specular geometry (45°) with an incident electron energy of 10 eV. The FWHM of the elastic peak was measured as 90 cm^{-1}.

Guo *et al.* have studied the development of a similar 2.6 eV loss feature as a function of Au coverage on TiO_2[45]. Their data shows that this feature appears when more than 0.2 MLE of Au is deposited onto the surface (where 1 MLE is defined as 1.387×10^{15} atoms cm^{-2}). In addition, as Au coverage increases to 0.6 MLE, the depression between 2 and 4 eV is no longer present in the spectrum. From these observations, it is inferred that the presence of a depression between 2 and 4 eV, and a loss feature at 2.6 eV, in the Au/TiO_2 spectrum shown in Fig.6.5 indicates an Au coverage between 0.2 and 0.6 MLE. Studies of the surface plasmon of bulk Au place it at a loss energy of 2.6 eV, corresponding well with the observed feature[46]. In view of this, Guo *et al.* attribute the appearance of the 2.6 eV loss to the transition from non-metallic to metallic as nanoparticle size increases.

After deposition, the Au/TiO_2 sample was transferred to an STM to further characterise particle size, coverage and morphology of the Au. Transferring between the STM and HREELS systems required the sample to be exposed to air for ~10 minutes. During this time, an unquantified amount of contaminants are expected to adsorb onto the sample surface. As STM images lack any form of chemical specificity, it is impossible to determine Au coverage when unknown surface adsorbates are present. Despite this, STM can still be used to determine particle size indirectly. STM measurements of Au/TiO_2, taken before and after exposing the sample to air, show that the nanoparticle morphology remains constant. Therefore, it is possible to obtain information regarding the maximum Au particle size using STM by measuring the largest particles present. Fig.6.6 (a) shows the TiO_2 surface after Au deposition for 30 seconds.

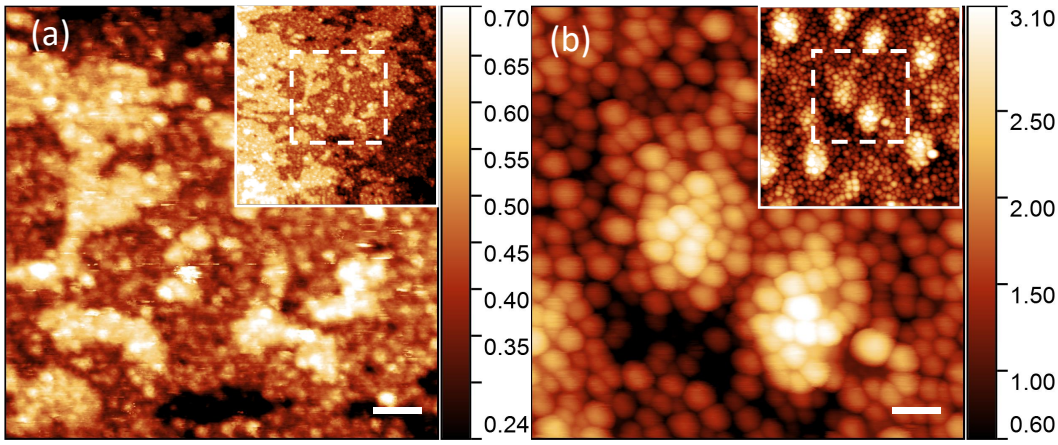

Fig.6.6, 50 nm^2 STM images of the Au/TiO_2 surface after (a) 30 seconds and (b) 5 minutes of Au vapour deposition. Insets show large scale images (250 nm^2) of the same areas shown in the main images. The z-scale of the colour maps used are given, in nm, on the right-hand side of each image. Scan parameters: V_S = +1.4 V, I_T = 100 pA. Scale bar: 5 nm. All images were recorded at 300 K.

At this coverage, terraces of the TiO_2 substrate can still be identified (Fig.6.6 (a) inset), and no individual features are seen with a diameter of 3 nm or greater. From this, the average Au nanoparticle diameter is concluded to be 3 nm or less. Comparing this with the data presented in Chapter 5 (showing the relation between nanoparticle diameter and Au coverage), the coverage of this sample can be revised to >0.2 and <0.5 MLE. This matches well with the coverage inferred by the appearance of an energy loss feature at 2.6 eV in HREELS (>0.2 MLE, <0.6 MLE). For comparison, Fig.6.6 (b) was taken from the same sample after Au deposition for 5 minutes, resulting in >1 MLE coverage. After 5 minutes of Au exposure, nanoparticles cover the whole surface with an average diameter of 3.0 ±0.6 nm, and no features of the TiO_2 substrate itself are visible.

6.3.4 | Ethanol Adsorption on TiO_2 and Au/TiO_2

After collecting suitable background measurements, each sample was exposed to 10 L of ethanol. Herein, ethanol exposed TiO_2 and Au/TiO_2 samples are referred to as $EtOH/TiO_2$ and $EtOH/Au/TiO_2$, respectively. During exposure, the ethanol purity was monitored via an RGA mass spectrometer. The background

pressure of the UHV chamber was allowed to recover to 5×10^{-10} mbar before collecting HREELS measurements. HREEL spectra were collected at a 5° off-specular angle to enhance the appearance of non-dipole modes, such as impact scattering modes, which typically have much weaker intensity than dipole modes. In brief, this works because dipole excitation modes have a high angular dependence, whereas non-dipole modes do not. By measuring at an off-specular angle the intensity of non-dipole modes appears enhanced relative to that of dipole modes, making them easier to identify in spectra. A more detailed explanation of the underlying principle of this phenomenon is given in Chapter 2. Though a larger off-specular angle would, in principle, enhance the appearance of non-dipole modes further, due to a sharp drop in the overall signal intensity it was not useful to collect spectra at angles greater than 5°.

EtOH/TiO_2

Fig.6.7 shows the HREEL spectrum collected from TiO_2 following exposure to 10 L of ethanol. After exposure, new loss features appear at 1130, 1440, 2820 and 2933 cm^{-1}. Using FTIR, Nadeem *et al.* have identified ethoxide as the main species present on powder anatase TiO_2 following ethanol exposure[27]. In their spectra, three features appear at 1378, 1442 and 1473 cm^{-1}, corresponding to the $\delta_s(CH_3)$, $\delta_{as}(CH_3)$, $\delta(CH_2)$ vibrational modes of ethoxide. Using this work as a guide, further analysis of the feature at 1440 cm^{-1} in Fig.6.7 was performed using the Igor Pro Multi-peak fit 2.0 program. Based on Nadeem *et al.*'s data, the Multi-peak fit 2.0 program was instructed to find the best fit of three Gaussian peaks within the broad feature at 1440 cm^{-1}. Fitting results indicate peaks at 1379, 1443 and 1483 cm^{-1} (Fig.6.7 inset). Following this, loss features at 1130, 1379, 1443, 1483, 2820 and 2933 cm^{-1} in the EtOH/TiO_2 spectrum can be assigned to ν(OC), $\delta_s(CH_3)$, $\delta_{as}(CH_3)$, $\delta(CH_2)$, $\nu_s(CH_3)$ and $\nu_{as}(CH_3/CH_2)$ vibrational modes respectively[22,23,33,47].

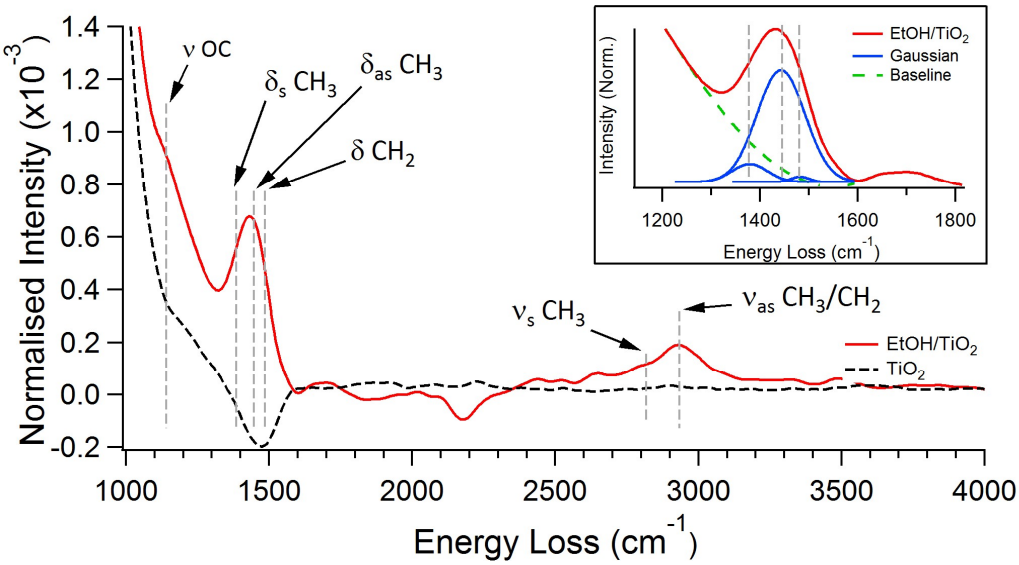

Fig.6.7, deconvoluted and background subtracted HREEL spectrum of TiO_2 after exposure to 10 L of ethanol (solid red line). The background measurement, taken from the sample before ethanol exposure, is shown for reference (dotted black line). Assigned vibrational modes are labelled on the spectrum. The inset shows an expanded view of the spectrum overlaid with Gaussian peak fit results. Spectra were collected at 300 K, +5° from the specular geometry with an incident electron energy of 10 eV. The measured FWHM of the elastic peak was 90 cm^{-1}.

There is some ambiguity in the assignment of features in this spectrum due to the poor resolution and signal-to-noise ratio. However, the similarity between the assignment of Nadeem *et al.*'s spectra and that of Fig.6.7 suggests that ethanol adsorption yields the same reaction products on both rutile and anatase TiO_2 (ethoxide)[27]. This is further supported by several TPD studies of ethanol exposed rutile TiO_2 single crystal that show thermal desorption of ethanol from the surface[48–53].

EtOH/Au/TiO$_2$

An Au/TiO_2 sample was prepared by vapour depositing Au for 30 s. From the characterisation measurements mentioned above, this is expected to produce an Au/TiO_2 sample with an Au coverage between 0.2 and 0.5 MLE and an average nanoparticle diameter of <3 nm. This sample was then dosed with 10 L of ethanol

in the same way as the bare TiO_2 sample. The deconvoluted, background subtracted HREEL spectrum of EtOH/Au/TiO_2 is shown in Fig.6.8.

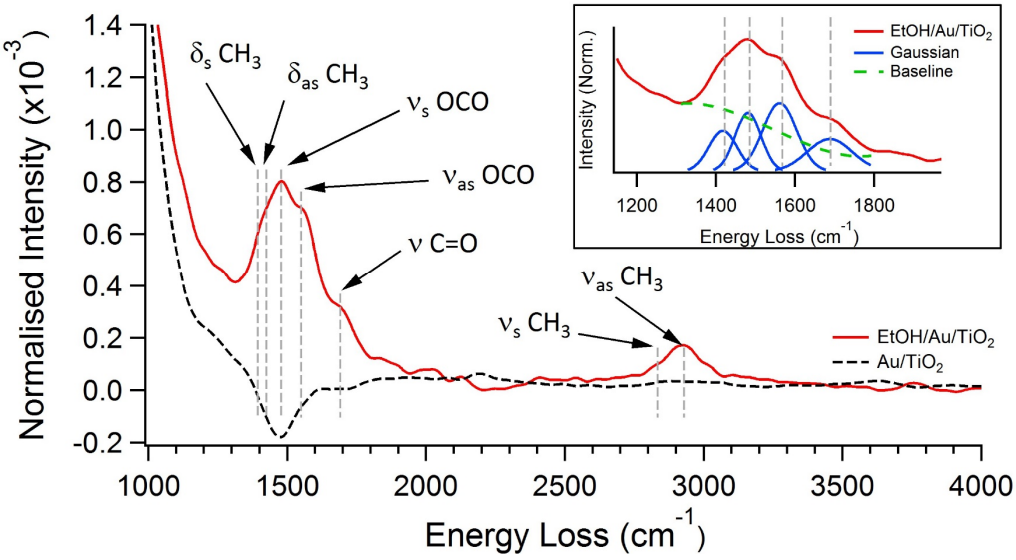

Fig.6.8, deconvoluted and background subtracted HREEL spectrum of Au/TiO_2 after exposure to 10 L of ethanol (solid red line). The background measurement, taken from the sample before exposure, is shown for reference (dotted black line). Assigned vibrational modes have been labelled on the spectrum. The inset shows an expanded view of the spectrum, overlaid with Gaussian peak fit results. Spectra were collected at 300 K, +5° from the specular geometry with an incident electron energy of 10 eV. The measured FWHM of the elastic peak was 90 cm^{-1}.

The same Gaussian peak-fitting program used to analyse EtOH/TiO_2 was employed to identify individual peaks within the broad feature between 1310 and 1800 cm^{-1}. Based on the appearance of a single peak and three shoulders, four Gaussian peaks were fit. From this, losses can be identified at 1418, 1481, 1561, 1688, 2835 and 2930 in the spectrum. The losses at 1688, 2835 and 2930 cm^{-1} can be assigned to ν(C=O), ν_s(CH_3) and ν_{as}(CH_3) vibrational modes, respectively[27]. The loss at 1561 cm^{-1} is unambiguous and can be assigned to the ν_{as}(OCO) mode of a carboxylate species. Assigning losses at 1418 and 1481 cm^{-1} is somewhat difficult as many vibrational modes overlap in this energy region. Fortunately, The position and inter-peak distances of the losses at 1418, 1481 and 1561 cm^{-1} matches well with the signature peaks of surface adsorbed acetate[54–56]. IR spectroscopy studies of acetate adsorbed on rutile TiO_2 powder identify signature peaks at 1400, 1454 and 1532 cm^{-1} [7]. With this in mind, the losses at 1481 and 1561 cm^{-1} are assigned

to ν_s(OCO), ν_{as}(OCO), respectively, and the loss at 1418 cm^{-1} is taken to be a convolution of $\delta_s(CH_3)$ and $\delta_{as}(CH_3)$ modes expected at ~1390 and 1430cm^{-1}. The separation of the ν_s(OCO) and ν_{as}(OCO) modes, $\Delta\nu_{as\text{-}s}$, in acetate vibrational spectra (and its derivatives) has been extensively studied by Deacon and Phillips[55]. Comparing $\Delta\nu_{as\text{-}s}$ of aqueous acetate, $\Delta\nu_{as\text{-}s\ (ionic)}$, with various metal complexes, they suggest three 'rules' for assigning the binding mode of acetate to a metal atom. $\Delta\nu_{as\text{-}s} > \Delta\nu_{as\text{-}s\ (ionic)}$ indicates monodentate coordination (η^1) to the surface, whereas $\Delta\nu_{as\text{-}s} < \Delta\nu_{as\text{-}s}$ (ionic) indicates a chelating (η^2) or bridging configuration (μ^2). In the latter case, if $\Delta\nu_{as\text{-}s}$ <105 cm^{-1} η^2 is the most likely geometry (except in the presence of short metal-metal bonds). Rotzinger *et al.* recorded $\Delta\nu_{as\text{-}s}$ values for acetate adsorbed on rutile and in aqueous solution to be 87 and 137 respectively[57]. The $\Delta\nu_{as\text{-}s}$ value of 79 cm^{-1}, measured from Fig.6.8, is consistent with Rotzinger *et al.*'s observations. Given the 'rules' laid out by Deacon and Phillips, the value of $\Delta\nu_{as\text{-}s}$ measured here infers that acetate adsorbs in either a η^2 or μ^2 configuration. Though this value is <105 cm^{-1}, due to the resolution of the recorded spectrum (90 cm^{-1}) a η^2 configuration cannot be conclusively assigned. Indeed, in the literature acetate is well known to bond to two adjacent Ti atoms (μ^2) on TiO_2 (110) following acetic acid exposure[58]. The lack of a ν(OC) mode at 1130 cm^{-1} on the Au dosed sample indicates the absence of ethoxide on the surface. The apparent lack of ethoxide on the surface suggests, its formation is unfavourable on Au/TiO_2, or subsequent reaction/decomposition occurs in the presence of Au nanoparticles. The appearance of acetate supports the suggestion that ethoxide undergoes further reactions on the Au/TiO_2 surface. From this observation, Au nanoparticles, supported by rutile TiO_2, appear to be an effective promotor of ethanol oxidation/acetate formation. In addition, the presence of the ν(C=O) vibrational mode at 1688 cm^{-1} suggests some amount of acetaldehyde may also be present on the surface.

EtOH/AuTiO$_2$ (Low Au coverage)

To investigate the effects of coverage on the catalytic properties of TiO_2 supported Au, a second sample was prepared with lower nanoparticle coverage. As before, Au was vapour deposited onto an as-prepared rutile TiO_2 (110) sample, but this time the duration of exposure was halved to 15 seconds. When maintaining constant dosing parameters, deposition time has a linear relationship with the resulting Au coverage. Therefore, halving the exposure time to 15 seconds should yield a total Au coverage of half the amount previously deposited, *i.e.* 0.1 – 0.25 MLE. The expected diameter of Au nanoparticles at this coverage is between 1.4 and 2.2 nm (see Chapter 5). The lower coverage Au/TiO_2 sample will be referred to herein as LC-Au/TiO_2. The HREEL spectrum of EtOH/LC-Au/TiO_2 is shown in Fig.6.9. After applying the same Gaussian peak fitting procedure used for the EtOH/TiO_2 spectrum, *i.e.* the best fit of three Gaussian peaks, losses were detected at 1395, 1430, 1478, 1645 and 2937 cm^{-1}. The losses at 1395, 1430, 1478, 1645 cm^{-1} and 2937 cm^{-1} can be assigned to $\delta_s(CH_3)$, $\delta_{as}(CH_3)$, $\delta(CH_2)$, $\nu(C=O)$ and $\nu_{as}(CH_3/CH_2)$ respectively[47,59]. As with Fig.6.7, the poor resolution and signal-to-noise ratio of the spectrum in Fig.6.9 makes assignment of these modes somewhat ambiguous. As such, any interpretation of this data cannot be considered as conclusive without further investigation. For example, the peak at 1645 cm^{-1} could be assigned to $\nu(C=C)$, suggesting the presence of an unsaturated hydrocarbon such as ethylene. This is also supported by the appearance of the $\delta(CH_2)$ and $\nu_{as}(CH_2)$ vibrational modes at 1478 cm^{-1} and 2937 cm^{-1}, respectively. However, $\nu(C=O)$ (*i.e.* acetaldehyde) could also be considered a likely assignment for the peak at 1645 cm^{-1} as ethylene is known to desorb from TiO_2 at <200 K, though this does not explain the presence of CH_2 on the surface[49].

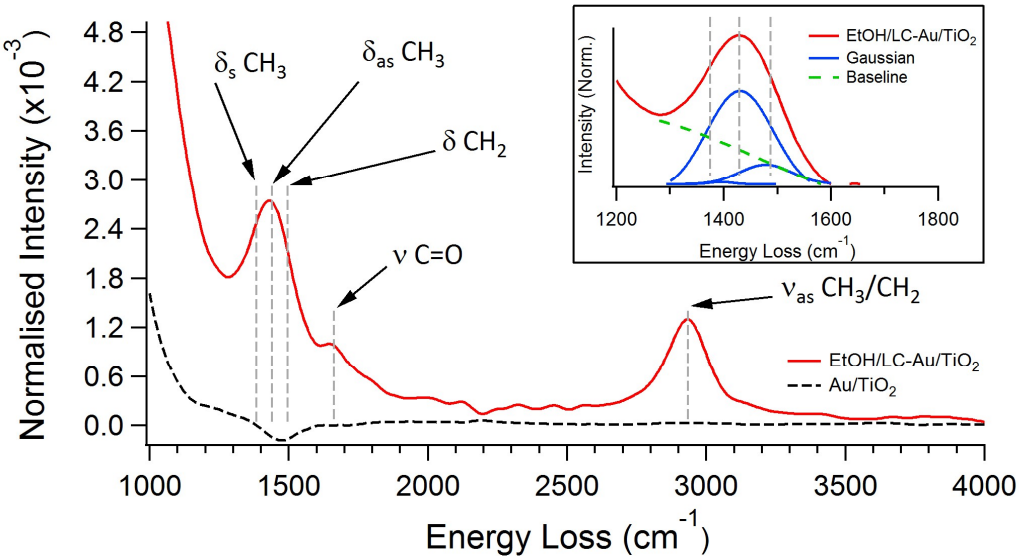

Fig.6.9, deconvoluted and background subtracted HREEL spectrum taken from Au/TiO_2 after exposure to 10 L of ethanol (solid red line). Prior to exposure, the sample was dosed with Au for 15 seconds (half the amount used previously). The background measurement, taken from the sample before ethanol exposure, is shown for reference (dotted black line). Assigned vibrational modes have been labelled on the spectrum. The inset shows an expanded view of the spectrum overlaid with Gaussian peak fit results. Spectra were collected at 300 K, +5° from the specular geometry with an incident electron energy of 10 eV. The measured FWHM of the elastic peak was 90 cm^{-1}.

Comparing the spectra of ethanol exposed Au/TiO_2 and LC-Au/TiO_2 highlights one key difference. No loss appears in the EtOH/LC-Au/TiO_2 spectrum at 1561 cm^{-1}, thereby ruling out the presence of acetate. This result suggests Au coverage has a dramatic effect on the catalytic activity of Au/TiO_2. Though assignments made from this data are complicated by the poor signal-to-noise ratio, acetaldehyde is proposed as a possible surface adsorbate. Acetaldehyde is a known intermediate in the oxidation of ethanol to acetate and has been observed previously from gas-phase oxidation experiments of ethanol over Au/TiO_2[60].

The data suggests that depositing 0.1-0.25 MLE Au over TiO_2 promotes either ethanol dehydrogenation or dehydration. However, for coverages above a critical value, Au_θ (between 0.2 and 0.5 MLE), ethanol oxidation occurs instead forming acetate. Such nanoparticle coverage/size (see Chapter 5) dependent behaviour is consistent with a study by Claus *et al.*, which shows preferential

hydrogenation of C=O to C=C over Au/ZrO_2 as nanoparticle size decreases below 2 nm[61].

6.3.5 | UV Irradiation of EtOH/TiO_2, Au/EtOH/TiO_2 and LC-Au/TiO_2

The effect of UV irradiation on ethanol exposed TiO_2, Au/TiO_2 and LC-Au/TiO_2 has also been investigated using HREELS. After collecting HREELS spectra from the ethanol dosed surfaces, each sample was exposed to UV light (365 nm) for 60 minutes. After UV irradiation, the HREEL specrum of each sample was measured a second time. Fig. 6.10 and Fig.6.11 show the lower (1000-2000 cm^{-1}) and higher (2500-3500 cm^{-1}) energy regions of the HREEL spectra collected from EtOH/TiO_2, EtOH/Au/TiO_2 and EtOH/LC-Au/TiO_2.

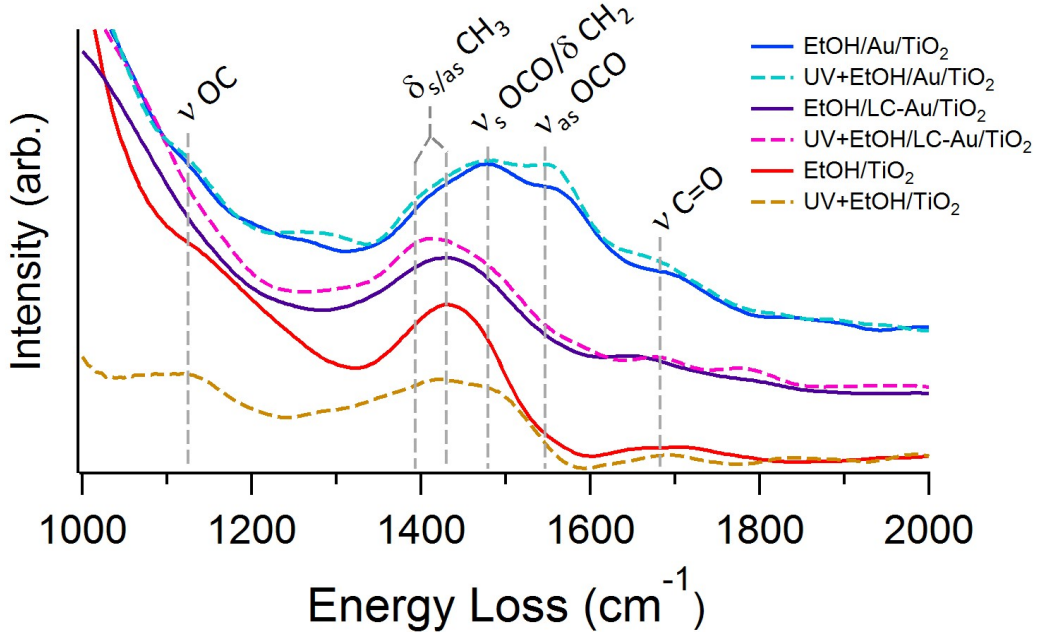

Fig. 6.10, deconvoluted and background subtracted HREEL spectra of EtOH/TiO_2, EtOH/Au/TiO_2 and EtOH/LC-Au/TiO_2 in the 1000-2000 cm^{-1} region. Dotted traces represent spectra taken from the respective samples after 60 minutes of UV exposure (365 nm). Assigned vibrational modes are labelled on the spectrum. For visual clarity, the spectra have been rescaled and vertically offset. All spectra were collected at 300 K, +5° from the specular geometry with an incident electron energy of 10 eV. The measured FWHM of the elastic peak was 90 cm^{-1}.

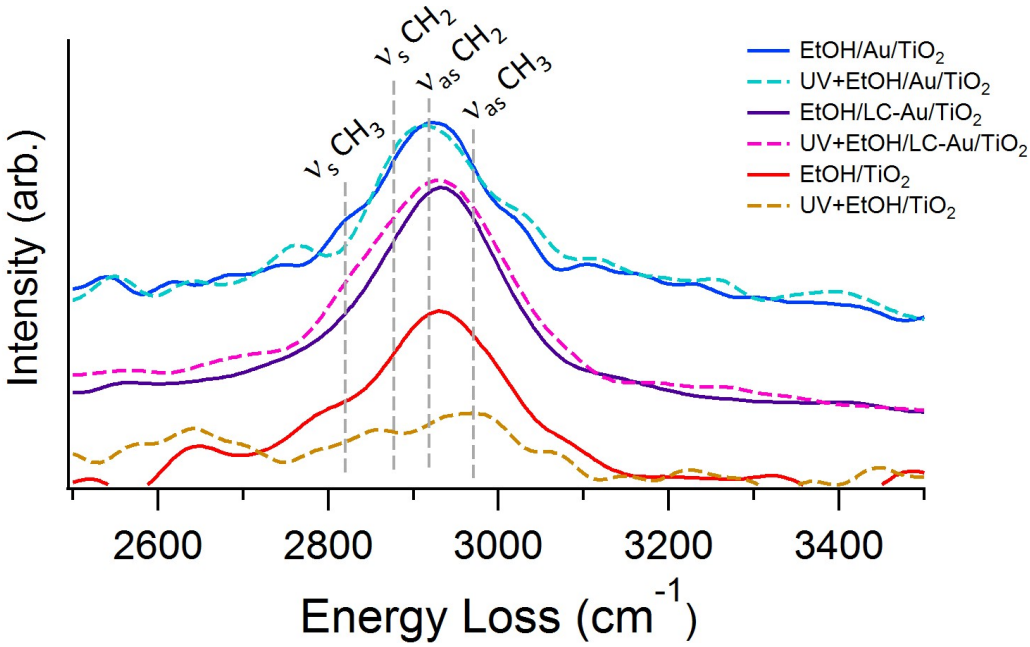

Fig.6.11, deconvoluted and background subtracted HREEL spectra of EtOH/TiO_2, EtOH/Au/TiO_2 and EtOH/LC-Au/TiO_2 in the 2500-3500 cm^{-1} region. Dotted traces represent spectra taken from the respective samples after 60 minutes of UV exposure (365 nm). Assigned vibrational modes are labelled on the spectrum. For visual clarity, the spectra have been rescaled and vertically offset. All spectra were collected at 300 K, +5° from the specular geometry with an incident electron energy of 10 eV. The measured FWHM of the elastic peak was 90 cm^{-1}.

Spectra collected prior to ethanol exposure (solid lines) are plotted together with those taken following 60 minutes of UV irradiation (dashed lines). Comparing the before and after spectra, a dramatic change is seen following UV irradiation of EtOH/TiO_2. The intensity of all detected loss peaks decreases significantly, and the higher enegy region becoms almost flat. This indicates that, surface species are being photo-desorbed from the TiO_2 surface, as is expected from the literature[62]. In contrast, the spectra taken from both Au covered samples does not replicate this behaviour. Work by Katsiev *et al*. has shown that the photo-oxidation cross section of acetate is ~100 times weaker than that of ethoxide[63]. Therefore, that very little change is seen in the post UV EtOH/Au/TiO_2 spectrum, compaired to that of EtOH/TiO_2, supports the assignment of acetate on the surface. Interestingly, acetaldehyde is expected to photodesorb from TiO_2 duing UV illumination, however, this is not seen in the post UV EtOH/LC-Au/TiO_2 spectrum[62]. In the EtOH/Au/TiO_2 and EtOH/LC-Au/TiO_2 spectra, some losses show

a slight increase in intensity after UV exposure. On LC-Au/TiO_2, the losses at 1395 cm^{-1}, 1430 cm^{-1} and 1478 cm^{-1} (assigned to $\delta_s(CH_3)$, $\delta_{as}(CH_3)$ and $\delta(CH_2)$ respectively) increase in intensity, and in the higher energy region the loss at 2820 cm^{-1} ($\nu_s(CH_3)$) also increases. The post UV spectrum of EtOH/Au/TiO_2 shows slightly increased intensity for the losses at 1560 and 1645 cm^{-1} (assigned to $\nu_{as}(OCO)$ and $\nu(C=O)$ respectively) in the lower energy region. In the higher energy region, the loss at 2820 cm^{-1} decreases in intensity ($\nu_s(CH_3)$). Increased intensity of $\nu_{as}(OCO)$ and $\nu(C=O)$ modes suggests a greater amount of acetate and acetaldehyde on the surface. The presence of $\nu_s(CH_2)$ and $\nu_{as}(CH_2)$ modes in the spectrum of EtOH/AuTiO_2 (both before and after UV exposure) can be explained by the presence of some amount of ethylene on the surface.

6.3.6 | Comparing Ethanol adsorption with Acetic Acid

In contrast to the data presented here using a rutile TiO_2 substrate, measurements taken from anatase Au/TiO_2 suggest ethoxide is the main adsorbate present after ethanol exposure[27]. To further support the assignment of acetate as the main species present on rutile Au/TiO_2 following ethanol exposure, the EtOH/Au/TiO_2 spectrum was compared with that of an acetic acid dosed TiO_2 (AcAc/TiO_2). An as-prepared rutile TiO_2 (110) sample was exposed to 10 L of acetic acid, and then HREEL spectrum was recorded, shown in Fig.6.12. The same peak fitting program was applied to the spectrum using the known vibrational features of surface adsorbed acetate as a guide. After exposure, losses appear in the spectrum at 1354, 1420, 1481, 1573, 1679, 2820 and 2939 cm^{-1}. These losses can be assigned to $\delta_s(CH_3)$, $\delta_{as}(CH_3)$, $\nu_s(OCO)$, $\nu_{as}(OCO)$, $\nu(C=O)$, $\nu_s(CH_3)$ and $\nu_{as}(CH_3)$ vibrational modes respectively and are consistent with surface adsorbed acetate (known to be present after exposing TiO_2 to acetic acid) with some amount of acetaldehyde[7,47,55–57,59]. The acetate/TiO_2 spectrum closely matches that of EtOH/Au/TiO_2 (Fig. 6.8), supporting the assignment of acetate/acetaldehyde on the Au/TiO_2 surface.

Following acetic acid exposure, the coverage of acetate on the rutile TiO_2 (110) surface is known to saturate at 0.5 MLE[64]. From this, one can roughly estimate the surface acetate coverage on ethanol exposed Au/TiO_2 using relative signal intensities. By measuring the peak height of the $\nu_{as}(OCO)$ mode in both the acetate/TiO_2 (assuming a 0.5 MLE coverage) and EtOH/Au/TiO_2 spectra, the surface coverage of acetate on Au/TiO_2, following 10 L ethanol exposure, is found to be 0.08 MLE. This suggests the rate of ethanol oxidation on Au/TiO_2 is very poor.

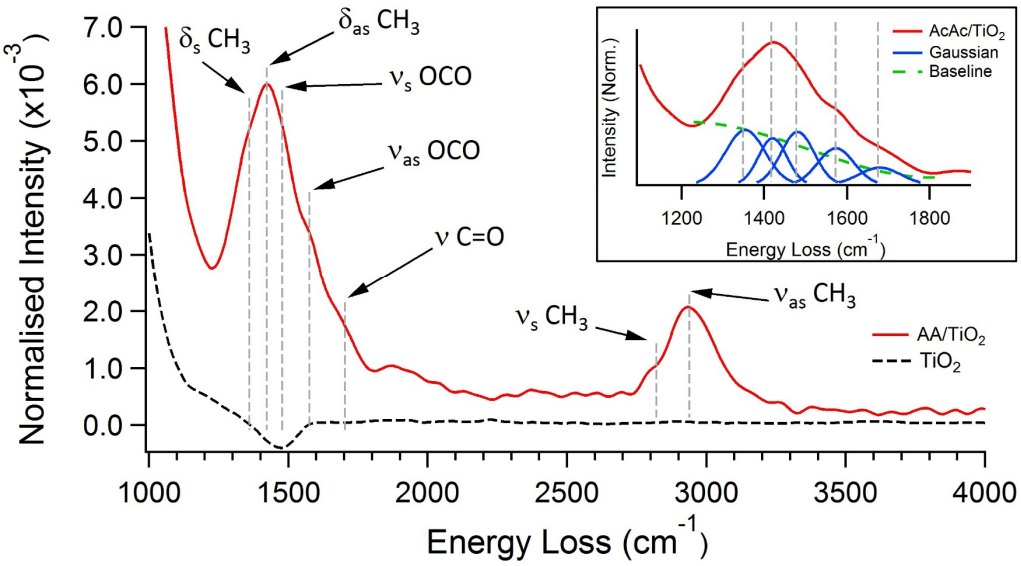

Fig.6.12, deconvoluted and background subtracted HREEL spectrum of TiO_2 after exposure to 10 L of acetic acid (solid red line). The background measurement, taken from the sample before exposure, is shown for reference (dotted black line). Assigned vibrational modes have been labelled on the spectrum. The inset shows an expanded view of the spectrum overlaid with Gaussian peak fit results. Spectra were collected at 300 K, +5° from the specular geometry with an incident electron energy of 10 eV. The measured FWHM of the elastic peak was 90 cm^{-1}.

As with the EtOH/Au/TiO_2 HREEL spectrum, the $\nu_{as}(OCO)$ to $\nu_s(OCO)$ peak separation was measured for the acetate/TiO_2 spectrum. The $\Delta\nu_{as\text{-}s}$ value measured from Fig.6.12 is 92 cm^{-1}. This closely agrees with the value measured for ethanol exposed Au/TiO_2 in this work (79 cm^{-1}) and Rotzinger *et al.*'s observations on rutile TiO_2 (110) adsorbed acetate (82 cm^{-1}).

It is important to consider the amount of data processing that has been applied to the data presented in this work and the impact this may have on the conclusions made herein. As mentioned above, each raw HREEL spectrum has been Fourier deconvoluted (during which a smoothing factor is applied) and then background subtracted, using a spectrum taken from the sample prior to organic deposition. Fig. 6.13 shows raw (solid lines) and Fourier deconvoluted (dashed) spectra taken from the Au/TiO_2 (black) $EtOH/AuTiO_2$ (red) samples. The inset of Fig. 6.13 shows a magnified view of each spectra together with the background subtracted $EtOH/TiO_2$ spectrum (blue line).

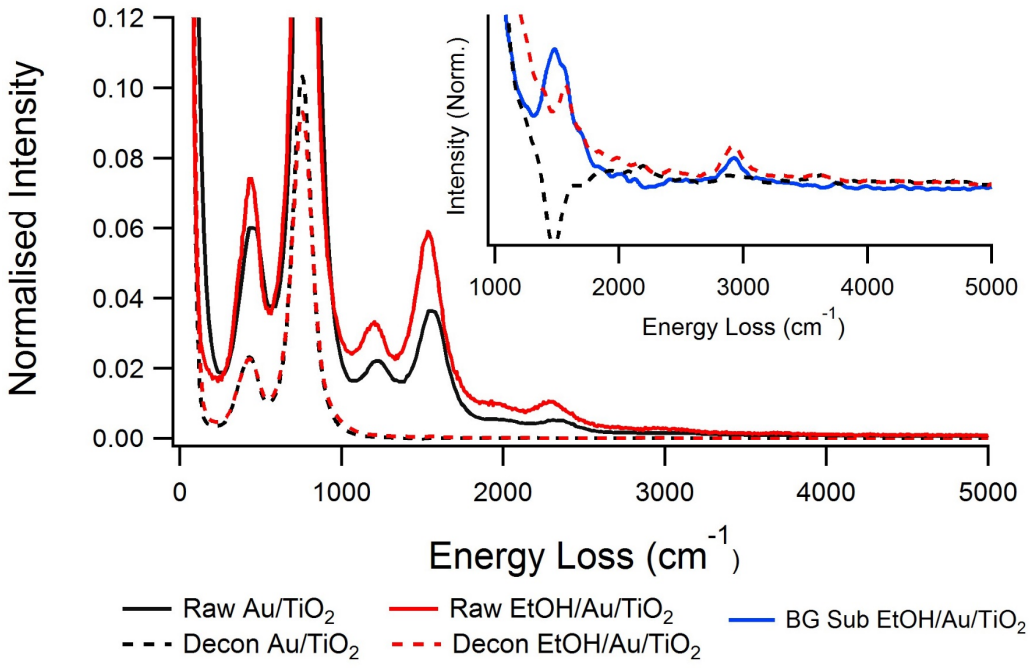

Fig. 6.13, raw (solid) and deconvoluted (dashed) HREEL spectra taken from an Au/TiO_2 sample before (black lines) and after (red lines) exposure to 10 L of EtOH. The inset shows an expanded view of the background subtracted $EtOH/Au/TiO_2$ spectrum (Au/TiO_2 was used as a background spectrum). The raw spectra have been omitted from the inset. Spectra were collected at 300 K, +5° from the specular geometry with an incident electron energy of 10 eV. The measured FWHM of the elastic peak was 90 cm^{-1}.

It is clear from the inset of Fig. 6.13 that, in this case, background subtraction has a significant effect on the $EtOH/Au/TiO_2$ spectrum, particularly between 1000 and 2400 cm^{-1}. Like Fig. 6.13, Fig. 6.14 shows all stages of data processing for the TiO_2 and $AcAc/TiO_2$ spectra. In contrast to $EtOH/Au/TiO_2$, the inset of Fig. 6.14 shows very little change in the $AcAc/TiO_2$ spectrum after

background subtraction. This observation is attributed to the much larger signal intensity of the acetate vibrational modes on the AcAc/TiO_2 sample compared to that of EtOH/Au/TiO_2.

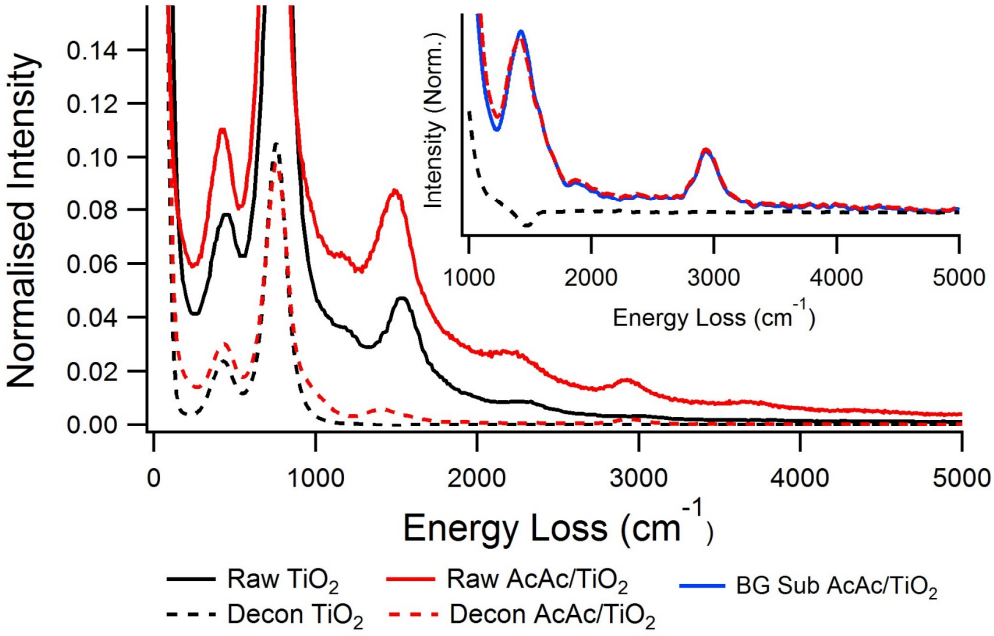

Fig. 6.14, raw (solid) and deconvoluted (dashed) HREEL spectra taken from a TiO_2 sample before (black lines) and after (red lines) exposure to 10 L of acetic acid. The inset shows an expanded view of the background subtracted AcAc/TiO_2 spectrum (TiO_2 was used as a background spectrum). The raw spectra have been omitted from the inset. Spectra were collected at 300 K, +5° from the specular geometry with an incident electron energy of 10 eV. The measured FWHM of the elastic peak was 90 cm^{-1}.

Although background subtraction is an effective tool for removing artefacts from HREEL spectra, this process also removes genuine signals originating from any adsorbates present on the sample prior to deposition. As such, any calculations of total adsorbate coverage, which are based on relative signal intensity, must have an associated error. The maximum error is therefore determined from the difference in intensity between spectra before and after background subtraction. The estimate for acetate coverage on the EtOH/Au/TiO_2 sample is thus revised to 0.08 (±0.03) MLE. The intensity of vibrational modes in raw spectra (*i.e.* before Fourier deconvolution) cannot be measured effectively, therefore, errors that arise during the deconvolution process cannot be accounted for in the above coverage estimate.

6.4 | Summary and Conclusions

Au nanoparticles have been deposited onto a reduced rutile TiO_2 (110) single crystal surface. Using HREELS and STM, an estimate of the nanoparticle coverage/size was determined. Three samples were prepared, clean TiO_2, Au/TiO_2 (0.2-0.5 MLE) and LC-Au/TiO_2 (0.1-0.25 MLE). HREELS spectroscopy reveals ethoxide as the main surface adsorbate present after exposing TiO_2 to ethanol. It is worth noting that the presence of OH on the surface cannot be ruled out as it is known to produce very weak losses, or not appear at all, in HREELS of TiO_2[22]. In previous photo-oxidation studies on single crystal rutile TiO_2 conversion of ethanol to acetaldehyde, and then to acetate is observed in the presence of UV radiation. Using mass spectrometry and XPS, Nadeem *et al.* observe acetaldehyde desorbing from an ethanol exposed rutile TiO_2 (110) surface during UV exposure. Subsequent XPS measurements indicate the presence of acetate on the surface after exposure to UV in the presence of O_2. In addition, they found the rate of acetaldehyde, and subsequently acetate, production increases as a function of O_2 partial pressure[50]. Ma *et al.* have suggested that the conversion of ethanol to acetaldehyde over TiO_2 likely occurs via the transfer of an α-H to an O_b site, forming an OH_b[62]. In the work presented here, depositing Au nanoparticles (0.2-0.5 MLE) onto rutile TiO_2 apparently modifies its surface chemistry, facilitating acetate formation without the need for UV illumination or O_2 exposure. It is worth noting however that this result may not be inconsistent with the results presented by Nadeem *et al.* as estimations of the total acetate coverage are very low (0.08 ±0.03 MLE). Methanol oxidation has been observed on CeO_2 and ZnO surfaces. In these processes, O is abstracted from the substrate to produce surface adsorbed formate[65,66]. From this, it is suggested here that ethanol oxidation over Au/TiO_2 is likely to occur via a similar process, abstracting lattice O from the TiO_2 surface to form acetate. Further to this, nanoparticle coverage was found to have a significant effect on the reaction behaviour of

Au/TiO_2. At lower Au coverage (0.1-0.25 MLE), rather than acetate, either acetaldehyde or ethylene is evidenced on the surface following ethanol exposure. It is therefore suggested that a critical Au coverage, Au_θ, exists between 0.25 and 0.5 MLE. Above Au_θ, ethanol oxidation occurs, producing acetate. Below Au_θ the oxidation reaction is either cut short at the dehydrogenation step (producing acetaldehyde) or, dehydration occurs instead (producing ethylene). The proposed reaction pathway for acetate formation (for Au coverage above Au_θ) is therefore:

$$CH_3CH_2OH \longrightarrow CH_3CHO \longrightarrow CH_3COO^- \qquad (6.4.1)$$

In chapter 5, the relationship between Au coverage and particle size was determined by measuring average Au diameter as a function of total coverage. The results here indicate small Au nanoparticles (1.4-2.2 nm diameter) are not active towards ethanol oxidation, highlighting the critical relationship between reactivity and nanoparticle size. These experiments show that, by controlling Au coverage, it is possible to tune the chemical properties of Au/TiO_2 to favour the formation of acetate over acetaldehyde/ethylene or *vice versa*. Au/TiO_2 has been demonstrated as an effective promoter for the conversion of ethanol to acetate. With further development, this process may prove to be a key component in the production of acetic acid from ethanol.

6.5 | References

1. Le Berre, C., Serp, P., Kalck, P., Torrence, G. P. & H. Cheung, R. S. Tanke, G. P. T. in *Ullmann's Encyclopedia of Industrial Chemistry* **8,** 255–271 (Wiley-VCH Verlag GmbH & Co. KGaA, 2000).

2. Malveda, M. P. & Funada, C. *'Acetic Acid', CEH Marketing Research Report*. (2010).

3. Haynes, A. in *Advances in Catalysis* (eds. Gates, B. C. & Knözinger, H.) **53,** 1–45 (Academic Press, 2010).

4. Seoane, J. L., Boutry, P. & Montarnal, R. Ethylene Oxidation to Acetic Acid with Pd-V , 05 Type Catalysts. **190,** 182–190 (1980).

5. Fierro-Gonzalez, J. C., Bhirud, V. a & Gates, B. C. A highly active catalyst for CO oxidation at 298 K: mononuclear AuIII complexes anchored to La_2O_3 nanoparticles. *Chem. Commun.* 5275–5277 (2005).

6. Liu, X. Y., Wang, A., Zhang, T. & Mou, C. Y. Catalysis by gold: New insights into the support effect. *Nano Today* **8,** 403–416 (2013).

7. Green, I. X., McEntee, M., Tang, W., Neurock, M. & Yates, J. T. Direct Formation of Acetate from the Partial Oxidation of Ethylene on a Au/TiO_2 Catalyst. *Top. Catal.* **56,** 1512–1524 (2013).

8. Connelly, K., Wahab, a. K. & Idriss, H. Photoreaction of Au/TiO_2 for hydrogen production from renewables: a review on the synergistic effect between anatase and rutile phases of TiO_2. *Mater. Renew. Sustain. Energy* **1,** 3 (2012).

9. Tritsaris, G. A., Vinichenko, D., Kolesov, G., Friend, C. M. & Kaxiras, E. Dynamics of the Photogenerated Hole at the Rutile TiO_2 (110)/Water Interface: A Nonadiabatic Simulation Study. *J. Phys. Chem. C* **118,** 27393–27401 (2014).

10. Park, J. B. *et al.* High catalytic activity of $Au/CeO_x/TiO_2(110)$ controlled by the nature of the mixed-metal oxide at the nanometer level. *Proc. Natl. Acad. Sci.* **106,** 4975–4980 (2009).

11. Dohnálek, Z., Lyubinetsky, I. & Rousseau, R. Thermally-driven processes on rutile $TiO_2(1\ 1\ 0)$-(1×1): A direct view at the atomic scale. *Prog. Surf. Sci.* **85,** 161–205 (2010).

12. Nadeem, M. A. *et al.* Photoreaction of ethanol on Au/TiO_2 anatase: Comparing the micro to nanoparticle size activities of the support for

hydrogen production. *J. Photochem. Photobiol. A Chem.* **216,** 250–255 (2010).

13. Fujishima, A., Zhang, X. & Tryk, D. A. TiO_2 photocatalysis and related surface phenomena. *Surf. Sci. Rep.* **63,** 515–582 (2008).

14. Kudo, A. & Miseki, Y. Heterogeneous photocatalyst materials for water splitting. *Chem. Soc. Rev.* **38,** 253–278 (2009).

15. Kim, T. S., Stiehl, J. D., Reeves, C. T., Meyer, R. J. & Mullins, C. B. Cryogenic CO oxidation on TiO_2-supported gold nanoclusters precovered with atomic oxygen. *J. Am. Chem. Soc.* **125,** 2018–2019 (2003).

16. Lai, X., Clair, T. P. S., Valden, M. & Goodman, D. W. Scanning tunneling microscopy studies of metal clusters supported on TiO_2 (110): Morphology and electronic structure. *Prog. Surf. Sci.* **59,** 25–52 (1998).

17. Lira, E. *et al.* Growth of Ag and Au Nanoparticles on Reduced and Oxidized Rutile TiO_2(110) Surfaces. *Top. Catal.* **56,** 1460–1476 (2013).

18. Al-Azri, Z. H. N. *et al.* The roles of metal co-catalysts and reaction media in photocatalytic hydrogen production: Performance evaluation of M/TiO_2photocatalysts (M = Pd, Pt, Au) in different alcohol-water mixtures. *J. Catal.* **329,** 355–367 (2015).

19. Khan, M. A., Sinatra, L., Oufi, M., Bakr, O. M. & Idriss, H. Evidence of Plasmonic Induced Photocatalytic Hydrogen Production on Pd/TiO_2 Upon Deposition on Thin Films of Gold. *Catal. Letters* **147,** 811-820 (2017).

20. Rodriguez, J. A. Gold-based catalysts for the water-gas shift reaction: Active sites and reaction mechanism. *Catal. Today* **160,** 3–10 (2011).

21. Connelly, K. A. & Idriss, H. The photoreaction of TiO_2 and Au/TiO_2 single crystal and powder surfaces with organic adsorbates. Emphasis on hydrogen production from renewables. *Green Chem.* **14,** 260–280 (2012).

22. Wong, G. S., Concepcion, M. R. & Vohs, J. M. Oxidation of methanol to formaldehyde on vanadia films supported on CeO_2(111). *J. Phys. Chem. B*

106, 6451–6455 (2002).

23. Henderson, M. A., Otero-Tapia, S. & Castro, M. E. The chemistry of methanol on the TiO_2(110) surface: the influence of vacancies and coadsorbed species. *Faraday Discuss.* **114,** 313–329 (1999).

24. Muggli, D. S., McCue, J. T. & Falconer, J. L. Mechanism of the Photocatalytic Oxidation of Ethanol on TiO_2. *J. Catal.* **173,** 470–483 (1998).

25. Hansen, J. O. *et al.* Unravelling Site-Specific Photo-Reactions of Ethanol on Rutile TiO_2(110). *Sci Rep* **6,** 21990 (2016).

26. Kelly, T. G., Stottlemyer, A. L., Yang, X. & Chen, J. G. Theoretical and Experimental Studies of Ethanol Decomposition and Electrooxidation over Pt-Modified Tungsten Carbide. *J. Electrochem. Soc.* **161,** E3165–E3170 (2014).

27. Nadeem, A. M., Waterhouse, G. I. N. & Idriss, H. The reactions of ethanol on TiO_2 and Au/TiO_2 anatase catalysts. *Catal. Today* **182,** 16–24 (2012).

28. Le Berre, C., Serp, P., Kalck, P. & Torrence, G. P. Ullmanns Encyclopedia of industrial chemistry: Acetic Acid*.* 1–29 (Wiley-VCH, Weinheim 2013).

29. Sano, K., Uchida, H. & Wakabayashi, S. A new process for acetic acid production by direct oxidation of ethylene. *Catal. Surv. from Asia* **3,** 55–60 (1999).

30. Gamble, L., Jung, L. S. & Campbell, C. T. Decomposition and protonation of surface ethoxys on TiO_2(110). **348,** 1–16 (1996).

31. Idriss, H. & Seebauer, E. G. Reactions of ethanol over metal oxides. *J. Mol. Catal. A Chem.* **152,** 201–212 (2000).

32. Chang, Z. Adsorbate studies at TiO_2 surfaces and metal TiO_2 interfaces using vibrational spectroscopies. *University of Manchester Thesis* (1999).

33. Henderson, M. A. An HREELS and TPD study of water on TiO_2(110): the extent of molecular versus dissociative adsorption. *Surf. Sci.* **355,** 151–166 (1996).

34. Thomas, F. S., Chen, N. S., Ford, L. P. & Masel, R. I. Vibrational/HREELS, UV/HREELS, and temperature-programmed desorption of benzene and hydrogen on (2 × 1)Pt(1 1 0). *Surf. Sci.* **486,** 1–8 (2001).

35. Qiu, H., Idriss, H., Wang, Y. & Wöll, C. Carbon−Carbon Bond Formation on Model Titanium Oxide Surfaces: Identification of Surface Reaction Intermediates by High-Resolution Electron Energy Loss Spectroscopy. *J. Phys. Chem. C* **112,** 9828–9834 (2008).

36. Gonzalez, R. J., Raman , Infrared , X-ray , and EELS Studies of Nanophase Titania. *Virginia Polytechnic Institute and State University Thesis* (1996).

37. Henrich, V. E. & Cox, P. A. in *The Surface Science of Metal Oxides* (Cambridge University Press, 2000).

38. Lazzari, R., Li, J. & Jupille, J. Spectral restoration in high resolution electron energy loss spectroscopy based on iterative semi-blind Lucy-Richardson algorithm applied to rutile surfaces. *Rev. Sci. Instrum.* **86,** (2015).

39. Cox, P. A., Flavell, W. R., Williams, A. A. & Egdell, R. G. Application of Fourier transform techniques to deconvolution of HREEL spectra. *Surf. Sci.* **152–153,** 784–790 (1985).

40. D'Amico, K. L., McFeely, F. R. & Solomon, E. I. High resolution electron energy loss vibrational studies of carbon monoxide coordination to the (10.hivin.10) surface of zinc oxide. *J. Am. Chem. Soc.* **105,** 6380–6383 (1983).

41. Sekine, T., Mogami, A., Kudoh, M. & Hirata, K. Peak energies and relative sensitivity factors in N(E) Auger spectra. *Vacuum* **34,** 631–636 (1984).

42. Mroczkowski, S. & Lichtman, D. Calculated auger sensitivity factors compared to experimental Handbook values. **131,** 159–166 (1983).

43. Zagorenko, A. I. & Zaporozchenko, V. I. Comparison of Accuracy of Various AES Methods for Quantitative Analysis of Refractory Metal Silicides. **17,** 237–244 (1991).

44. Seah, M. P. Quantitative Auger Electron Spectroscopy : Modulating the Spectrometer. *Surf. Int. Anal.* **1,** 91-95 (1979).

45. Guo, Q., Luo, L., Davis, K. A. & Goodman, D. W. Initial growth of Au on oxides. in *Surface and Interface Analysis* **32,** 161–165 (2001).

46. Nagahara, H., Ono, M. & Konishi, M. Plasmon resonance in sputtered gold films observed in scanning tunneling microscopy. *Appl. Surf. Sci.* **122,** 448–451 (1997).

47. Daly, L. H. & Wiberley, S. E. *Intorduction to Infrared and Raman Spectroscopy*. (Academic Press Inc, 1975).

48. Kong, D. *et al.* Growth, structure, and stability of Ag on CeO_2(111): Synchrotron radiation photoemission studies. *J. Phys. Chem. C* **115,** 6715–6725 (2011).

49. Chen, L., Smith, R. S., Kay, B. D. & Dohnalek, Z. Adsorption of small hydrocarbons on rutile TiO_2(110). **650,** 83–92 (2016).

50. Nadeem, A. M. *et al.* Ethanol photo-oxidation on a rutile TiO_2(110) single crystal surface. **13,** 7637–7643 (2011).

51. Jayaweera, P. M., Quah, E. L. & Idriss, H. Photoreaction of Ethanol on TiO_2(110) Single-Crystal Surface. *J. Phys. Chem. C* **111,** 1764–1769 (2007).

52. Walenta, C. A. *et al.* Ethanol photocatalysis on rutile TiO_2(110): the role of defects and water. *Phys. Chem. Chem. Phys.* **17,** 22809–22814 (2015).

53. Nadeem, M. A. Reactions of Ethanol on Bare and Noble Metal Modified TiO_2 Single Crystal and Powders. (The University of Auckland, 1994).

54. Lagutschenkov, A., Langer, J., Berden, G., Oomens, J. & Dopfer, O. Infrared spectra of metal acetates. *Phys. Chem. Chem. Phys.* **33,** 1961–1961 (2011).

55. Deacon, G. B. & Phillips, R. J. Relationships between the carbon-oxygen stretching frequencies of carboxylato complexes and the type of carboxylate coordination. *Chem. Rev.* **33,** 227–250 (1980).

56. Ito, K. & Bernstein, H. J. the Vibrational Spectra of the Formate, Acetate, and Oxalate Ions. *Can. J. Chem.* **34,** 170–178 (1956).

57. Rotzinger, F. P. *et al.* Structure and Vibrational Spectrum of Formate and Acetate Adsorbed from Aqueous Solution onto the TiO_2 Rutile (110) Surface. *J. Phys. Chem. B* **108,** 5004–5017 (2004).

58. Tao, J., Luttrell, T., Bylsma, J. & Batzill, M. Adsorption of acetic acid on rutile TiO_2(110) vs (011)-2×1 surfaces. *J. Phys. Chem. C* **115,** 3434–3442 (2011).

59. Edwards, H. G. M. & Lewis, I. R. Vibrational spectroscopic studies of iron(II) acetate. *J. Mol. Struct.* **296,** 15–20 (1993).

60. Sobolev, V. I., Yu, K., Simakova, O. A., Leino, A. & Yu, D. Applied Catalysis A : General Low temperature gas-phase oxidation of ethanol over Au/TiO_2. *Appl. Catal. A, Gen.* **433–434,** 88–95 (2012).

61. Claus, P., Bruckner, A., Mohr, C. & Hofmeister, H. Supported Gold Nanoparticles from Quantum Dot to Mesoscopic Size Scale: Effect of Electronic and Structural Properties on Catalytic Hydrogenation of Conjugated Functional Groups. *J. Am. Chem. Soc.* **122,** 11430 (2000).

62. Ma, J., *et al.* Photocatalytic Dissociation of Ethanol on TiO_2 (110) by Near-Band-Gap Excitation. *J. Phys. Chem. C* **117,** 10336-10344 (2013).

63. Katsiev, K. *et al.* Mechanism of Ethanol Photooxidation on Single-Crystal Anatase TiO_2(101). *J. Phys. Chem.* C **121,** 2940-2950 (2017).

64. Tao, J., Luttrell, T., Bylsma, J. & Batzill, M. Adsorption of Acetic Acid on Rutile TiO_2 (110) vs (011)-2×1 Surface. *J. Phys. Chem. C* **115,** 3434-3442 (2011).

65. Li, C., Domen, K., Maruya, K.-I.& Onishi, T. Spectroscopic Identification of Adsorbed Species Derived from Adsorption and Decomposition of Formic Acid, Methanol, and Formaldehyde on Cerium Oxide. *J. Catal.* **125,** 445-455 (1990).

66. Vohs, J. M. & Barteau, M. A. Conversion of Methanol, Formaldehyde and Formic Acid on the Polar Faces of Zinc Oxide. *Suf. Sci.* **176,** 91-114 (1986).

Chapter 7

Summary

7.1 | Summary

The investigations presented in this thesis have explored the nucleation, electron transfer and reaction behaviour of TiO_2 supported Au nanoparticles. In addition, the effect nanoparticle size has on these properties has been examined. To do this, several surface spectroscopy and microscopy techniques have been employed.

STM was used to examine the nucleation of Au nanoparticles over reduced rutile TiO_2 (110). Direct observations of the Au atom nucleation site on TiO_2 were achieved via two independent methods. Firstly, a TiO_2 surface was continuously imaged during in-situ deposition of Au. By comparing images of the same area before and after deposition, surface $O_{b\text{-}vacs}$ were identified as the favoured nucleation site of Au nanoparticles at room temperature. Secondly, precise atomic manipulation was achieved using voltage pulses from an STM tip while positioned over a single Au atom at low temperature. Using this method, Au atoms were controllably displaced from their nucleation sites revealing $O_{b\text{-}vacs}$ beneath. Statistical analysis of Au manipulation revealed displacement to be a two-electron process. This supports suggestions in the literature that Au forms covalent bonds with the Ti_{5c} atoms either side of an $O_{b\text{-}vac}$ on reduced TiO_2.

A combination of high resolution imaging and surface sensitive spectroscopy was used to probe the electronic character of Au nanoparticles on reduced rutile TiO_2 (110) as a function of particle size. Relative binding energy shifts of the Au 4f state were observed as the nanoparticle size was varied. Such binding energy shifts can be small and are affected by the reduction of the substrate. To remove any inconsistencies between different samples, a single Au/TiO_2 sample, with discrete regions of varying Au coverage, was created using an STM tip shadowed deposition. STM was then used to determine Au nanoparticle size for each region on the sample, and the position of each region was determined relative to the sample so they could be easily located for XPEEM

analysis. Core level spectroscopy of the sample revealed a two-stage shift in Au 4f binding energy as particle size increased. The observed binding energy shifts suggest that for small nanoparticles charge transfer occurs from $O_{b\text{-}vacs}$ to Au on the TiO_2 surface. It is proposed that at low coverages (<0.2 MLE) particle size effects dominate the electronic character of Au nanoparticles, whereas at higher Au coverages (>0.2, <0.4 MLE) charge transfer effects dominate. Such observations correlate well with published data on the size dependent catalytic activity of Au nanoparticles over TiO_2 substrates.

During spectroscopic measurements of Au/TiO_2, using synchrotron radiation, the observation of Ti^{3+} and Ti^{2+} species evidenced beam induced photo-reduction of the substrate. Despite this, no reduction was observed for Au after exposure to synchrotron radiation. Beam induced reduction of TiO_2 could be counteracted by the introduction of O_2 into the instrument during measurement.

Surface sensitive vibrational spectroscopy, HREELS, was used to follow the reaction of ethanol over TiO_2 and Au/TiO_2 surfaces. HREELS spectra suggest the ethoxide is the main species present on the TiO_2 surface following ethanol exposure. Depositing a low coverage of Au nanoparticles (0.1-0.25 MLE) prior to ethanol exposure results in either acetaldehyde or ethylene being formed on the TiO_2 (110) surface, rather than ethoxide. In contrast, after depositing 0.2-0.5 MLE Au, vibrational modes characteristic of acetate appear in the HREEL spectra. From this, it is suggested the presence of Au has a dramatic effect on the reactivity of TiO_2 towards organic species. In addition, the reactive properties of Au/TiO_2 can be tuned by controlling nanoparticle coverage/size. Deposition of Au below a critical coverage promotes ethoxide dehydrogenation(dehydration), forming acetaldehyde (ethylene), whereas deposition of Au above this coverage favours oxidation, forming acetate.

This work has addressed the thesis question posed in Chapter 1. Through these experiments, the Au/TiO_2 system has demonstrated potential for the

production of organic species (acetate/acetaldehyde) from renewable resources (ethanol).

7.2 | Future Work

To gain further insight into ethanol oxidation over Au/TiO_2, ambient pressure XPS (AP-XPS) could be used to determine more about the reaction mechanism. It would be interesting to monitor the electronic state of Au nanoparticles during ethanol exposure to determine the role they play in oxidation. In addition, XPS could provide further insight into the state of carbon species on the surface.

Au adsorption on TiO_2 is known to differ depending on the reduction state of the substrate. This causes variations in the nucleation properties and particle size distribution of Au nanoparticles at a given coverage. In addition, substrate reduction state may have a dramatic effect on the charge transfer characteristics of the system. It would be interesting to expand the investigations presented in Chapter 5 to include comparable measurements of the stoichiometric and oxidised rutile TiO_2 (110) surfaces.

Appendix

A 1 | $Au_{1\text{-}Ti}$ Site Determination

The adsorption site of Au_1 species on TiO_2, following tip displacement to Ti_{5c} rows, was determined by applying an overlay to STM images corresponding to the surface lattice parameters of TiO_2. To align the overlay with the crystal lattice, $O_{b\text{-}vacs}$ were used as a point of reference on the surface. Using this overlay, tip displaced $Au_{1\text{-}Ti}$ species were determined to adsorb atop Ti_{5c} sites on TiO_2 (110) (see A 1).

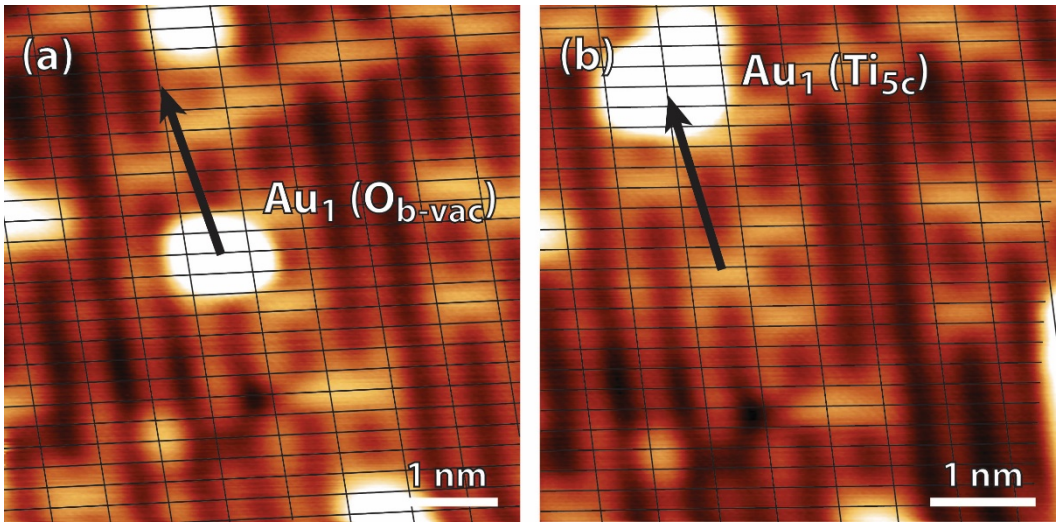

A 1, (a) STM image of an Au_1 species centred at an O_b row. (b), as (a) after STM tip induced displacement of Au_1 to a Ti_{5c} rows. A surface lattice overlay has been applied corresponding with the surface unit cell of TiO_2 (110). Points of intersection between horizontal and vertical lines indicate Ti_{5c} sites on the surface. A -2 V, 100 ms tip pulse was used to induce displacement. Arrows indicate the direction of Au_1 movement. Scan parameters: V_S = +1.2 V, I_T = 10 pA. All images were recorded at 78 K.

A 2.1 | Histogram Bin Width Determination

The bin width has a crucial effect on the distribution of data plotted in a histogram, which in turn affects the reliability of fitting a function to that data. A 2 shows three histograms plotted for the same data set (-1.8 V, 10 pA) with varying bin widths. If the selected bin width is too large (as in A *2* (a) then the precision of the data is reduced. If the bins are too small (as in A *2* (b) the signal to noise ratio of the data increases such that data cannot be fit in any meaningful way. To fit the data effectively, a compromise must be made concerning bin width to maximise both the signal to noise ratio and precision of the data (as in A *2* (c). In this work the bin widths of each histogram, plotted for the 16 unique pulsing parameter sets, were varied in order to obtain the optimum data distribution. For each histogram, a plot of $\ln(N_t)$ vs t was generated to help identify the most suitable data distribution.

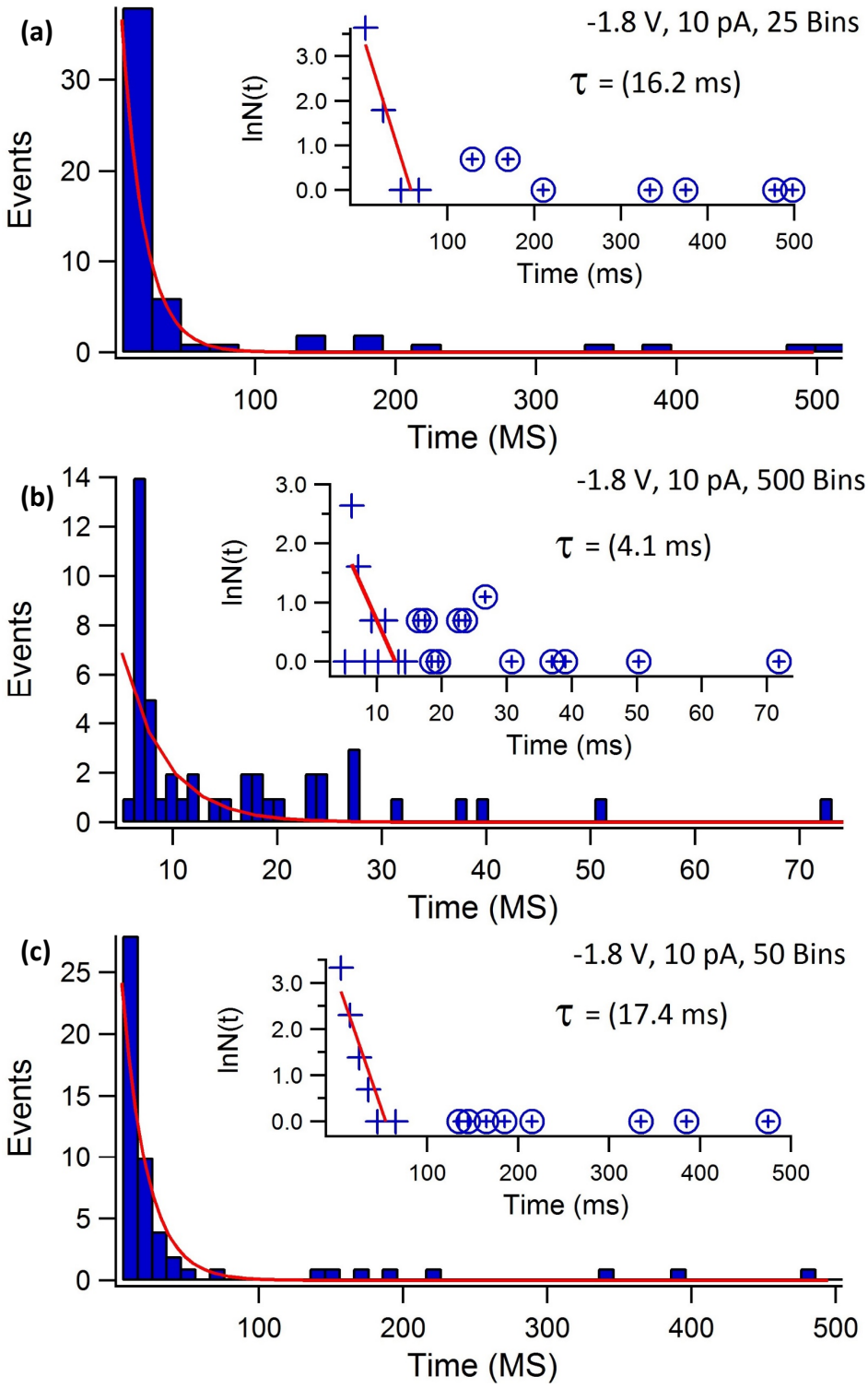

A 2, Histograms plotted for Au displacement times using -1.8 V, 10 pA pulses using (a) 25 bins, (b) 500 bins and (c) 50 bins, corresponding to bin widths of 20, 1 and 10 ms respectively. Red curves indicate the results of fitting an exponential function to each histogram. Values of τ determined from each histogram are also given. Insets show plots of $\ln(N_t)$ vs t for each histogram, together with a linear fit to the data (red line), used to highlight the suitability of the chosen bin width.

A 2.2 | Au_1 Pulse Induced Displacement Times

Tables 1-4 show the values of τ determined for each of the 16 unique pulsing parameter sets used in this work. Each value was determined from a histogram of pulsing events for each parameter set. The bin widths of each histogram plotted are given.

-1.9 V:

I_T	τ (ms)	Bin Width (ms)
1 pA	41	11.47
2 pA	28	6.8
5 pA	4	2.65
10 pA	1	0.37

-1.8 V:

I_T	τ (ms)	Bin Width (ms)
2 pA	167	42
5 pA	98	28.6
10 pA	17	10.27
20 pA	5	4.8

-1.7 V:

I_T	τ (ms)	Bin Width (ms)
5 pA	591	105.173
10 pA	140	67
20 pA	38	12.6
100 pA	1	0.224

-1.6 V:

I_T	τ (ms)	Bin Width (ms)
50 pA	126	76.56
100 pA	38	135.7
200 pA	4	1.05
300 pA	6	5.8

A3 | Au Height-to-Diameter Ratio at Very Low Coverage

From STM measurements, single Au atoms adsorbed at $O_{b\text{-}vac}$ sites on reduced rutile TiO_2 (110) had an average height and diameter of 183 ± 20 pm and 1.22 ± 0.07 nm, respectively. From this, an average nanoparticle height-to-diameter ratio of 0.15 was determined. Data was collected from a rutile TiO_2 (110) single crystal sample with a 0.08 MLE Au nanoparticle coverage. An example STM image of a single Au and accompanying line profile is shown in A 3.

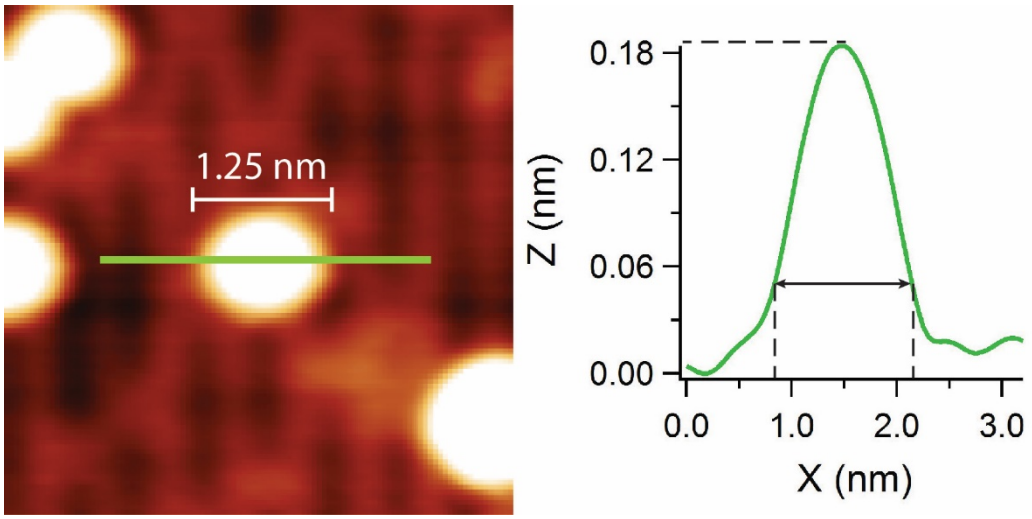

A 3, (left) 5 nm^2 STM image showing the surface of a TiO_2 (110) sample with a 0.08 MLE Au nanoparticle coverage. A single Au atom, adsorbed at an $O_{b\text{-}vac}$ site, can be seen in the centre of the image. (Right) A line profile taken from the central Au atom in the STM image, showing its measured height and diameter. The area of the line profile is indicated in the image together with the nanoparticle's measured diameter.

A4 | HREELS Fourier Deconvolution Macro

The Igor Pro procedure used in this work for HREELS deconvolution is detailed below.

The ‘menu’ macro sets-up the user interface required to execute the procedure in Igor Pro.

```
Menu "macros"

"Getwave.../1"
"-"
submenu "Deconvolution"
"Normalise.../2"
"Gaussian.../3"
"Fourier.../4"
end
"-"
"Results.../5"
"Rescale.../6"
Endmacro
```

The ‘Namewave’ macro prompts the user to assign a name to the raw HREEL spectrum to be loaded.

```
Macro namewave (w)
	string w
	prompt w, "Enter name of wave you wish to load: "
	string/g nwave
	nwave=w
Endmacro
```

The ‘Getwave’ macro loads the desired raw HREEL spectrum via a user specified file path. The X and Y components of the spectrum, initially stored as x1 and y1, are then renamed using the name assigned by the user during the ‘Wavename’ macro.,

```
Macro Getwave()
	namewave()
	LoadWave/G/A "General II: Users (General II): "Raw data storage file"" +nwave
	rename wave1, $("y"+nwave[0,10])
	duplicate wave0, wave2
	rename wave2, $("x"+nwave[0,10])
	duplicate/o $("x"+nwave[0,10]), x1
	duplicate/o $("y"+nwave[0,10]), y1
```

```
        display y1 vs x1
        showinfo
        Cursor/P A y1 0
Endmacro
```

The ‘Variables’ macro prompts the user to enter the resolution (FWHM of the elastic peak) and step size of the spectrum being processed and then stores this data in two variables.

```
Macro Variables(s,f)
        Variable s,f
        Prompt s, "Enter stepsize of data (meV): "
        Prompt f, "Enter FWHM of elastic peak (meV): "
        variable/g stepsize,FWHM
        stepsize=s
        FWHM=f
Endmacro
```

The ‘Rescale’ macro adjusts the x-axis of the spectrum so the centre of the elastic peak is at 0 energy loss and the scale is set to meV.

```
Macro Rescale()
        string name, namex
        variable maxy, maxx, miny
        variable/g xpos,zpos,minx,npoints
        name=csrwave(a)
        namex=csrxwave(a)
         iterate (numpnts($name)-xcsr(a))
                if ($name[i+xcsr(a)]>maxy)
                maxy=$name[i+xcsr(a)]
                maxx=$namex[i+xcsr(a)]
                xpos=i+xcsr(a)
                endif
         loop
         $namex-=maxx
         $namex=-1000*$namex
         $name/=maxy
         label left "Intensity (Normalised)"
         Label bottom "Electron Energy Loss (meV)"
Endmacro
```

The ‘Normalise’ macro normalises the spectrum so the top of the elastic peak is equal to 1 on the y-axis. The spectrum is then rotated in the x-axis splitting the elastic peak between the beginning and end of the spectrum. A linear background subtraction is performed by locating the lowest point of the spectrum

and a number of 0 values are added to the negative energy loss side of the elastic peak. This ensures that the total number of points plotted is equal to 2^n (4096 in this case), which is required to Fourier transform the spectrum.

```
Macro Normalise()
	variables()
	rescale()
	string name, namex
	variable wavearea,miny
	name=csrwave(a)
	namex=csrxwave(a)
	miny=1
	iterate (numpnts($name))
		if($name[i]<miny)
		miny=$name[i]
		minx=i
		endif
	loop

	$name-=miny
	zpos=(xpos+(4096-(numpnts($name))))
	npoints=(4096-(numpnts($name)))
	insertpoints 0, 4096-(numpnts($name)),$name, $namex
	if(xpos>minx)
		$namex=-stepsize*(p-zpos)
	else
		$namex=-stepsize*(p-xpos)
	endif
	wavearea=area ($name,0,4095)
	$name/=wavearea
	if (xpos>minx)
		rotate -zpos,$name
	else
		rotate -xpos,$name
	endif
Fourier()
Endmacro
```

The ‘Gaussian’ macro generates two Gaussian plots consisting of 4096 points (same as the spectrum) and an area of 1. The FWHM of one Gaussian is set to be equal to that of the loaded spectrum and another 2 meV wider. These two Gaussian plots represent the instrumental broadening and smoothing functions described in the Fourier deconvolution section of chapter 2. Finally, the macro rotates both Gaussians in the x-axis such that they are split between the beginning and end of each plot, thereby matching the rotated spectrum.

```
Macro Gaussian()
	variable sdsmooth,sdinst,cent,garea
	make /N=4096/o xginst,yginst,xgsmooth,ygsmooth
	xginst=p*stepsize
	xgsmooth=p*stepsize
	sdinst=FWHM/2.355
	sdsmooth=(fwhm+2)/2.355
	cent=(xginst[2047]+xginst[2048])/2
		yginst=(1/sdinst*(sqrt(2*pi)))*exp((-((xginst-cent)^2))/(2*sdinst^2))
		garea=area(yginst,0,4095)
		yginst/=garea
		rotate 2048,yginst

		ygsmooth=(1/sdsmooth*(sqrt(2*pi)))*exp((-((xgsmooth-
		cent)^2))/(2*sdsmooth^2))
		ygsmooth/=garea
		rotate 2048,ygsmooth
	display yginst vs xginst
	display ygsmooth vs xgsmooth
	TileWindows/O=1/C
Endmacro
```

The ‘Fourier’ macro performs the Fourier deconvolution of the spectrum being processed. First, the spectrum and both the instrumental broadening and the smoothing Gaussians are fast Fourier transformed (fft). The three functions are then manipulated as per the Fourier deconvolution formula (Chapter 2, eq. 2.2.20) to yield a Fourier transformed spectrum free from multiple phonon losses. The ’Complog’ macro allows the program to take logs of complex numbers. After manipulation, the resulting wave is inverse Fourier transformed (ifft) to produce a deconvoluted version of the original HREEL spectrum, on which the ‘Rescale’ macro is then run. This spectrum can now be used for vibrational analysis.

```
Macro Fourier()
Gaussian()
	string name, namex
	namex=csrxwave(a)
	name=csrwave(a)
	fft $name
	fft yginst
	fft ygsmooth
	$name*=(64*stepsize)
	make /n=2049/c/o ydivide
	ydivide=$name/yginst
	make /n=2049/o a,b
	a=real(ydivide);b=imag(ydivide)
```

```
		complog()
		yresult*=ygsmooth
		yresult[1024]=cmplx(0,0)
		yresult[2048]=cmplx(0,0)
		ifft yresult
		if(xpos>minx)
			rotate zpos,yresult
		else
			rotate xpos,yresult
		endif
		deletepoints minx, npoints, yresult
		make /n=(4096-npoints)/o xresult
		xresult=p*stepsize*0.001
		rename yresult, $("y"+nwave[0,10]+"dec")
		rename xresult, $("x"+nwave[0,10]+"dec")
		display $("y"+nwave[0,10]) vs $("x"+nwave[0,10])
		showinfo
		display $("y"+nwave[0,10]+"dec") vs $("x"+nwave[0,10]+"dec")
		showinfo
		Cursor/P A $("y"+nwave[0,10]+"dec") 0
Rescale()
		TileWindows/O=1/C
Endmacro

Macro Complog()
		make /N=2049/o/c yresult
		make /N=2049/o re,im
		re=ln(sqrt((a)^2+(b)^2))
		im=(atan(b/a))
		yresult=cmplx(re,im)
Endmacro
```

The ‘Results’ macro is used to display the raw and deconvoluted spectra of the last data set processed.

```
Macro results()
		make /n=(4096-npoints)/o xresult
		xresult=p*stepsize*0.001
		rename yresult, $("y"+nwave[0,10]+"dec")
		rename xresult, $("x"nwave[0,10]+"dec")
		display $("y"+nwave[0,10]+"dec") vs $("x"+nwave[0,10]+"dec")
		showinfo
		display $("y" +nwave[0,10]) vs $("x"+nwave[0,10])
		showinfo
		TileWindows/O=1/C
Endmacro
```